Magnetized, Laser-Driven, Plasma Experiments at Astrophysically Relevant Conditions, and Proton Imaging of Magnetic Fields

by

Joseph Maurice Levesque

A dissertation submitted in partial fulfillment
of the requirements for the degree of
Doctor of Philosophy
(Applied Physics)
in The University of Michigan
2020

Doctoral Committee:

Associate Professor Carolyn Kuranz, Chair
Professor R Paul Drake
Research Scientist Gennady Fiksel
Associate Professor Ryan McBride
Assistant Professor Louise Willingale

Joseph Maurice Levesque

jmlevesq@umich.edu

ORCID iD: 0000-0003-0952-9974

ACKNOWLEDGEMENTS

With the exception of what went on inside the OMEGA target chamber, this work was not accomplished in a vacuum, there are many people that have contributed to my success during my time in Michigan. Foremost of those I wish to thank is my advisor, Carolyn Kuranz, who defined much of my research trajectory in magnetized HEDP and managed to keep me on track over the years, and who provided valuable professional insight and opportunities throughout. I want to thank Paul Drake for introducing me to the field of High-energy-density physics and for offering me the opportunity to come to Michigan through the Applied Physics program. I also want to thank Frederico Fiuza, who, since my time at SLAC onward, provided me with and advised me on the very interesting problem of proton imaging of filamentary fields, which required a lot of creative thinking over many years, and which came to a satisfying conclusion. Additionally, I greatly appreciate the insightful critiques of this thesis from my committee: Carolyn Kuranz, Paul Drake, Ryan McBride, Louise Willingale, and Gennady Fiksel.

This work would not have been possible without the target fabrication expertise of Sallee Klein, proton imaging insight from Mario Manuel, the astrophysical and MHD expertise of Pat Hartigan, and the computational and mathematical advice from Tim Handy and William Gray. Finally, I am especially grateful to Woody VanDervort, Heath LeFevre, Mac Cathles, Matt Trantham, and Rachel Young, for humoring me and some of my crazy ideas.

In addition, there are many sources of funding which contributed to my work that should be noted: This work was supported by the U.S. Department of Energy, through the NNSA Center of Excellence under grant number DE-NA0003869, the NNSA-DP and SC-OFES Joint Program in HEDLP, grant number DE-NA0002956, the NLUF Program and Rice University, grant number DE-NA0002722, NLUF Program, grant number DE-NA0002719, through SLAC Contract No. DE-AC02-76SF00515, through the U.S. DOE Office of Science, Fusion Energy Sciences under FWP 100182 and FWP 100237, and through the LLE, University of Rochester by the NNSA/OICF under Cooperative Agreement numbers DE-NA0001944 and DE-NA0003856.

TABLE OF CONTENTS

LIST OF FIGURES

LIST OF TABLES

LIST OF ABBREVIATIONS

1D One-dimensional

2D Two-dimensional

3D Three-dimensional

AU Astronomical Unit

CME Coronal mass ejection

EOS Equation of state

EM Electromagnetic

EPW Electron plasma wave

HED High energy density

HEDP High energy density physics

IAW Ion-acoustic wave

ICF Inertial confinement fusion

ITS Imaging Thomson scattering (system)

MHD Magnetohydrodynamic

MIFEDS Magneto-Inertial Fusion Electrical Discharge System

NIF National Ignition Facility

PIC Particle-in-cell

TNSA Target-normal sheath acceleration

TS Thomson scattering

ABSTRACT

This thesis presents analysis relevant to two magnetized, astrophysically relevant experimental campaigns that were performed at the OMEGA laser facility. The magnetic fields of these systems were measured using proton imaging, in which high-energy protons interact with and are deflected by the electromagnetic fields, forming spatial variations in the proton fluence on the image plane. Proton images are determined by both the amplitude of the field and the orientation of the field relative to a proton's trajectory, which makes it difficult to generalize between different systems, although certain geometrical effects should always be considered.

The collisionless interaction of two counter-propagating, laser-irradiated plasmas results in the formation of small-scale magnetic filaments via the Weibel instability, a process which may explain the presence of magnetic fields throughout the intergalactic medium. Proton images of experiments studying this phenomenon display repeatable features corresponding to the filaments. Through analytical approximations and statistical analysis of synthetic proton images we determined that the observed images features fundamentally correspond to the transverse extent of the constituent filaments. How the image features related to the underlying field had not previously been understood.

The magnetic field produced by planets with active dynamos, like the Earth, can exert sufficient pressure to oppose inflowing, supersonic stellar wind plasmas. The effective obstacle to the flow in these systems is the pressure-balance surface between the stellar wind and the magnetic field, known as the magnetopause, and a standing bow shock forms at a standoff distance upstream from the magnetopause to redirect the flow. We performed scaled experiments to explore magnetized bow shocks, which consisted of a slow, low-density

plasma flow impinging on the external azimuthal magnetic field around a current-carrying wire. We infer the presence of a shock at a significant standoff distance from the wire from the spatially resolved, optical, Thomson scattered spectra, and the inferred density jump suggests significant magnetization. We also observe the formation of a bow shock around the magnetized wire in proton images of the magnetic fields at 60, 70, and 80 ns after the initial laser drive for two different field amplitudes. Simulations of the experiment performed using the FLASH code supplement the data.

CHAPTER 1

Introduction

This thesis has two primary components: the analysis of proton images of randomized systems of filamentary magnetic fields, and experiments to generate bow shocks in the interaction of a flowing plasma and a strong magnetic pressure external to the plasma. These components are both concerned with magnetic fields and interactions that can be related to astrophysical phenomena, forming the overarching theme of studying magnetic fields in laboratory astrophysics experiments. In this chapter I lay the foundation for the experiments and analysis presented in Chapters 3, 4, and 5. The experiments covered in this thesis are all in the High-energy-density regime of physics, or at least performed in facilities which achieve these conditions, so a brief overview is provided in Section 1.1, followed by an introduction of the experimental facility in Section 1.2. Section 1.3 introduces the concept of laboratory astrophysics, wherein astrophysical phenomena can be explored in experiment through the use of magnetohydrodynamic scaling parameters. Section 1.4 provides a brief overview of magnetohydrodynamic shocks. Section 1.5 then introduces the concept of collisionless plasmas and how the Weibel instability can produce filamentary magnetic fields when two such plasmas interact. Section 1.6 describes the interaction of the solar wind with the Earth's magnetic field, the terrestrial bow shock, and why experiments may be a good way of studying this interaction. Section 1.7 provides a brief overview of the proton imaging diagnostic, which is further developed in Chapter 2. Section 1.8 describes the basics of Thomson scat-

tering of laser light for measuring plasma parameters, used further in Chapter 4. Section 1.9 provides a brief summary of the following chapters, and section 1.10 accounts for the specific contributions I have made in each.

1.1 High-Energy-Density Physics

The Manhattan project and the development of nuclear weapons introduced a new regime of physics for terrestrial exploration — high-energy-density (HED) physics — which describes systems at energy densities (or pressures) exceeding 1 MBar.[1] At HED conditions, materials at or even exceeding solid densities often behave hydrodynamically, and are typically highly ionized. Systems exhibiting high energy densities are not unusual in nature, for example, such conditions are present in stars and the interiors of massive planets.

Following the advent of lasers came the recognition that sufficiently high-intensity, pulse-shaped lasers could feasibly be used to implode capsules of nuclear fuel to initiate controlled thermonuclear burn on laboratory scales.[2] Now, controlled HED conditions are routinely achieved in specialized, pulsed-power, laboratory settings, which utilize either high-intensity lasers or the direct application of electric current in a z-pinch configuration. Today, the United States' inertial confinement fusion (ICF) program studies nuclear fusion in controlled, laboratory experiments, with the goal of achieving sustained nuclear burn.[3,4] The efforts in ICF, though they apply in part to potential commercial fusion energy production, are driven primarily because of their relevance to maintaining the nuclear stockpile. As a result of the end of the Cold War, the United States moratorium on testing in 1992, and the Comprehensive Test Ban Treaty in 1996, determining the longevity of the weapons stockpile has shifted to computational modeling, informed by HED and ICF experiments, rather than testing by detonation. There is a clear connection between HED physics and nuclear weapons — the implosion of solid fissile material by detonation of high-explosives occurs at HED conditions, which allows the initially solid fuel to compress hydrodynamically, at least until it reaches a critical mass for fission and destroys itself. Although laboratory-controlled

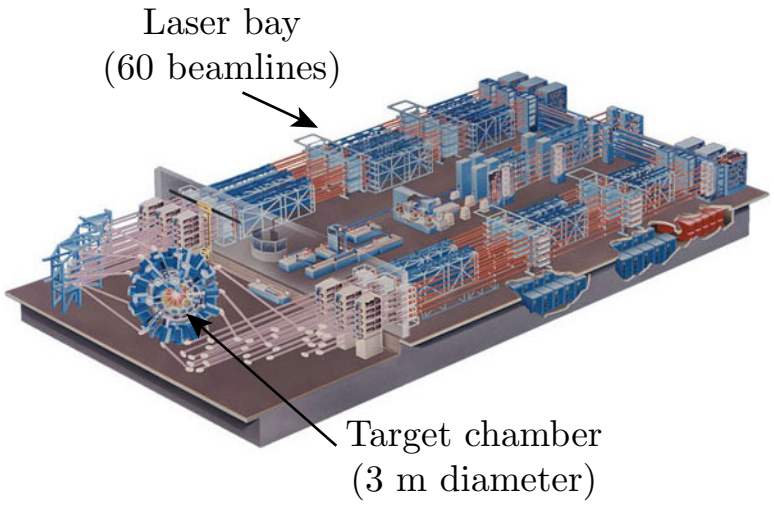

Figure 1.1: An illustration of the OMEGA laser facility, showing the independent beam lines and the experimental chamber. (Credit: Laboratory for Laser Energetics)

burning plasmas have yet to be achieved, HED physics remains an active and growing field, driven by increased access to HED facilties for more wide-ranging scientific exploration.

1.2 The OMEGA Laser Facility

The facility at which all experiments presented in this thesis were performed is the OMEGA laser facility, at the Laboratory for Laser Energetics in Rochester, New York. The OMEGA laser facility is a kiloJoule-class laser facility with 60 separate beamlines, each laser capable of delivering 500 J over a 1 ns square pulse, for a maximum intensity of $> 10^{14}$ W/cm^2.[5,6] The upgraded facility was built primarily to study the implosion of fusion fuel capsules by direct laser irradiation (direct-drive), and so the laser beamlines are arranged symmetrically about the spherical chamber. Over time, more exploratory science has been allowed at the facility, and it has become an increasingly valuable science facility for studying HED physics and laser-plasma interactions because of its flexibility and wide array of diagnostics.

1.3 Laboratory Astrophysics and Magnetohydrodynamic Scaling

Before the advent of nuclear physics, a persistent question was how stars generated their energy. We now know that the answer is nuclear fusion, driven by the great gravitational forces experienced at the core of stars. In some sense, fusion (and fission) research was founded on astrophysical considerations, and the desire to understand and harness these processes. As achieving HED conditions in a strictly controlled manner became possible with laser facilities[2], more direct connections could be made to astrophysical systems. Starting in 1999, a number of papers — notably Ryutov et al. (1999), Ryutov et al. (2000), Ryutov et al. (2001), and Ryutov and Remington (2002) — reasoned that through proper scaling of experimental parameters, the physics of energetic, large-scale astrophysical processes could be explored in analogous, small-scale, highly energetic, short-lived laboratory experiments in what has become known as laboratory astrophysics.[7,11,12,8,13,9,10,14] Since then, many more experiments have been performed to explore a wide range of astrophysically relevant processes.

An important aspect of many astrophysical plasmas is that, by nature of the vast distances, low densities, and long time scales involved, they typically behave magnetohydrodynamically, meaning that the evolution of these plasmas can be significantly affected by magnetic fields. As the implementation of magnetic fields has become streamlined at HED facilities (e.g. due to the availability of MIFEDS at OMEGA[15,16]), so too has the number of experiments exploring astrophysically relevant magnetized plasma systems. Recent experiments have explored a wide range of astrophysically relevant, magnetized plasma systems: the interaction of collisionless flows to create collisionless shocks[17–31], driven magnetic reconnection in laser-produced plasmas[32,33], the amplification of magnetic fields by turbulent dynamo action[34,35], and shocks formed by magnetized plasmas[36,37], among others. The work presented in this thesis concerns two separate astrophysical processes. The first, discussed in Section 1.6 and later in Chapters 4 and 5, is the formation of detached bow shocks around magnetized astrophysical bodies. The second, discussed further in Section 1.5 and in Chapter

3, deals with the formation of small-scale current filaments in the interaction of collisionless plasmas via the Weibel instability.

To understand how the physics of astrophysical systems may be scaled to laboratory experiments, it is necessary to review the governing equations of magnetohydrodynamics (MHD). The MHD equations are an extension of the typical hydrodynamic (Euler) equations to include the conservation and evolution of magnetic fields, and are commonly provided in plasma physics and astrophysics texts.[38,1,39–41] For simplicity I will confine the discussion here to resistive MHD and neglect contributions from other extended MHD effects, although the Hall effect may be important in collisionless plasma systems. The conservation of mass, or continuity, equation requires no modification from hydrodynamics, and is

$$\frac{\partial \rho}{\partial t} + \nabla \cdot (\rho \underline{u}) = 0, \tag{1.1}$$

where ρ is the plasma density, and $\underline{u}$ is the velocity of the plasma. The single underline notation will denote vectors throughout. The momentum conservation equation,

$$\rho \left(\frac{\partial}{\partial t} + \underline{u} \cdot \nabla \right) \underline{u} = \underline{j} \times \underline{B} - \nabla p, \tag{1.2}$$

now includes the effect of field components, where $\underline{j} = qn\underline{u}$ is the electric current density (q is the species electric charge and n is the species number density), $\underline{B}$ is the magnetic field, and p is the internal plasma pressure. The $\underline{j} \times \underline{B}$ term describes the effect of the electromagnetic force on the plasma, where $\underline{j}$ is determined from the resistive form of Ohm's law (in SI units) as

$$\eta \underline{j} = \underline{E} + \underline{u} \times \underline{B}, \tag{1.3}$$

where η is the resistivity of the plasma. The electric field $\underline{E}$ can typically be neglected when the plasma is not relativistic. The momentum equation can be further simplified by applying

Ampère's law

$$\mu_0 \underline{j} = \nabla \times \underline{B} \tag{1.4}$$

where μ_0 is the vacuum permeability, and which produces the expression

$$\rho \left(\frac{\partial}{\partial t} + \underline{u} \cdot \nabla \right) \underline{u} = \frac{1}{\mu_0} (\underline{B} \cdot \nabla) \underline{B} - \nabla \left(\frac{B^2}{2\mu_0} \right) - \nabla p, \tag{1.5}$$

in which the first term on the right hand side corresponds to a magnetic tension force, and it is apparent that the second term describes the effect of gradients in a magnetic pressure

$$p_B = B^2 / 2\mu_0. \tag{1.6}$$

Next, the induction equation describes the change of the magnetic field in time,

$$\frac{\partial \underline{B}}{\partial t} = \underbrace{\nabla \times (\underline{u} \times \underline{B})}_{\text{Advective term}} + \underbrace{\frac{\eta}{\mu_0} \nabla^2 \underline{B}}_{\text{Diffusive term}} , \tag{1.7}$$

which has terms corresponding to advection of the magnetic field with the plasma and diffusion of the field determined by the resistivity. In ideal MHD the plasma is assumed to be infinitely conductive, so the resistivity is zero, in which case the diffusion term disappears and the field is purely frozen into and advected by the plasma.

To close the relations, the energy (or entropy) equation is given by

$$\left(\frac{\partial}{\partial t} + \underline{u} \cdot \nabla \right) \left(\frac{p}{\rho^\gamma} \right) = 0, \tag{1.8}$$

in which a polytropic equation of state is assumed (pV^γ is constant), where V is a volume element and γ is the polytropic index. Finally, the divergence of the magnetic field must be zero,

$$\nabla \cdot \underline{B} = 0, \tag{1.9}$$

which is particularly important across shocks.

Now, how exactly can these equations be applied analogously to systems with such vast differences in spatial and temporal scales? Luckily, the MHD equations do not have any intrinsic scale requirements, and in fact, the scales are directly related to the plasma and field conditions, which allows for similarity scaling. Based on the initial values in the system, it is necessary to nondimensionalize the representations of density, pressure, velocity, and magnetic field. Following Ryutov et al. (2001), the usual derivation is as follows. First, define the chosen initial conditions

$$L^*, \quad \rho^*, \quad p^*, \quad u^*, \quad B^*, \tag{1.10}$$

as characteristic length, density, pressure, velocity, and magnetic field scales. The dimensionless variables are

$$\tilde{\underline{r}} = \frac{\underline{r}}{L^*}, \quad \tilde{\tau} = \frac{t}{L^*}\sqrt{\frac{p^*}{\rho^*}}, \quad \tilde{\rho} = \frac{\rho}{\rho^*}, \quad \tilde{p} = \frac{p}{p^*}, \quad \tilde{\underline{u}} = \underline{u}\sqrt{\frac{\rho^*}{p^*}}, \quad \tilde{\underline{B}}^2 = \frac{(\underline{B}^*)^2}{2\mu_0 p^*}, \tag{1.11}$$

where the tilde over each parameter indicates a dimensionless quantity, and the characteristic plasma pressure p^* is the primary scale for magnetic field considerations and is incorporated into the dimensionless time and velocities. With this choice of scaling, there are two key similarity parameters: the Ryutov number and the plasma beta.[1] The Ryutov number is defined as

$$\mathrm{Ry} = u^*\sqrt{\frac{\rho^*}{p^*}} \sim \frac{u^*}{c_s^*}, \tag{1.12}$$

and scales the hydrodynamics (and is analogous to the Mach number M), where c_s is the sound speed.[9] The plasma beta is defined as the ratio of magnetic pressure to thermal pressure

$$\beta = \frac{(B^*)^2}{2\mu_0 p^*}. \tag{1.13}$$

This formalism is widely applicable, but assumes that the magnetic fields of interest are

generally small and intrinsic to the plasma.

In many astrophysical cases, such as those concerning solar physics or the evolution of supernovae remnants, defining β with respect to internal fields and thermal pressure is acceptable. However, when dealing with the interaction of a flowing plasma and external magnetic fields, as in the experiments discussed in Chapter 4, the relevant parameters are not the thermal pressure and the internal magnetic pressure, but the kinetic energy density, or ram pressure, of the flowing plasma

$$p_{\text{ram}} = \frac{1}{2}\rho u^2, \tag{1.14}$$

and the *external* magnetic pressure acting against this flow. It is the bulk flow that impinges on the obstacle, not the randomized thermal motions, at least when $p_{\text{ram}} > p_{\text{therm}}$. In this case, the dimensionless magnetic field is represented as

$$\tilde{\underline{B}}^2 = \frac{(\underline{B}^*)^2}{\mu_0 \rho^* (\underline{u}^*)^2}. \tag{1.15}$$

From which a new dimensionless scaling parameter between systems is defined as the ratio of magnetic pressure to ram pressure

$$\beta_{\text{ram}} = \frac{B^2}{\mu_0 \rho u^2}. \tag{1.16}$$

It is this parameter which defines the dominant similarity when dealing with magnetized bow shocks in Chapter 4.

Additionally, when dealing with plasmas whose internal field pressure exceeds the thermal pressure it could be argued that the pressure to consider in the Ryutov number should be the magnetic pressure. In this case it is apparent that a new scaling parameter is the plasma

velocity in relation to the Alfvén velocity, the Alfvén number (or Alfvén Mach number)

$$M_A = \underline{u}^* \sqrt{\frac{\mu_0 \rho^*}{(\underline{B}^*)^2}} = \frac{u^*}{v_A}, \tag{1.17}$$

where the Alfvén velocity v_A describes the speed at which electromagnetic field information can travel in the plasma. The general information propagation speeds in a plasma really depend on the magnetosonic velocity, which is a combination of the sound speed and Alfvén speeds

$$v_{ms} = \sqrt{c_s^2 + v_A^2}. \tag{1.18}$$

However, the speed of a wave depends on the direction of the wave propagation with respect to the magnetic field, and from this directionality three types of waves are defined: the fast, slow, and intermediate magnetosonic waves, where the classification also depends on the relative sound and Alfvén speeds.[38,1] Waves travelling perpendicular to the magnetic field have a fast magnetosonic velocity $v_{fms} = v_{ms}$, which will be important when dealing with magnetized bow shocks. The presence of magnetic fields quickly complicates scaling considerations, because there are now multiple scales — both hydrodynamic and magnetohydrodynamic — which must be considered simultaneously. It is also necessary to consider the relative directionality of the field and velocity components — the topology of the system determines the interaction, with different speeds for transverse and longitudinal waves.

Although the above derivation considered ideal MHD, when dealing with a resistive plasma it is also important to consider the time scales over which diffusion occurs relative to advection to determine which one dominates. The plasma resistivity can be calculated as

$$\eta = \frac{4\sqrt{2\pi}}{3} \frac{Ze^2 \sqrt{m_e} \ln \Lambda}{(4\pi\epsilon_0)^2 (k_B T_e)^{3/2}} \ \Omega\text{m} \approx 1.03 \times 10^{-4} \frac{Z \ln \Lambda}{T_e^{3/2}} \ \Omega\text{m}, \tag{1.19}$$

where Z is the average charge state of the plasma, e is the electron charge, m_e is the electron mass, $\ln \Lambda$ is the Coulomb logarithm, ϵ_0 is the vacuum permittivity, k_B is the Boltzmann

constant, and T_e is the electron temperature (in units of eV on the right-hand side).[39] The diffusion coefficient η/μ_0 thus lends itself to calculation of a characteristic diffusion time scale

$$\tau_B = \frac{\mu_0 L^2}{\eta} = 1.22 \times 10^{-2} \frac{L^2 T_e^{3/2}}{Z \ln \Lambda} \text{ s}, \tag{1.20}$$

where L is a characteristic length scale (in meters).[1] In any system, the advective time scale is given by $\tau_{adv} = L/U$, where U is some bulk velocity. Therefore, to determine which of these two processes is dominant (over a given length scale), we can define another important similarity parameter — the magnetic Reynolds number — as the ratio of the magnetic diffusion and advective time scales

$$R_m = \frac{\tau_B}{\tau_{adv}} = \frac{\mu_0 U L}{\eta}. \tag{1.21}$$

When $R_m \gg 1$, diffusion dominates and resistivity is important, and when $R_m \ll 1$ diffusion is unimportant, and the system can be considered as mostly ideal MHD. In the cases when diffusion and advection are roughly equivalent, the dynamics depend greatly on the choice of length scales, and diffusion may be important over small scales, while the bulk evolution is determined by advection.

1.4 Magnetohydrodynamic Shocks

Since I will be dealing with MHD shocks in Chapter 4, it is important to define them in more detail. I will only present the results, but in-depth derivations can be found in Kantrowitz and Petshek (1966), Kulsrud (2005), Draine and McKee (1993), and Hartigan

(2003), and likely many other MHD texts. The shock jump conditions are

$$\text{Continuity: } \left[\rho \underline{u} \cdot \hat{n}\right]_1^2 = 0 \tag{1.22}$$

$$\text{Momentum: } \left[\rho \underline{u}\underline{u} \cdot \hat{n} + \left(p + \frac{B^2}{8\pi}\right)\hat{n} - \underline{B}\left(\frac{\underline{B} \cdot \hat{n}}{4\pi}\right)\right]_1^2 = 0 \tag{1.23}$$

$$\text{Energy: } \left[\frac{\rho u^2}{2}\underline{u} \cdot \hat{n} + \left(\frac{\gamma}{\gamma - 1}\right) p\underline{u} \cdot \hat{n} - \frac{(\underline{u} \times \underline{B}) \times \underline{B}}{4\pi} \cdot \hat{n}\right]_1^2 = 0 \tag{1.24}$$

$$\text{Parallel field: } \left[\underline{B} \cdot \hat{n}\right]_1^2 = 0, \tag{1.25}$$

in which $\hat{n}$ corresponds to the direction of the shock normal, where the large square brackets indicate the subtraction of the bracketed quantities evaluated on either side of the shock, with state 1 being the unshocked, upstream state, and state 2 being the shocked, downstream state. The direction of the shock with respect to the magnetic field determines the kind of shock, but I will only deal with perpendicular shocks, where the magnetic field is perpendicular to the shock normal, and thus has the greatest effect on the shock. In this case, the compression ratio across the shock is

$$C = \frac{\rho_2}{\rho_1} = \frac{B_{2\perp}}{B_{1\perp}} = \frac{u_{1\parallel}}{u_{2\parallel}} = \frac{2\left(\gamma + 1\right)}{D + \left[4\left(2 - \gamma\right)\left(\gamma + 1\right) M_A^{-2} + D^2\right]^{1/2}}, \tag{1.26}$$

where D is given by

$$D = \gamma - 1 + \frac{2}{M^2} + \frac{\gamma}{M_A^2}, \tag{1.27}$$

and contains the relative significance of the sound speed to the Alfvén speed.[43,44] It can be seen from equation (1.26) that in this ideal, perpendicular shock, the compression of the perpendicular magnetic field and the density are equivalent. Note that components of the magnetic field parallel to the shock normal cannot be amplified, but can undergo a rotational discontinuity in which the field rotates about the shock normal.

1.5 Collisionless Plasmas and the Weibel Instability

Because of the large spatial scales of astrophysical plasmas, astrophysical plasma dynamics are also typically collisionless. A collisionless plasma is a dynamic plasma system in which the hydrodynamic length scale is shorter than the collisional mean free path, and the effect of particle collisions is therefore negligible with respect to the dynamic evolution of the system. In such plasmas, interactions are purely electromagnetic, and new instabilities (including the Weibel instability) are possible. Collisionless plasmas can be created in a laboratory by the interaction of high-power lasers with solid targets.[45,17] Most intriguing about this category of plasmas is that collisionless plasmas can still sustain shocks, much like normal hydrodynamics, with the exception that the shock is mediated by the electromagnetic fields, rather than particle collisions.[38,41] In some cases, the field which sustains this interaction is intrinsic to one of the plasmas, and initial consideration for experiments studying these shocks by Drake (2000) included an applied magnetic field. However, collisionless shocks can also form in the interaction of initially unmagnetized plasmas. In this case, the fields required to sustain the shock are self-generated during the interaction of the plasmas.[17,46]

There are multiple processes by which the self-generation of magnetic fields is thought to occur in plasmas, but the mechanism of interest here is the Weibel (or filamentation) instability.[47] The Weibel instability occurs when a collisionless plasma exhibits an anisotropic velocity distribution of electrons and / or ions. The anisotropy drives the formation of filaments of electric current, which in turn set up small-scale magnetic fields, though the system is presumed to retain a zero-mean field when integrated over the interaction volume. The Weibel instability is also hypothesized to be the source of initial magnetization in the intergalactic medium.[48] The work of Park et al. (2012) and Drake and Gregori (2012) first put forward methods to experimentally generate collisionless shocks in unmagnetized plasmas using laser-produced plasmas. Since then, many experiments have been performed at the OMEGA laser facility[46,18,20,25,21] and the NIF to attain collisionless shocks. While the reported results from these experiments have yet to achieve the formation of true collisionless

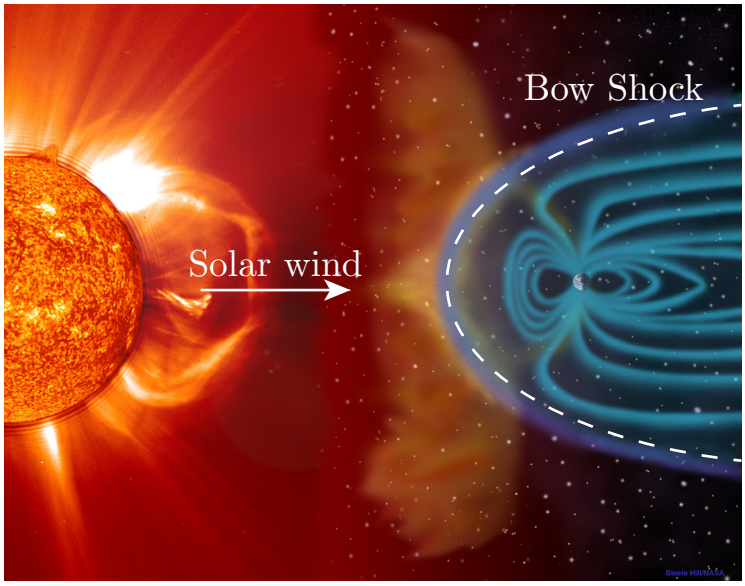

Figure 1.2: Illustration of the Sun-Earth system, showing a coronal mass ejection (CME) incident on the Earth's magnetosphere. The bow shock has been outlined. (Courtesy of SOHO/NASA consortium. SOHO is a project of international cooperation between ESA and NASA.)

shocks, filamentation and magnetic field generation consistent with the Weibel instability has been demonstrated in measurements made of the magnetic fields via proton imaging.[20,21,25]

1.6 Magnetospheres and Bow Shocks

The Sun, like all stars, emits a stream of charged particles outward, known as the solar wind. This wind is fast, yet incredibly diffuse, with an average velocity of 400 km/s and number density of 1 cm^{-3} measured at 1 AU, where it interacts with the Earth. The Earth has an intrinsic magnetic field, generated by the dynamo action of iron in the core and mantle can be approximated as a dipolar field as

$$B(r,\theta) = \left(\frac{M}{r^3}\right)\sqrt{1+3\cos^2\theta}, \tag{1.28}$$

where r is the radial distance from the center of the Earth, θ is the azimuthal angle, and M is the magnetic dipole moment, which has a typical value of approximately 8×10^{15} T

m^3, providing a mean equatorial value of approximately 30 μT at the surface. Importantly, the strength of this field decreases very quickly, inversely with the cube of the radius. The Earth's magnetic field may therefore seem relatively weak for terrestrial purposes (aside from its use in navigation), but it exerts sufficient pressure to oppose the solar wind at an average distance of 10 Earth radii.[49] The pressure-balance surface in the Earth-Sun system is known as the magnetopause, and is the effective obstacle to the solar wind, rather than the planet's surface. Similar to standing, detached gasdynamic shocks upstream of a blunt body, a standing bow shock exists at an average standoff distance of 3 Earth radii upstream from the magnetopause.[49] At the leading edge, the bow shock is a quasi-perpendicular, fast magnetosonic shock, in which the information speed is the fast magnetosonic speed as discussed in Section 1.3 and follows the jump conditions presented in Section 1.4.

The interaction of the solar wind with the Earth's magnetosphere is collisionless. It may seem confusing at first that a collisionless plasma flow experiences an effective pressure, but because of the large scales (multiple Earth radii) over which these dynamics occur with respect to the electron and ion gyroradii, the bulk of the interaction is magnetohydrodynamic. For example, the solar wind does indeed behave kinetically across and through the bow shock, with a thickness defined by the gyroradius of the impinging ions, which is on the order of a few hundred kilometers.[38] However, because the gyroradii are small compared to the ≈ 10 Earth radii scale of the magnetopause, the ions can be significantly redirected by the field, so the location of the magnetopause agrees well with simple pressure balance between the ram and magnetic pressures. Between the bow shock and the magnetopause is the magnetosheath, a region of shocked solar wind plasma as it is redirected around the magnetopause. Because of the Earth's magnetic field, the solar wind does not typically penetrate beyond the magnetopause, although there is speculation that instabilities like Kelvin-Helmholtz waves along the surface of the bow shock and magnetopause could transport the solar wind plasma to the interior of the magnetosphere.[50]

The solar wind is highly variable, with characteristic speeds and densities changing by

more than a factor of 2, corresponding to solar cycles and energetic events in the corona, the origins of which are an active research area.[51] As the solar wind fluctuates, the bow shock and magnetopause contract further toward the planet in the case of increased solar wind energy, or relax farther out in the case of decreased solar wind energy, following the requirements of pressure balance. This shifting balance does not usually affect life on the surface, but extremely energetic events (coronal mass ejections) on the sun can produce geomagnetic storms when this plasma reaches the Earth, during which the magnetosphere rapidly compresses and relaxes. If the storms are energetic enough, the rapid change in magnetic field can induce currents in terrestrial and orbiting electronics, which can cause significant damage. The worst such storm since the advent of electronics, known as the Carrington event, occurred in 1859 and induced strong enough currents to short telegraph lines throughout North America.[52,53] Indeed, it was this event (and resulting aurora) which first led scientists to consider that the sun emitted a constant stream of charged particles.[52] Decades of satellite measurements inform empirical models and complex computational models of the Earth's magnetosphere. Scaled experiments may provide additional ways to explore how magnetized obstacles respond to an incoming plasma flow and thus broaden our understanding of the physical processes which occur in the magnetosphere. Such experiments can provide advantages like controllable system parameters and a wide array of diagnostics, in comparison to more passive satellite measurements.

1.7 Proton Imaging

The previous two sections encompass the physics and motivation for the experiments considered in this thesis. This thesis has a broad, overarching theme of studying magnetic fields in laboratory astrophysics experiments, and there is another fundamental link: the method by which the magnetic fields are measured — proton imaging. Proton imaging is a powerful technique for visualizing electromagnetic fields of an experimental system, in which the deflections of probe protons by electromagnetic fields produce spatial variations of inci-

dent fluence on the image, which encode information about the integrated field topology and strength. High-energy (> MeV) probe protons are able to pass through low-density plasmas with minimal scattering due to particle collisions, and can thus probe the electromagnetic fields. Proton imaging has widespread usage among magnetized HED plasma experiments, including in collisionless shock[20,25] and magnetic reconnection[32] experiments.

However, the degree to which proton images can be usefully analyzed depends entirely on how well the magnetic field geometry is known and the relative strength of the field. Indeed, since the image is primarily determined by the orientation of the fields with respect to the trajectories of the probe protons, careful consideration of the geometry must be made in any experiment.[54] Most basically, the field strength determines the degree to which protons are deflected, described by two main regimes of proton imaging: the linear regime and the caustic regime. In the linear regime, proton deflections are very small, and deflected trajectories do not cross before they reach the image plane. In the caustic regime, proton trajectories do overlap, resulting in very large variations in intensity. When caustics are present, the inherent nonlinearity complicates inference of field strength and structures unless there are known symmetries. The analysis techniques that can be applied to proton images is quite different among the two regimes, but some similarities do emerge. Because this diagnostic technique is central to the work of this thesis, I present a detailed account of the basic physics, experimental techniques, and image analysis techniques for proton imaging of magnetic fields in Chapter 2.

1.8 Thomson Scattering

Thomson scattering is the scattering of light by electrons, and when using a laser of known frequency, this phenomenon can be used to infer plasma parameters by measuring the spectrum of Thomson-scattered light.[55,56] There are two primary regimes of Thomson scattering, the collective regime and the noncollective regime, which determine how the light scatters from the plasma.[55] In the collective regime, which occurs when the probe

frequency is not significantly less than the plasma frequencies, the probe beam excites waves in the plasma — specifically, electron plasma waves and ion acoustic waves. When the probe scatters from the excited plasma waves, the light is up- or down-shifted in frequency corresponding to the frequency of these waves. Noncollective scattering occurs when the probe laser frequency is much greater than the plasma frequencies. In this case, the laser does not generate coherent waves in the plasma, the scattering is instead a result of direct interaction with individual electrons, providing a measure of their thermal distribution. The work presented in this thesis (e.g. Chapter 4) only deals with collective Thomson scattering, so I will restrict further discussion to that regime.

Knowing the general relation between the frequency of the plasma waves in collective Thomson scattering, plasma parameters can be inferred from the frequency shifts measured on the spectrometer. The fully general Thomson-scattered spectral density function is

$$S(\underline{k},\omega) = \frac{2\pi}{k}\left|1-\frac{\chi_e}{\epsilon}\right|^2 f_{e0}\left(\omega/k\right) + \frac{2\pi}{k}Z\left|\frac{\chi_e}{\epsilon}\right|^2 f_{i0}\left(\omega/k\right), \tag{1.29}$$

where k is the laser wavenumber, ω is the scattered frequency, χ_e is the electric susceptibility, ϵ is the permittivity of the plasma, Z is the average charge state, f_{e0} is the initial electron distribution function, and f_{i0} is the initial ion distribution function.[55] The scattered power can be determined S, from which exists a method of determining the complete Thomson scattered spectrum from a plasma.[55] The method presented in Froula et al. (2011) for determining fits to scattered spectra is followed in the analysis of Thomson scattering data presented in Chapter 4. However, it is often useful (and usually accurate) to simplify the expression and infer plasma parameters by the measured peak scattering frequencies.

First, consider the features produced by the electron plasma waves. The plasma waves excited by the laser is described by the Bohm-Gross dispersion relation

$$\Delta\omega = \sqrt{\omega_{pe}^2 + 3k_0^2 v_{Te}^2}, \tag{1.30}$$

where ω_{pe} is the electron plasma wave frequency, k_0 is the wavenumber of the probe laser, and v_{Te} is the thermal electron velocity. The electron plasma wave frequency is (in SI units)

$$\omega_{pe} = \sqrt{n_e e^2/m_e\epsilon_0} = 5.64 \times 10^4 \sqrt{n_e\ (\mathrm{cm}^{-3})}, \tag{1.31}$$

where n_e is the electron number density (in units of $1/\mathrm{cm}^3$), e is the fundamental electron charge, m_e is the electron mass, and ϵ_0 is the vacuum permittivity. The thermal electron velocity is

$$v_{Te} = \sqrt{k_B T_e/m_e} \approx 4.19 \times 10^5 \sqrt{T_e\ (\mathrm{eV})}\ \mathrm{m/s}, \tag{1.32}$$

where k_B is the Boltzmann constant, and T_e is the electron temperature in eV. In most cases of interest (like those considered in this thesis), the electron plasma wave is the primary component of the excited wave, so the Thomson-scattered frequency peaks are highly dependent on changes in electron number density. A similar procedure can be followed for observing ion waves, but there are additional complications arising from the need to account for ionization states and the presence of multiple species.

The natural measurement from the spectrometers used in the work of this thesis is in wavelength space. Typically, when n_e is large enough, two Thomson-scattered peaks of are observed on the spectrometer, and the difference in wavelength between these peaks (or difference between one peak and the laser wavelength) is used to determine the plasma parameters. After converting to wavelength space, the wavelength shift between the two peaks is related to the excited wave by

$$\Delta\lambda = 2\pi c \left(\frac{1}{\omega_0 - \Delta\omega} - \frac{1}{\omega_0 + \Delta\omega} \right), \tag{1.33}$$

where $\omega_0 = k_0 c$ is the angular frequency of the laser. There are more detailed formalisms to describe the entire Thomson-scattered spectrum in a plasma given by[56,55,57,58] which use the full scattered spectral density function and assume a Maxwellian temperature distribution.

The full spectral density method is used to fit plasma parameters in Chapter 4, but the overall result is mostly reliant on scattered peak positions as described above. In general, increasing n_e increases $\Delta\lambda$ while reducing the width of the peaks, and increasing v_{Te} primarily increases the width of the peaks, while also increasing $\Delta\lambda$.

The OMEGA laser facility has a robust optical and ultraviolet Thomson scattering system which includes two spectrometers, one to measure the electron feature and one to measure the ion feature. These spectrometers can be run in either a time-resolved, spatially integrated (streaked)[57] or a time-gated, spatially resolved (imaging)[59,60] configuration. The Thomson probe laser can be run in either the 2ω (526 nm) or 4ω (263 nm) modes, where the lower frequency is typically used for plasmas of number density $< 10^{20}$ cm^{-3} and the higher frequency is used to probe more dense systems ($\leq 10^{21}$ cm^{-3}). Only 2ω Thomson scattering was used for the work in this thesis.

1.9 Summary of Chapters

Chapter 2 provides a more detailed description of proton imaging, and derives how images are formed from proton deflections. Chapter 3 covers the computational and analytic analysis of proton images of statistical magnetic fields generated by the Weibel instability to determine what information of the underlying three-dimensional structure can be recovered from the two-dimensional images. Chapter 4 details the primary experimental foundation of this thesis: the magnetized bow shock experiments performed at the OMEGA laser. This chapter presents the theoretical backing, experimental design, and data analysis from these experiments. Chapter 5 follows up on the work presented in Chapter 4 and provides more information about the use of results from simulations using the FLASH code in relation to analyzing the bow shock experiments. Chapter 6 concludes the thesis, with some thoughts about how the bow shock experiments could be improved, and about the proper interpretation of proton images.

1.10 Contributions

In this section I describe the contents of each of the following chapters and explicitly describe the contributions I have made to the work presented, as well as work that may not have been included.

Chapter 2: Proton imaging of electromagnetic fields has been in use for perhaps twenty years, with increased usage over the last five or so years as techniques have evolved. I have expanded analysis from the typically simplified assumptions of collimated proton probing to include the effects of realistic, diverging proton sources. This aspect is critically important for fully capturing resulting proton images, because off-axis velocity components can (and often do) cause significant deflection contributions when interacting with the field, depending on the system geometry. Additionally, I have performed more analytic analysis of the deflections, considering symmetries and how to interpret and infer field information from a specific caustic image feature: the features created by the defocusing of protons when probing the fields generated by a current-carrying wire, in which the protons travel primarily antiparallel tot he direction of current in the wire.

Chapter 3: Experiments and simulations had already been performed to probe the magnetic fields which self-generate during the interaction of two counter-propagating collisionless plasmas. However, it was not previously known how the observed proton image features related to the internal distribution of the filamentary fields. It was commonly assumed that the effective wavelength between the small-scale, repeated filamentary features on the proton images would correspond to some effective wavelength of the spacing between the many real filaments which the protons interact with, either in one or two dimensions. Working with Frederico Fiuza, I was responsible for determining how proton images of systems of many filamentary magnetic fields from the collisionless shock (Weibel instability) correspond to the internal field structures. I explored this problem computationally and analytically and determined that the common assumption was incorrect. I determined that there was indeed a relation between internal field properties and the proton images in the linear deflection

regime. In the small-deflection regime of proton imaging, the effect of the very small individual filaments is almost negligible over the scale of the filament itself, and so the contribution to the image from each filament is cumulative; the image is essentially a summation of image functions. Using this assumption, the Fourier spectrum of the final image corresponds to the Fourier spectrum of the summation of the individual image functions. By using a specific form of the filamentary magnetic fields, I derived an analytic relation between the dominant wavelength on the proton image and the constituent filaments: the spacing of the image features inherently depends on the *size* of the filaments and *not* on the spacing between them. However, if a certain packing of the filaments is assumed, the spacing may be inferred from the filament size. This analysis was borne out by computational analysis of the proton images from many, randomly generated, synthetic fields containing many filaments as well. Along with the new analytic relation, I provided a method to determine the size of the constituent filaments (and an approximate spacing between them when assuming a close-packed system of many filaments) via Fourier analysis of the image features. This new analysis and method should allow better interpretation (and reinterpretation) of the experimental results to more accurately infer magnetization and compare to full particle-in-cell (PIC) simulations. This work was published in Levesque et al. (2019).

Chapters 4 and 5 discuss work performed as part of an experimental campaign to create bow shocks due to the influence of external magnetic pressure on a plasma flow was carried out at the OMEGA laser facility. Chapter 4 deals with the experimental results and combined analysis. Chapter 5 details work done to simulate the physics of this experiment using the FLASH code. This campaign was a collaboration between Carolyn Kuranz at the University of Michigan and Patrick Hartigan from Rice University as part of the NLUF program. Two shot days focused on creating a suitable plasma flow for the experiment had been performed prior to my joining the project. Upon joining, I was assigned to be the PI for the final two shot days, which included: designing the targets, which diagnostics to use and their positioning, choice of beams and positioning, target characterization, and properly executing

the shot plan. I was also responsible for analyzing the data: proton images and Thomson-scattered spectra. Because of the lack of extra shot time and too much variability of observed features in the data, I decided to explore simulating the experiment using the FLASH code, a modular MHD code with optional extended MHD, multigroup radiation diffusion, tabulated equation of state (EOS) and opacities, laser energy deposition, and heat conduction. These simulations provided much qualitative assurance as to the physics of the system, but I faced many limitations and barriers in quantitatively matching results to the data.

CHAPTER 2

Proton Imaging of Magnetic Fields

Proton imaging is a central component of this thesis, so this chapter provides a detailed account of how proton images are formed, considerations for system geometry, and some methods of inferring field information from the images. We first explore the basics of proton imaging in terms of proton sources, detectors, and deflections in Section 2.1. Section 2.2 then analytically describes how proton images are formed in the linear imaging regime, and defines some typical proton imaging geometry considerations. Section 2.3 further derives the intensity map of proton images when assuming a collimated source of protons, as many papers do. Methods of incorporating the effects of a more realistic, diverging proton source are then covered in 2.4. Section 2.5 briefly describes the formation of caustics on proton images, and how their presence can impede analysis. Section 2.6 compares the effect of using a collimated or diverging source for two magnetic field geometries of interest — a Gaussian ellipsoid of magnetic in Section 2.6.1, and the magnetic field produced by a current-carrying wire in Section 2.6.2. Section 2.7 briefly addresses techniques for reconstructing the path-integrated magnetic fields from a proton image, and the limits of such methods. Finally, section 2.8 concludes the chapter with a brief discussion of the general way to analyze proton images, and gives a look forward to how some of the methods presented in this chapter are applied to the work in Chapters 3 and 4.

2.1 Physics Background

There are few methods available for nonperturbatively probing the amplitude and topology of small-scale magnetic fields which evolve on nanosecond timescales. The lack of tools comes from physical constraints, and there are relatively few means of physically interacting with electromagnetic fields, besides. A magnetic induction probe, for example, is a device that measures the current induced in a loop of wire by an external magnetic field. These probes provide measurements of the field amplitude at a single postion, spatially integrated over the size of the probe, and are typically too large for use in the systems of interest for this thesis — high-energy-density experiments at OMEGA. Another option is measuring the Faraday rotation of laser light, in which the polarization of light propagating parallel to magnetic field lines rotates in proportion to the amplitude of the field. Assuming the system is well-characterized, the path-integrated field strength can be inferred from the measured rotation. This technique (depending how it is set up) can also provide spatially resolved measurements, a distinct advantage over induction probes. However, rotation angles in small-scale experiments are typically very small by nature of the limited extent (and usually amplitude) of the fields[62,34], and can thus be challenging to constrain.

Thus, we come to charged particles — specifically, high-energy protons, as might have been assumed from the title of this chapter — to probe magnetic fields. Protons are a good candidate for investigating electromagnetic fields by nature of being charged particles and because their large mass relative to electrons allows high-energy (>MeV) protons to pass through low-density plasmas with minimal scattering by particle collisions. The probe protons are deflected from their initial trajectories primarily by interacting with the electromagnetic fields in some system, which produces spatial variations of incident fluence (via proton capture) on an image surface. The resulting image features encode information about the integrated field topology and strength.[54] These features depend on both the total amplitude of the field and the orientation of the field with respect to the proton's velocity along its trajectory. The geometry dependence, in many cases, is the driving factor of the

resulting images, and it therefore becomes difficult to generalize structures or methods of analysis. However, a general procedure can be followed to analyze images.

There are two methods available to produce protons at the OMEGA (and OMEGA EP) laser facility, and so I will limit my work to those methods. The first is Target-Normal Sheath Acceleration (TNSA), which produces a distribution of protons whose energies exceed 1 MeV when a high-intensity, short-pulse laser (typically on the order of 1 ps) irradiates a solid target.[63,64] The laser-plasma iteraction at the surface of the target generates relativistic electrons which stream away from the surface, and the resulting charge imbalance creates a sheath field which then accelerates protons to relativistic energies as well.[64] The protons travel through the system of interest, gaining deflections, and are typically captured by a radiochromic film (RCF), forming visible features on the film because of the large proton fluence of the source. The large range of proton energies essentially creates a time series of images, where proton energy and time are determined by depth of film in the stack. However, the broad range also causes some of the closer, lower-energy images to exhibit features from the higher-energy protons passing through that film, and disentangling these features can be difficult.

The second method — the method used in the experiments presented in this thesis — is to produce protons by imploding a small, nominally 400 μm diameter, D^3He capsule, by uniformly (or nearly uniformly) irradiating the sphere with ≥ 17 high-intensity lasers.[65] The implosion causes the fuel to fuse, producing 3 MeV protons as a product of DD reactions and 15 MeV protons as a product of D^3He reactions. Because two well-characterized, and distinct proton energies are produced by the implosion, this method has the distinct advantage of producing two clean images of the experiment per shot, one corresponding to each energy. The protons in this method are captured by a CR-39 proton track detector.[65] CR-39 images requires a time-consuming etching process, by which the pits caused by proton impact are enlarged, after which the etched CR-39 is scanned to create an image of proton fluence based on the counted number of pits. CR-39 images are also typically of much coarser resolution

Figure 2.1: An optical caustic formed by the cylindrical reflecting surface of a coffee cup.

than film, but the flux of protons generated by capsule implosion is generally insufficient to produce film images. Although each method has advantages, the primary consideration driving the use of this more convoluted procedure for imaging on the OMEGA 60 facility is the lack of a dedicated short-pulse laser.

Although proton imaging had been implemented since at least the reporting of Mackinnon et al. (2004), the first quantitative treatment of analysis techniques for proton imaging of electric and magnetic fields was provided by Kugland et al. (2012). Because the images are determined by field topology, Kugland et al. (2012) considers a number of specific cases of electric and magnetic field topologies, the influence of increasing field amplitude, and some effects of orientation of the probe protons with respect to the field. Perhaps most importantly, that paper addresses the onset and effect of caustic image features — nonlinearities of imaging intensity. Proton image caustics are similar in structure to optical caustics by nonuniform optics, such as in a coffee cup (see Figure 2.1) or on the bottom of a pool.[67] Proton image caustics arise when the gradient of deflections become large and at least some proton trajectories cross by the time they reach the image, producing regions of greatly increased proton flux. The presence of caustics can significantly impede analysis, because

there is not necessarily a unique solution due to the nonlinearity of the proton trajectories with respect to initial trajectory. However, if the system exhibits an advantageous symmetry (as in the case of the field of a current-carrying wire that I explore in section 2.6.2 and later in the bow shock experiments described in Chapter 4) the caustics may at least be predicted and provide a quantitative measurement.

I will next work out the basics of proton deflections by electromagnetic fields and how image features are produced from these deflections. The derivation first follows the derivation presented by Kugland et al. (2012) which, aside for some limited consideration of image magnification, essentially assumes a collimated source of protons for simplicity. Following that, I extend the analysis to include the effects of a more realistic, diverging point source of protons. The deflections from electromagnetic fields are determined by the effect of the Lorentz force

$$\underline{F} = m\frac{\partial \underline{v}}{\partial t} = q\left(\underline{E} + \underline{v} \times \underline{B}\right), \tag{2.1}$$

in which F is the force, m is the mass of the particle, v is the velocity of the particle, q is the electric charge, E is the electric field, and B is the magnetic field, where the single underline notation denotes vector quantities — which I will use throughout.

Equation (2.1) shows that deflections by the magnetic field are only caused by the field components *transverse* to the proton velocity, and the force is directly proportional to the velocity of the particle. Fortunately, magnetic fields act to deflect charged particles in such a way as to cause rotation about the field lines while conserving particle energy, which provides some simplicity in analysis. The primary geometrical consideration in any proton imaging setup is, therefore, the orientation of the probe axis with respect to the magnetic field. Integrating Equation (2.1) over the time of flight within the system, the change in velocity of a proton is

$$\Delta\underline{v} = \frac{q}{m_p}\int_{t_1}^{t_2}\left(\underline{E} + \underline{v} \times \underline{B}\right)\mathrm{d}t, \tag{2.2}$$

where m_p is the proton rest mass, and the time integration bounds t_1 and t_2 represent the

time of flight within the interaction region. For the moment, I will simplify the system by assuming that the velocity and electromagnetic fields are constant within the interaction region. The primary concern is the transverse deflection, and the change in the perpendicular velocity components can be written as

$$\Delta v_\perp = \frac{q}{m_p}\left(E_\perp + v_0 B_\perp\right)\Delta t = \frac{q}{m_p}\left(\frac{E_\perp}{v_0} + B_\perp\right)\Delta L, \tag{2.3}$$

where v_0 is the initial proton velocity, $B_\perp$ is the transverse magnetic field, and Δt is the time it takes to cross the interaction region, which can also be defined in terms of the distance across the interaction region $\Delta L = v_0 \Delta t$. In this simplified case I also assume that the added energy by interaction with the electric fields is negligible, to maintain conservation of energy (further reason for this simplification will be made clear momentarily). The deflection angle α of a proton trajectory in this simplified form is thus

$$\alpha = \tan^{-1}\left(\frac{\Delta v_\perp}{v_0}\right) = \frac{\Delta v_\perp}{v_0}, \tag{2.4}$$

which we can also write as a function of the proton energy $E_p = m_p v_0^2/2$,

$$\alpha = \frac{2q\Delta L}{E_p} E_\perp + \frac{q\Delta L}{\sqrt{2 m_p E_p}} B_\perp. \tag{2.5}$$

In this form, it is immediately apparent that electric field deflection will be a factor of $\sqrt{E_p}$ smaller than magnetic field deflection. The work of this thesis is only concerned with systems in which the magnetic field is much greater than the electric fields, and the protons travel at relativistic speeds (further reducing the effect of electric fields), so I will restrict the rest of the analysis in this chapter to deflections by magnetic fields.

To more properly evaluate the integral of the magnetic field interaction in equation (2.2) it is necessary to consider that the velocity does change as it interacts with the fields. I will continue to assume that the magnetic field is not changing in time, but has a varying spatial

geometry, which the protons experience as they travel across this field. In some cases it is more useful to express the field as the curl of the vector potential $\underline{A}$,

$$\underline{B} = \nabla \times \underline{A}, \tag{2.6}$$

where we assume a Lorenz gauge, and that the vector potential is constant in time. Along with the above assumptions, I rewrite the change in proton velocity in terms of the vector potential

$$\Delta \underline{v} = \frac{q}{m_p} \int_{t_1}^{t_2} \underline{v} \times (\nabla \times \underline{A}) \, \mathrm{d}t = \frac{q}{m_p} \int_{t_1}^{t_2} \left[\nabla \left(\underline{v} \cdot \underline{A} \right) - \left(\underline{v} \cdot \nabla \right) \underline{A} \right] \mathrm{d}t, \tag{2.7}$$

which, when expanding into components provides an insightful representation

$$\Delta v_i = \frac{q}{m_p} \int_{t_1}^{t_2} \left[v_j \frac{\partial}{\partial x_i} A_j - \left(v_j \frac{\partial}{\partial x_j} \right) A_i \right] \mathrm{d}t, \tag{2.8}$$

where Einstein subscript notation has been applied. Expanding this out in all components can provide some further insight

$$\Delta v_x = \frac{q}{m_p} \int_{t_1}^{t_2} \left[v_y \frac{\partial}{\partial x} A_y + v_z \frac{\partial}{\partial x} A_z - \left(v_y \frac{\partial}{\partial y} + v_z \frac{\partial}{\partial z} \right) A_x \right] \mathrm{d}t \tag{2.9}$$

$$\Delta v_y = \frac{q}{m_p} \int_{t_1}^{t_2} \left[v_x \frac{\partial}{\partial y} A_x + v_z \frac{\partial}{\partial y} A_z - \left(v_x \frac{\partial}{\partial x} + v_z \frac{\partial}{\partial z} \right) A_y \right] \mathrm{d}t \tag{2.10}$$

$$\Delta v_z = \frac{q}{m_p} \int_{t_1}^{t_2} \left[v_x \frac{\partial}{\partial z} A_x + v_y \frac{\partial}{\partial z} A_y - \left(v_x \frac{\partial}{\partial x} + v_y \frac{\partial}{\partial y} \right) A_z \right] \mathrm{d}t. \tag{2.11}$$

An important aspect of the vector potential notation is that deflections in any direction depend on the interaction of the orthogonal velocity components with either the gradients of the same orthogonal component of the vector potential with respect to the direction of deflection (i.e. v_y interacts with A_y), or the gradients of the vector potential component in

the direction of deflection along the orthogonal axes. As I will show in Section 2.6.1, there are some cases, like when the vector potential only has one component, in which using the vector potential is much simpler than using the magnetic field when calculating deflections.

2.2 Proton Imaging in the Small-Deflection Regime

In this section I consider the case of proton imaging in the small-deflection — or linear — regime. In this regime proton trajectories do not intersect one another (at least not before reaching the image plane), and there exists a functional form for determining the image intensity profile. Before proceeding, it is important to set up a general system geometry. For simplicity, I define the proton probe-image axis to be the positive y-axis and the object and image planes are defined by (x, z), as illustrated in Figure 2.2. I will use as this the general system geometry throughout this thesis, except when specified otherwise. These coordinates are simply a matter of preference — I prefer to preserve a right-handed coordinate system which maintains that positive x is to the right and positive z is up.

As presented by Kugland et al. (2012), a surface element of proton intensity dS_I on the image plane can be defined relative to the change of the element dS_0 from an object plane as

$$dS = \frac{\partial(x_I, z_I)}{\partial(x_0, z_0)} dS_0. \tag{2.12}$$

When applied to the total intensity map, where total intensity is conservative, the two-dimensional image profile can be determined analytically by dividing the initial proton intensity map by the Jacobian determinant of the final proton positions with respect to their initial position[54]

$$I(x_I, z_I) = I_0 \frac{dS_0}{dS_I} = I_0(x_I, z_I) \left[\frac{\partial(x_I, z_I)}{\partial(x_0, z_0)} \right]^{-1}, \tag{2.13}$$

where I_0 is the initial intensity map of the proton source (which is typically assumed to be uniform), (x_I, z_I) represent proton positions at the image plane (subscript I), and (x_0, z_0) represent the initialized proton positions at some plane prior to deflection. Essentially, the

image is determined by the functional change in proton positions on the image with respect to their unperturbed positions.

It is thus necessary to determine the deflected proton positions as a function of initial position. Because the deflection angles are assumed to be small for the moment, the position of the protons at the image in this regime can (more or less) be accurately determined by applying the effect of the deflection angle in a single "kick" at the end of the interaction region and then propagating the protons with their new trajectories to the image plane. On the image plane (x_I, z_I) the final image positions can be represented as

$$x_I(x_0) = \frac{L_{OI}}{L_O} x_0 + L_{OI} \sin\left(\alpha_{x,I}\right) \tag{2.14}$$

$$z_I(z_0) = \frac{L_{OI}}{L_O} z_0 + L_{OI} \sin\left(\alpha_{z,I}\right), \tag{2.15}$$

where L_O is the distance from the proton source to the center of the object region, L_{OI} is the distance from the center fo the object region to the image, and $\alpha_{x,I}$ and $\alpha_{z,I}$ correspond the angles of the proton's trajectory in the xy and yz planes, respectively, after interacting with the field.

Equation (2.14) can be further expanded to include the effects of a diverging proton source by adding the components of the initial proton trajectories $\alpha_{x,0}$ and $\alpha z, 0$ as

$$x_I(\alpha_0) = L_O \sin(\alpha_{x,0}) + L_{OI} \sin(\alpha_{x,I}) \tag{2.16}$$

$$= L_O \sin(\alpha_{x,0}) + L_{OI} \sin(\alpha_{x,0} + \Delta\alpha_x) \tag{2.17}$$

$$\approx L_I \alpha_{x,0} + L_{OI} \Delta\alpha_x, \tag{2.18}$$

where I have assumed that the angles $\alpha_{x,0}$ and $\Delta\alpha_x$ are sufficiently small. For practical purposes, the x_0 formalism and $\alpha_{x,0}$ formulation are equivalent if all components of the trajectory are considered. However, in application there are situations for which it is advantageous to use one over the other based on the system geometry. The choice of coordinates

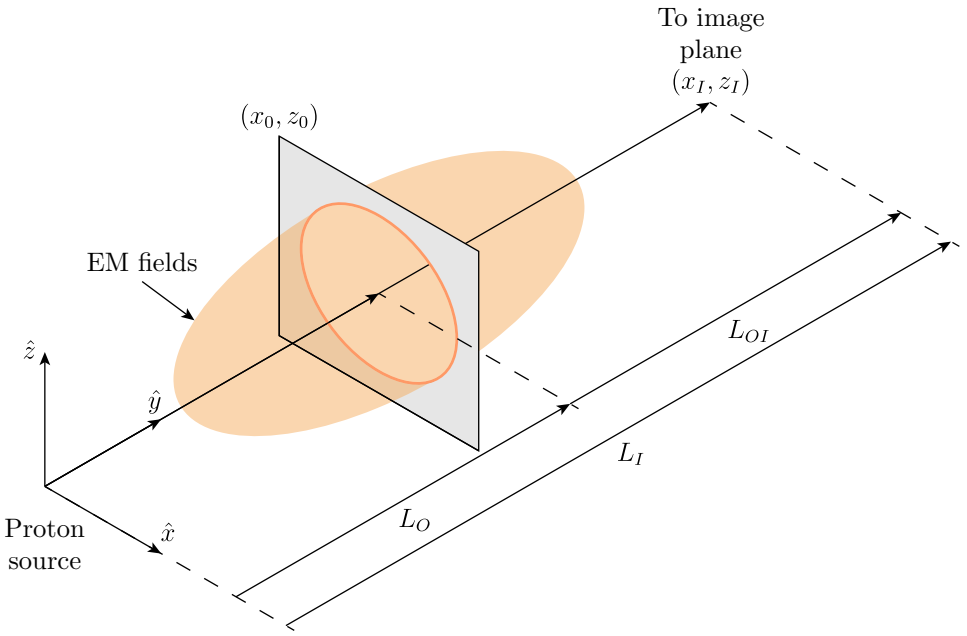

Figure 2.2: The general proton imaging geometry in Cartesian coordinates (no scale assumed). The center of the interaction is defined as the object plane, at a distance L_O from the proton source along the imaging axis. The image plane is a distance L_{OI} from the object plane.

also depends on the desired level of fidelity, i.e. whether to model the source as a point source or as a collimated source; I discuss both in the next two sections.

2.3 Proton Imaging With a Collimated Source

The simplest method of approaching proton images is to assume that the protons are initially collimated — they all have the same trajectory along the imaging axis, with some spatial variance in the initial positions (x_0, z_0) — as illustrated in Figure 2.3. This assumption can sometimes capture the broad features that would appear in a more realistic source profile, depending on the orientation of the proton velocity with respect to the fields, but fails when significant deflection occurs from the interaction of off-axis velocity components. In a computational sense, this situation is easy to implement — it is straightforward to define a grid of particles in (x, z) and propagate them with a constant velocity v_0 along y through

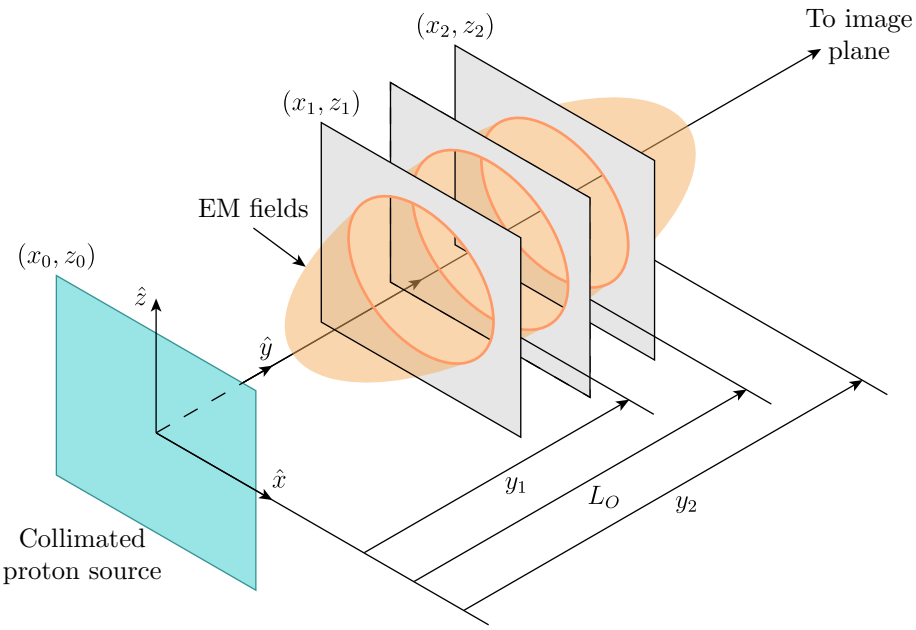

Figure 2.3: The general geometry of probing magnetic fields with a collimated source of protons. The cross section of the EM fields with respect to the extent of the protons remains constant throughout the interaction region.

the system and onto an image. Again, by assuming that the velocity doesn't change much (or at all) within the system itself, the path-integrated fields only require integration along y by transforming the time integration of equation (2.2) using $t = y/v_0$ and $\mathrm{d}t = \mathrm{d}y/v_0$. The changes in velocities from a general magnetic field are thus

$$\Delta v_x(x_0, z_0) = \frac{q}{m_p} \int_{y_1}^{y_2} B_z\left(x_0, y, z_0\right) \mathrm{d}y = \frac{q}{m_p} \int_{y_1}^{y_2} \frac{\partial A_y}{\partial x_0} \mathrm{d}y - \cancel{\frac{q}{m_p} \int_{y_1}^{y_2} \frac{\partial}{\partial y} A_x \mathrm{d}y}, \tag{2.19}$$

$$\Delta v_y(x_0, z_0) = 0, \tag{2.20}$$

$$\Delta v_z(x_0, z_0) = -\frac{q}{m_p} \int_{y_1}^{y_2} B_x\left(x_0, y, z_0\right) \mathrm{d}y = \frac{q}{m_p} \int_{y_1}^{y_2} \frac{\partial A_y}{\partial z_0} \mathrm{d}y - \cancel{\frac{q}{m_p} \int_{y_1}^{y_2} \frac{\partial}{\partial y} A_z \mathrm{d}y}, \tag{2.21}$$

where the $\partial/\partial y$ terms are canceled by assuming that the magnetic field is constrained to the interaction region, so $B = 0$ at y_1 and y_2. From these deflections, assume that the final velocities $v_{I,x} = \Delta v_x$ and $v_{I,z} = \Delta v_z$ are small and apply conservation of energy so $|\underline{v}| = v_0$

to find the post-deflection velocity along y

$$v_y = \sqrt{v_0^2 - \Delta v_x^2 - \Delta v_z^2} \approx v_0, \tag{2.22}$$

which says that we can approximate the velocity v_y after interaction as if there is essentially no change for very small deflections. Propagate the protons with their new transverse velocities to the image plane from the center of the interaction region to find the final proton positions

$$x_I = \frac{v_x}{v_0} L_{OI}, \quad z_I = \frac{v_z}{v_0} L_{OI}. \tag{2.23}$$

In this geometry, the deflection angles are

$$\Delta\alpha_x(x_0, z_0) = \frac{q}{\sqrt{2m_p E_p}} \int_{y_1}^{y_2} B_z\left(x_0, y, z_0\right) \mathrm{d}y = \frac{q}{\sqrt{2m_p E_p}} \int_{y_1}^{y_2} \left(\frac{\partial}{\partial x} A_y - \frac{\partial}{\partial y} A_x\right) \mathrm{d}y,$$

$$\Delta\alpha_y(x_0, z_0) \approx 0,$$

$$\Delta\alpha_z(x_0, z_0) = \frac{q}{\sqrt{2m_p E_p}} \int_{y_1}^{y_2} -B_x\left(x_0, y, z_0\right) \mathrm{d}y = \frac{q}{\sqrt{2m_p E_p}} \int_{y_1}^{y_2} \left(\frac{\partial}{\partial z} A_y - \frac{\partial}{\partial y} A_z\right) \mathrm{d}y.$$

The image can now be determine by applying equation (2.13) to each point on the image. For a simple illustration of this application, assume a one-dimensional image determined by deflections in the x direction to find

$$I = I_0 \left[\frac{\partial x_I}{\partial x_0}\right]^{-1} \tag{2.24}$$

$$= I_0 \left[\frac{\partial}{\partial x_0}\left(x_0 + L_{OI}\Delta\alpha_x\right)\right]^{-1} \tag{2.25}$$

$$= I_0 \left[1 + L_{OI}\frac{\partial}{\partial x_0}\Delta\alpha_x\right]^{-1} \tag{2.26}$$

$$= I_0 \left[1 + \frac{q}{\sqrt{2m_p E_p}} L_{OI} \frac{\partial}{\partial x_0} \int_{y_1}^{y_2} B_z(x_0, y, z_0)\mathrm{d}y\right]^{-1}. \tag{2.27}$$

There are, however, some major shortcomings that come with assuming a collimated source in relation to realistic proton sources available at OMEGA: magnification effects of the imaging process are not included, and, as mentioned before, off-axis velocity components are neglected. A simple, though limited, remedy to the magnification problem can be applied when the length scale of the electromagnetic fields is small relative to its distance from the source. In this case, the deflections can be calculated by integrating along the probe direction while keeping the other position components fixed, and magnification can be added afterward. This quick fix does not truly capture the effects of a diverging source — like the off-axis velocity components — but simplifies the integration and can be a good starting point for understanding what to expect in an image for a given field. Applying a realistic, diverging, proton source profile is covered in the next section.

2.4 Proton Imaging With a Diverging Source

In reality, the available proton sources at HEDP facilities (OMEGA, in particular) are not collimated. Both the D^3He fusion source and TNSA methods create a diverging source of protons which, given the typically high magnification (16–30 times) used in such experiments, can be accurately approximated as a point source of protons. Some effects of using a diverging source are illustrated in Figure 2.4. The basics of this divergence were briefly addressed above in equation (2.16), and that is a good starting point for this section.

2.4.1 Angular Representation

The most mathematically obvious way to include the effects of a diverging proton source is to express the proton trajectories in a spherical coordinate system (r, θ, ϕ) in which the angles are oriented with respect to the imaging axis (i.e. $(r, 0, 0) = y$ from the previous section). In this representation, proton velocities are initialized as (v_0, θ_0, ϕ_0) over a range of θ_0 and ϕ_0. The limits $\theta_{0,max}$ and $\phi_{0,max}$ are the angles subtended by the image, defined by the distance from the proton source to the image L_I and the side length d of the square

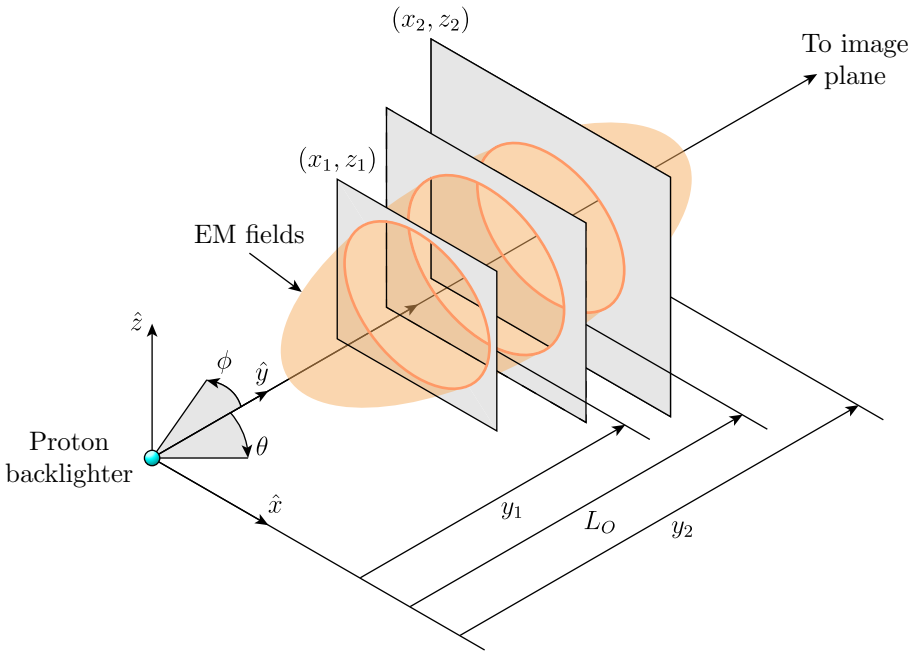

Figure 2.4: Illustration of imaging EM fields with a diverging source of protons. The cross section of the EM fields with respect to the extent of the protons decreases with distance form the source. This shift in magnification (known as perspective) can significantly affect the image. A perspective transform between planes can be used for Cartesian grids of particles to approximate these effects at the expense of some fine features by off-axis velocity components.

detector, and their orientations are shown in Figure 2.4. The limits are (broadly)

$$\theta_{0,max} = \phi_{0,max} = \tan^{-1}\left(\sqrt{2}d/L_I\right) \tag{2.28}$$

so the initial trajectories are defined over the range

$$\theta_0 \in \{-\theta_{0,max}, \theta_{0,max}\}, \quad \phi_0 \in \{-\phi_{0,max}, \phi_{0,max}\}. \tag{2.29}$$

However, because most magnetic field topologies are much more easily defined in Cartesian coordinates, using a fully spherical coordinate system becomes unwieldy. Instead, it is convenient to convert the proton trajectories and positions into Cartesian representation as functions of θ_0 and ϕ_0

$$v_{0,x} = v_0\cos(\theta_0)\sin(\phi_0), \quad v_{0,y} = v_0\cos(\theta_0)\cos(\phi_0), \quad v_{0,z} = v_0\sin(\theta_0). \tag{2.30}$$

Now that I am including the nonzero velocity components along x and z, there are additional deflections to consider. Returning to equation (2.7) and expanding all components, the changes in velocity are

$$\Delta v_x = \frac{q}{m_p}\int_{t_1}^{t_2}\left[v_{0,y}B_z - v_{0,z}B_y\right]\mathrm{d}t, \tag{2.31a}$$

$$\Delta v_y = \frac{q}{m_p}\int_{t_1}^{t_2}\left[v_{0,z}B_x - v_{0,x}B_z\right]\mathrm{d}t, \tag{2.31b}$$

$$\Delta v_z = \frac{q}{m_p}\int_{t_1}^{t_2}\left[v_{0,x}B_y - v_{0,y}B_x\right]\mathrm{d}t. \tag{2.31c}$$

It is again possible to integrate along the system length in y rather than t by substituting

$\mathrm{d}t = \mathrm{d}y/v_{0,y}$ and parametrizing the positions in (y, θ_0, ϕ_0)

$$x = y\tan(\phi_0), \quad z = y\frac{\tan(\theta_0)}{\cos(\phi_0)}, \tag{2.32}$$

Expanding equations (2.31a-2.31c) in terms of θ_0 and ϕ_0 gives

$$\Delta v_x = \frac{q}{m_p}\int_{y_1}^{y_2}\left[B_z(y,\theta_0,\phi_0) - \frac{\tan(\theta_0)}{\cos(\phi_0)}B_y(y,\theta_0,\phi_0)\right]\mathrm{d}y, \tag{2.33a}$$

$$\Delta v_y = \frac{q}{m_p}\int_{y_1}^{y_2}\left[\frac{\tan(\theta_0)}{\cos(\phi_0)}B_x(y,\theta_0,\phi_0) - \tan(\phi_0)B_z(y,\theta_0,\phi_0)\right]\mathrm{d}y, \tag{2.33b}$$

$$\Delta v_z = \frac{q}{m_p}\int_{y_1}^{y_2}\left[\tan(\phi_0)B_y(y,\theta_0,\phi_0) - B_x(y,\theta_0,\phi_0)\right]\mathrm{d}y, \tag{2.33c}$$

which is considerably more complex than for a collimated source, and does not lend itself well to determining a general solution of the deflection angles. To work out any significant meaning from these, it is useful to apply a specific magnetic field topology. Some specific field configurations are explored in sections 2.6.1 and 2.6.2. Next, however, I will describe another method of including some of the effects of a diverging source.

2.4.2 Perspective Representation

Whereas in the previous section proton velocity and position are defined as functions of the spherical angles of the initial trajectories within a pseudo-Cartesian coordinate system, if the positions (x_0, z_0) are instead defined at a specified position y_0 along the imaging axis, the effects of the changing magnification from a diverging source can be applied by the camera perspective transform. The transform simply makes use of the fact that magnification is linear along any imaging axis, easily seen by the relation to y in equation (2.32). Thus, the position of a proton is defined by its initial position and the relative distance along the

imaging axis

$$x = x_0 \frac{y}{y_0}, \quad z = z_0 \frac{y}{y_0}. \tag{2.34}$$

This formulation is particularly useful computationally, because it is natural to initialize a uniform mesh of protons in the xz plane and propagate that mesh through an interaction region to the image plane. Calculating deflections from off-axis velocity components still requires the trajectory angles θ_0 and ϕ_0, which are easily determined from the initialized positions (x_0, y_0, z_0).

Using a grid approach, by visualizing the changing size of the grid of protons as it passes through the interaction region, shown in Figure 2.4, it is straightforward to imagine how extended objects will appear on the image — regions closer to the source will be enlarged, and regions farther away will be diminished. Therefore, the change in magnification across the system must be considered when designing and analyzing proton images. In general, the more two-dimensional the system is — in all aspects — the simpler the analysis becomes. In a typical OMEGA experiment, for which the distance from the source to the center of the interaction region is $L_O = 1$ cm, the system of interest has length $D = 3$ mm, and the distance to the image plane L_{OI} is between 15 and 30 cm, the change in magnification across the interaction region is $\sim 35\%$.

2.5 Proton Imaging in the Caustic Regime

Up to this point I have only discussed imaging when proton deflections are small, but as the magnitude of the deflections increases (and again depending on the field topology) the image analysis becomes more complicated. Return to the functional form of proton images by the Jacobian of final positions with respect to initial positions given by equation (2.13). It is immediately apparent that the expected image intensity profile approaches infinity at any point where the Jacobian becomes zero, and the functional form no longer holds where this occurs. In reality, where the Jacobian becomes zero there is a crossing of final proton

positions with respect to initial trajectories such that the trajectories of protons on one side of the maximum cross to the other side. This region of crossing proton trajectories is a caustic. In the case of a diverging source the location of the maximum becomes the turnover point between deflections due to the fields and the initial ballistic trajectory of the protons.

Mathematically, it is apparent that the final proton positions with respect to initial positions (or trajectories) are nonlinear when caustics are present — there are multiple initial trajectories which produce the same final position — this nonlinearity makes calculating and analyzing proton images more difficult. When creating synthetic images computationally, the typical process would be to initialize a large number of protons, integrate across the interaction region, propagate them to the image plane, and then bin them onto a fixed grid to compute the image. Naturally, this is much more involved than calculating a Jacobian, and more care must be taken with respect to the number of protons and the resolution of the image to create a suitable comparison to experimental images. Additionally, because a binning process is typically necessary to create synthetic images when caustics are present, available field reconstruction techniques are no longer useful (at least around the caustic regions). In fact, the nonlinearities introduced by caustics makes it unlikely that any unique reconstruction could be made, as there is no unique method for *un*binning. However, depending on the field topology and system geometry — if the field is uniform enough and two-dimensional enough — there may be system-dependent methods for reconstruction, or at least methods of inferring field properties, as I will show in section 2.6.2 for the case of the field around a current-carrying wire.

2.6 Comparison of synthetic proton images from collimated and diverging sources

In this section I compare the results of collimated and diverging source analysis for two specific magnetic field topologies — a Gaussian ellipsoid and a current-carrying wire — to

demonstrate the importance of geometric considerations, and to show that simplifications can still result in useable methods of quantitative analysis.

2.6.1 Imaging a Gaussian Ellipsoid of Magnetic Field

Though Kugland et al. (2012) describes the process of finding the deflections of protons for both electric and magnetic field structures, we shall concern ourselves only with the latter case here. Generally, magnetic filaments generated by the Weibel instability[47] are modeled as Gaussian ellipsoids[68], also applied by Kugland et al. (2012), as single-component vector potentials of the form

$$A_z = \frac{B_0 a}{2} \exp\left(-\frac{r^2}{a^2} - \frac{z^2}{b^2}\right), \tag{2.35}$$

in which a and b correspond to the ellipsoid's e-folding distance along its transverse and longitudinal axes and B_0 is the maximum magnetic field strength of the filament (this is generally more easily identified and understood than a maximum vector potential). As mentioned in Section 2.1, using the vector potential greatly simplifies analysis of this field geometry by having only a single component, compared to integrating along the azimuthal magnetic field

$$B_\phi = B_0 \frac{r}{a} \exp\left(-\frac{r^2}{a^2} - \frac{z^2}{b^2}\right). \tag{2.36}$$

As previously discussed Kugland et al. (2012) also only considers the deflections from the proton velocity component parallel to the imaging axis, essentially a collimated source. However, as addressed in Section 2.4, the collimated assumption neglects significant contributions to the image from velocity components other than the imaging axis, which are particularly important when probing perpendicular to the vector potential axis of a filament.

I first address the case of probing parallel to the vector potential axis (in this case y, in Cartesian coordinates) of such a single-component ellipsoid centered on this axis. In this situation it is convenient to utilize the cylindrical symmetry inherent to the fields and define

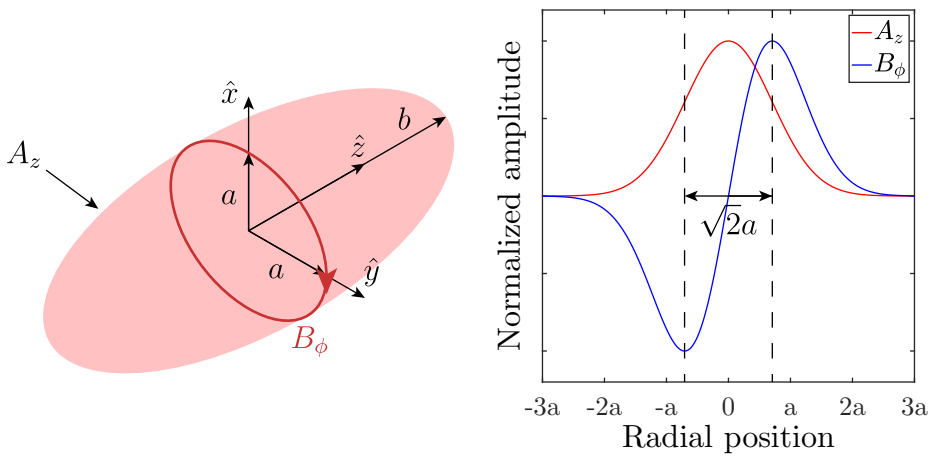

Figure 2.5: Illustration of a Gaussian filament as described by equation (2.35), and the amplitude profiles of the vector potential and azimuthal magnetic field as a function of r at $z = 0$.

velocities in r and z as

$$\underline{v} = v_r \hat{r} + v_z \hat{z}, \tag{2.37}$$

where the probe axis is now z, rather than y. In this formulation the change in velocity is

$$\Delta v_r = \frac{q}{m_p} \int_{z_1}^{z_2} \frac{\partial}{\partial r} A_z \mathrm{d}z = \frac{q}{m_p} \frac{\partial}{\partial r} \int_{z_1}^{z_2} A_z \mathrm{d}z \tag{2.38}$$

$$\Delta v_z = \frac{q}{m_p} \int_{z_1}^{z_2} -\frac{v_{0,r}}{v_{0,z}} \frac{\partial}{\partial r} A_z \mathrm{d}z = -\frac{q}{m_p} \frac{v_{0,r}}{v_{0,z}} \frac{\partial}{\partial r} \int_{z_1}^{z_2} A_z \mathrm{d}z., \tag{2.39}$$

where I have again assumed a constant velocity within the interaction region. From equations (2.38) and (2.39) it is apparent that interaction of the velocity and vector potential in the z direction act to radially deflect the protons, while there is a deflection in the z-direction corresponding to the r component of velocity. The effect of the diverging source thus appears in the r-derivative of v_z and the presence of a v_r component — a collimated source would set these terms to zero, which is the extent of the solution provided by Kugland et al. (2012). For reasonably small angles, the deflection in the r-direction will be much greater than in the z-direction because most of the velocity is directed along z. Because of the disparity in

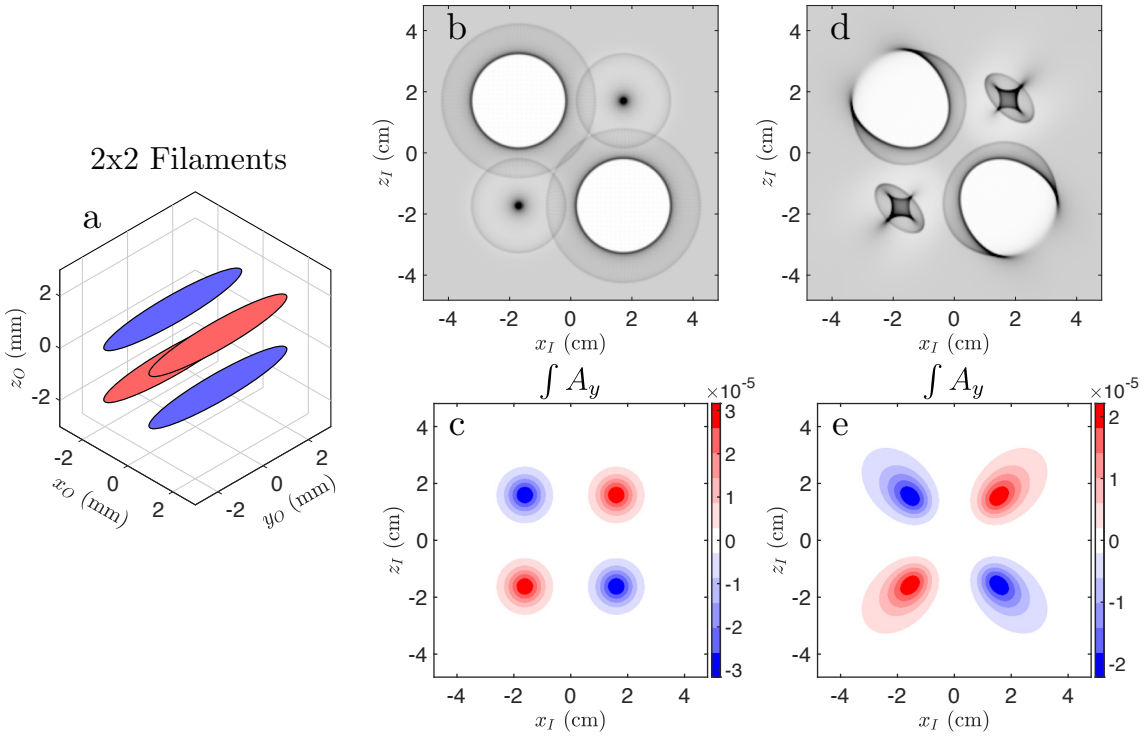

Figure 2.6: Comparing the proton images of a collimated and diverging source for a system of four filaments aligned along the probe axis y. The filaments are modeled as ellipsoidal Gaussian blobs of semiminor axis $a = 400$ μm, semimajor axis $b = 3000$ μm and a maximum magnetic field of 30 T. Following the typical system geometry, $L_O = 1$ cm, and $L_I = 16$ cm. (a) Illustration of the filament system at the object plane, where red and blue indicate positive or negative A_y, respectively. (b,c) The 14.7 MeV proton image and integrated potential at the image for a collimated proton source, (d,e) for a diverging source.

the magnitude of the velocity components, and depending on the length of the ellipsoid, a diverging source may result in only small differences to the proton image.

The radial deflection angle

$$\alpha_r = \frac{q}{\sqrt{2m_p E_p}} \frac{\partial}{\partial r} \int_{z_1}^{z_2} A_z \mathrm{d}z. \tag{2.40}$$

indicates that the magnetic field will act either to focus or defocus the protons, if the deflection angle is either negative or positive, respectively, depending on the relative orientation of v_z and A_z. Figure 2.6 demonstrates these results for a system of four magnetic filaments

of alternating polarity which are illustrated in Figure 2.6a, using Cartesian coordinates. The resulting image and path-integrated vector potential for a collimated source are shown in figures 2.6b and 2.6c, where it is clear that the orientation of the potential either focuses or defocuses the protons. When including the effect of perspective analytically, shown in figures 2.6d and 2.6e, the image features are not as uniform, and track with the changing magnification. This shows very clearly that the effects of a diverging source are significant, particularly the effect of perspective on the integration.

Now consider the case of probing a magnetic filament perpendicular to the vector potential axis of the filament. To do so, it is easiest to change back to Cartesian coordinates, with y the imaging axis and z the filament axis, so again the only component of the vector potential is A_z. The velocity components change as

$$\Delta v_x = \frac{q}{m_p} \int_{t_1}^{t_2} v_z \frac{\partial}{\partial x} A_z \mathrm{d}t \tag{2.41a}$$

$$\Delta v_y = \frac{q}{m_p} \int_{t_1}^{t_2} v_z \frac{\partial}{\partial y} A_z \mathrm{d}t \tag{2.41b}$$

$$\Delta v_z = \frac{q}{m_p} \int_{t_1}^{t_2} - \left(v_x \frac{\partial}{\partial x} + v_y \frac{\partial}{\partial y} \right) A_z \mathrm{d}t, \tag{2.41c}$$

from which an important realization should be made: the deflections on the image plane are caused by the velocity component moving in the direction of the vector potential, which, in this case, is orthogonal to the probe axis. Indeed, every deflection has a component that depends on $v_z A_z$, and, importantly for Weibel instability experiments, the deflection in x is *solely* dependent on the z component of velocity. It is therefore unwise to assume a collimated source when probing perpendicular to the vector potential, as it would not produce any deflection. The treatment of this problem provided by Kugland et al. (2012) is therefore insufficient for explaining structures observed in experimental proton images of magnetic filaments. In fact, Δv_x closely resembles the radial deflection angle when probing parallel to

the long axis of the filament, so the effect will be to either focus or defocus the protons in x depending on the magnitude and sense of both v_z and A_z. For a positive A_z, the field will defocus the protons for $z > 0$ and focus them for $z < 0$, which leads to the characteristic fence-like pattern in experimental and synthetic proton images of forests of these filaments. These results are demonstrated in Figure 2.7, where I calculate the proton images for a system of four filaments aligned perpendicular to the probe axis (aligned in z). Unsurprisingly, the proton image and change in velocity v_x from the path-integrated vector potential for a collimated source (2.7b and 2.7c) are zero. When including the effect of a diverging source (2.7d and 2.7e), deflections in x and z now occur, and the fence-like structures seen in experiments (i.e. Huntington et al. (2015)) are recovered. The deflections in this case require off-axis velocity components, which are only possible when using a diverging source.

2.6.2 Imaging the Field Around a Current-Carrying Wire

The magnetic field generated on the outside of a cylindrically symmetric, semi-infinite, current-carrying wire is proportional to the current in the wire and inversely proportional to distance from the wire as

$$\underline{B} = \frac{\mu_0 I}{2\pi r}\hat{\theta}, \quad r \geq R, \tag{2.42}$$

where μ_0 is the vacuum permeability, I is the current in the wire, R is the radius of the wire, and r is the radial distance from the wire axis. For simplicity, this can also be represented in terms of the maximum field B_0 at the surface of the wire (where $r = R$)

$$\underline{B} = \left(\frac{\mu_0 I}{2\pi R}\right)\frac{R}{r}\hat{\theta} = B_0\frac{R}{r}\hat{\theta}, \quad r \geq R. \tag{2.43}$$

Immediately apparent is the cylindrical symmetry, which, as with the magnetic filament, simplifies the problem to a nearly one-dimensional form.

In this section I will derive analytically features of the expected proton image due to the field around a current-carrying wire. Because of the available symmetry I assume that the

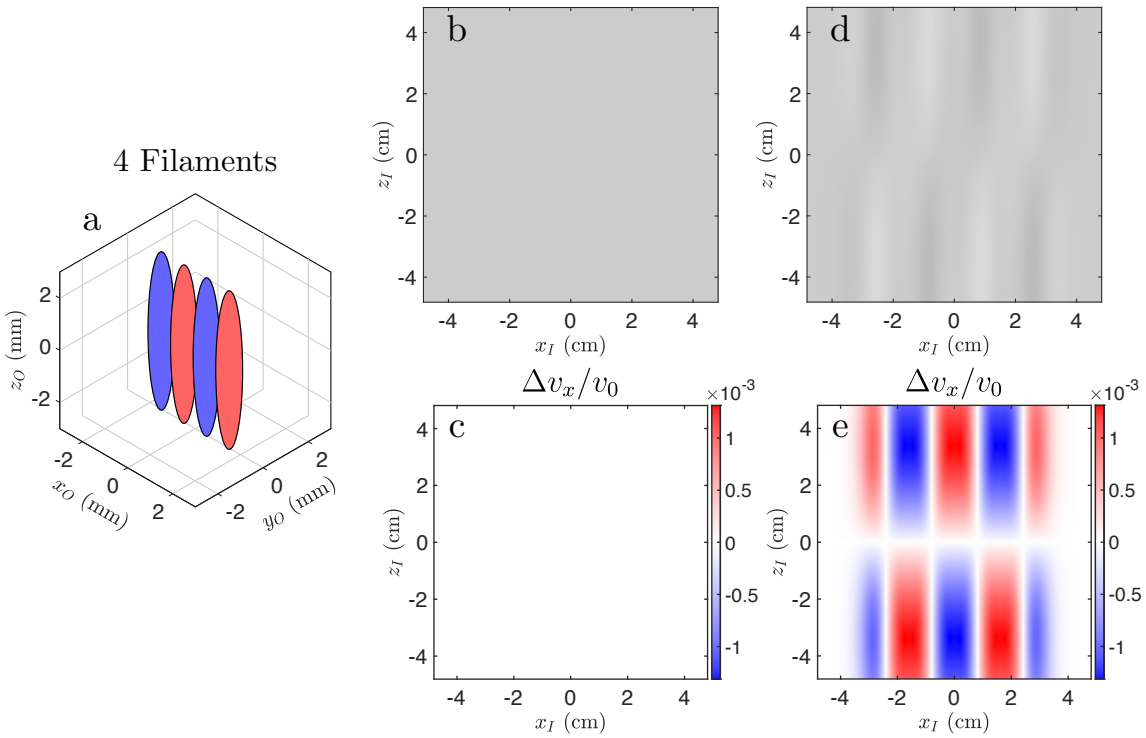

Figure 2.7: Comparing the proton images of a collimated and diverging source for a system of four filaments aligned perpendicular to the probe axis y. The filaments are modeled as ellipsoidal Gaussian blobs of semiminor axis $a = 400$ μm, semimajor axis $b = 3000$ μm and a maximum magnetic field of 15 T. Following the typical system geometry, $L_O = 1$ cm, and $L_I = 16$ cm. (a) Illustration of the filament system at the object plane, where red and blue indicate positive or negative A_z, respectively. (b) The 14.7 MeV proton image and the relative change in velocity v_x due to the path-integrated vector potential for a collimated proton source, (d,e) for a diverging source.

proton source is aligned along the axis of the wire ($\hat{z}$). Similar to the previous section dealing with the magnetic field of an ellipsoid filament, deflections to proton trajectories based on motion parallel to $\hat{z}$ — the direction of the current in the wire — will be solely in r. The effect of the deflections will be either to focus the protons to a point or to defocus them, depending on whether the protons probe parallel or antiparallel, respectively. The radial deflection is given by

$$\Delta v_r = \frac{q}{m_p} v_{0,z} B_0 \int_{t_1}^{t_2} \frac{R}{r} \mathrm{d}t, \tag{2.44}$$

By again assuming constant proton velocity within the interaction region, the time integral

of equation (2.44) can be converted to an integral in z using $\mathrm{d}z = v_{0,z}\mathrm{d}t$, which removes the velocity dependence in front and gives

$$\Delta v_r = \frac{q}{m_p} B_0 \int_{z_1}^{z_2} \frac{R}{r} \mathrm{d}z. \tag{2.45}$$

This integral is trivial when assuming a constant radial distance from the wire, however, when including the divergence of a point source, the initial velocities are

$$v_{0,z} = v_0 \cos(\theta_0), \quad v_{0,r} = v_0 \sin(\theta_0), \tag{2.46}$$

where θ_0 is the initial angle of a proton's trajectory, and the radius changes as

$$r(z) = z \sin\theta_0. \tag{2.47}$$

Substituting this back into equation (2.45),

$$\Delta v_r = \frac{q}{m_p} \frac{B_0 R}{\sin(\theta_0)} \int_{z_1}^{z_2} \frac{\mathrm{d}z}{z} = \frac{q}{m_p} \frac{B_0 R}{\sin(\theta_0)} \ln\left(\frac{z_2}{z_1}\right). \tag{2.48}$$

It is again easy to find the angle of deflection as a function of the initial proton angle θ_0

$$\alpha = \tan^{-1}\left(\frac{v_0 \sin(\theta_0) + \Delta v_r}{v_0}\right) - \theta_0 \approx \frac{\Delta v_r}{v_0}, \tag{2.49}$$

$$= \frac{q}{\sqrt{2 m_p E_p}} \frac{B_0 R}{v_0 \sin(\theta)} (\ln \frac{z_2}{z_1}) \tag{2.50}$$

$$= \frac{q}{\sqrt{2 m_p E_p}} \frac{B_0 R}{v_0 \theta_0} (\ln \frac{z_2}{z_1}), \tag{2.51}$$

where θ_0 is assumed to be small.

After acquiring some deflection while passing through the interaction region, the radial

positions of the protons at the image plane are

$$r_I = z_2 \tan(\theta_0) + (L_I - z_2) \tan(\theta_0 + \alpha) \approx L_I \theta_0 + L_{OI} \alpha(\theta_0), \tag{2.52}$$

where all angles are assumed to be small. The radial location of maximum proton fluence on the image occurs where the derivative with respect to θ_0, so where

$$\frac{\partial r_I}{\partial \theta_0} = L_I + L_{OI} \frac{\partial}{\partial \theta_0} \alpha = 0. \tag{2.53}$$

Substituting in equation (2.51) for $\alpha(\theta_0)$,

$$\frac{\partial \alpha}{\partial \theta_0} = -\frac{qB_0R}{m_p v_0 \theta_0^2} \ln(\frac{z_2}{z_1}). \tag{2.54}$$

The location of the proton intensity maximum thus occurs for the initial angle

$$\theta_{0,\max} = \left[\frac{L_{OI}}{L_I} \frac{qB_0R}{\sqrt{2m_pE_p}} \ln(\frac{z_2}{z_1}) \right]^{1/2}, \tag{2.55}$$

which corresponds to a radius on the image

$$r_{I,\max} = L_I \theta_{0,\max} + L_{OI} \alpha(\theta_{0,\max}). \tag{2.56}$$

By substituting the value of the deflection angle

$$\alpha(\theta_{0,\max}) = \left[\frac{L_I}{L_O I} \frac{qB_0R}{\sqrt{2m_pE_p}} \ln(\frac{z_2}{z_1}) \right]^{1/2}, \tag{2.57}$$

the radius of the intensity maximum on the image is

$$r_{I,\max} = 2 \left[L_I L_{OI} \frac{qB_0R}{\sqrt{2m_pE_p}} \ln(\frac{z_2}{z_1}) \right]^{1/2}. \tag{2.58}$$

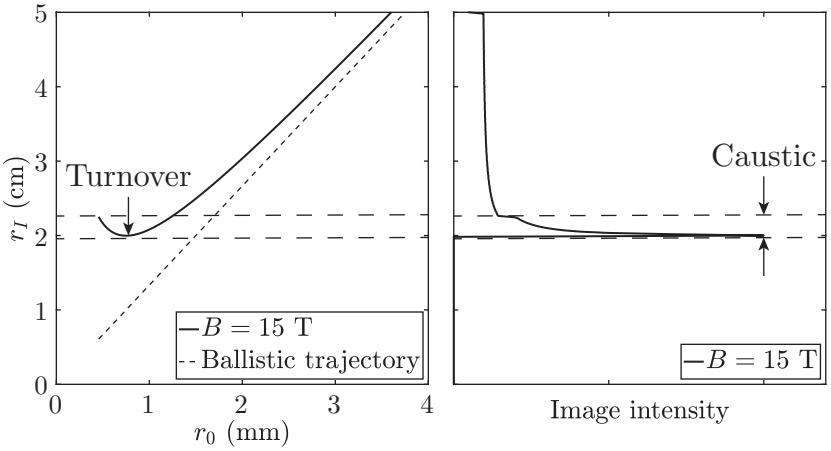

Figure 2.8: Left: plotting the radial position of a proton at the image plane r_I as a function of radial position in the interaction region r_0, for a point source of protons interacting with the field around a current-carrying wire given the specified experimental geometry for a maximum field of 15 T at the surface of the wire. Right: the resulting caustic image intensity profile, where the intensity maximum occurs at the turnover point between deflected and ballistic trajectories.

Equation (2.58) unfortunately depends on many variables, concerning the geometry of the system, the magnetic field, and proton energy, which make it potentially unwieldy. However, by substituting in some reasonable values — particularly those corresponding to the experiments discussed in Chapter 4 — a much more usable expression is acquired. Using the experimental values $L_O = 1$ cm, $L_I = 16$ cm, $L_{OI} = 15$ cm, $R = 380$ μm, $z_1 = 0.8$ cm, $z_2 = 1.2$ cm, the expression becomes

$$r_{I,\max} = 3.2 \left[\frac{B_0}{10\text{ T}}\right]^{1/2} \left[\frac{1\text{ MeV}}{E_p}\right]^{1/4} \text{cm}. \tag{2.59}$$

This representation is further adapted the analysis of experimental proton images in Chapter 4.

2.7 Path-Integrated Field Reconstruction

Because of the inherent difficulty in proton image analysis, work has been done to create a general framework for analysis by way of reconstructing path-integrated magnetic fields.

This possibility was first proposed by Kugland et al. (2012), for some limited cases, and further expanded to become more general by Graziani et al. (2017) and Bott et al. (2017). These methods have been applied to the turbulent dynamo experiments by Tzeferacos et al. (2018).

Field reconstruction is an inverse problem — it seeks to determine a path-integrated field structure from the resulting image. To do this, certain assumptions must be made about the system and the imaging process. The first assumption is that the total image intensity (number of protons on the image) is conserved between the initial and final states. Images must also lie solely in the linear regime to ensure that there is a one-to-one mapping of final proton positions to initial positions. The introduction of caustic nonlinearities disallows unique solutions of the path-integrated field, because it is not generally possible to separate the overlapping intensities. As discussed in Section 2.2, proton images in the linear regime can be determined by the application of an operator on the initial image map, written as

$$I - FI_0 = I_0, \tag{2.60}$$

where F is operating on the initial (uniform) intensity map I_0, and the total proton intensity is conserved. F encodes the information of proton deflections to the image. This is demonstrated by the image calculation from equation (2.24) of section 2.3, where the two-dimensional image function in the small-intensity regime can be approximated as

$$I = \frac{I_0}{|D(x_0, z_0)|} = I_0 \left[1 + L_{OI}\left(\frac{\partial \alpha_x}{\partial x_0} + \frac{\partial \alpha_z}{\partial z_0}\right)\right]^{-1} \approx I_0 \left[1 - L_{OI}\left(\frac{\partial \alpha_x}{\partial x_0} + \frac{\partial \alpha_z}{\partial z_0}\right)\right]. \tag{2.61}$$

In this case, F is

$$F = -L_{OI}\left(\frac{\partial}{\partial x_0}\Delta\alpha_x + \frac{\partial}{\partial z_0}\Delta\alpha_z\right) = \frac{qL_{OI}}{\sqrt{2m_pE_p}}\left(\frac{\partial^2}{\partial^2 x_0} + \frac{\partial^2}{\partial^2 z_0}\right)\int_{y_1}^{y_2} A_y \mathrm{d}y, \tag{2.62}$$

which can be recognized as a Poisson equation

$$F = -\nabla^2 \Phi, \tag{2.63}$$

where Φ is the path-integrated vector potential. Kugland et al. (2012) provide a general, simplified solution for finding Λ. Graziani et al. (2017) expands upon this formalism by including the effect of the deflected proton positions by the path-integrated potential in their field-reconstruction equation

$$I(\underline{x_0} + \nabla\Phi(\underline{x_0})) = \nabla^2\Phi(\underline{x_0}). \tag{2.64}$$

From this, they are then able to rewrite the equation as a two-dimensional, steady-state diffusion equation

$$\nabla \cdot \left[e^{I(\underline{x_0})}\nabla\Phi(\underline{x_0})\right] = I(\underline{x_0})e^{I(\underline{x_0})}, \tag{2.65}$$

which can be solved numerically to determine a path-integrated field.

The reconstructed path-integrated field can be a useful quantity, but the quality depends on the method used — particularly, the complexity of the imaging process accounted for. One aspect not explicitly addressed in the reconstruction equations above is the addition of magnification changes from a diverging source, which Section 2.4 showed can be significant. The simple solution of Kugland et al. (2012) assumes only a collimated source, but it would be feasible to accommodate this profile in the method of Graziani et al. (2017), and this effect can also be included in the more complex, generalized methods presented in Bott et al. (2017). However, field reconstruction will not be emphasized in the following chapters. When dealing with proton images of a statistical system of fields, as in the case of the filament analysis in Chapter 3, a two-dimensional inference of the fields gets us no closer to understanding the underlying correlations between the filaments and the image features, so other methods must be employed. Then, when imaging the field around a current-carrying

wire in Chapter 4, the images are inherently caustic, as demonstrated in Section 2.6.2, so reconstruction cannot be reliably employed.

2.8 Conclusion

In this chapter I have worked through some of the important aspects of proton image analysis. Proton imaging provides unique measurement challenges because it relies on deflections — the direction and degree to which protons are deflected, along with where the protons end up on the image depend on the field strength, field topology, and system geometry. Changes to field topology and probe orientation produce fundamentally different images, so there is no easy way to generalize a solution, particularly if caustics are involved.

There is, however, a general procedure which can be followed. First, consider the geometry: the magnetic field orientation with respect to the proton trajectories, the system size, the expected field strength, and the path length from the object region to the image plane. Using this information calculate a synthetic (computational or analytic) proton image. If the system exhibits a useful symmetry, reduce the dimensionality of the deflections as possible. Consider the components of the velocity relative to the magnetic field and add the divergence of the proton source, if applicable. From the synthetic image profile, determine whether the image exhibits caustics and where, as this will limit what analysis tools are available. If deflections are small and the entire image exists in the linear (non-caustic) regime, then it is possible to apply techniques which reconstruct the path-integrated field based on optimizing the cost (imaging) function.

If the image exhibits caustics, then there is not necessarily a unique function which can be used to invert the image and reconstruct the field (although if the field topology is well-known it may be possible to construct a system-specific methodology to do so). In such a case, inferring quantitative information from the proton image requires careful consideration of the system topology. In the case of caustics generated by a known field, the general approach is to determine — analytically — what the image should look like given the system

parameters and how it changes based on proton energy and field amplitude. For example, as explored in section 2.6.2, proton images probing antiparallel to the direction of current in a wire are inherently caustic by nature of the $1/r$ magnetic field topology. Luckily, despite being caustic, field information can be inferred from such a proton image. As evidenced by equation (2.59), the experimental location of the proton image maximum allows inference of field strength, provided the system geometry and proton energy are known.

In Chapter 3 I apply the above knowledge to images produced by small-scale, statistical magnetic field structures. Then, in Chapter 4 I deal with images of strong magnetic fields around a current-carrying wire. In both of these cases the electric fields effects are small compared to the magnetic fields, and the most useful analytic tool is an assumption for the underlying magnetic field geometries.

CHAPTER 3

Characterizing Filamentary Magnetic Structures in Counter-Streaming Plasmas by Fourier Analysis of Proton Images

This chapter is adapted from Levesque et al. (2019).

Proton imaging is a powerful tool for probing electromagnetic fields in a plasma, providing a path-integrated map of the field topology. However, in cases where the field structure is highly inhomogeneous, inferring spatial properties of the underlying field from proton images can be difficult. This problem is exemplified by recent experiments which used proton imaging to probe the filamentary magnetic field structures produced by the Weibel instability in collisionless counter-streaming plasmas. In this chapter, we perform analytical and numerical analysis of proton images of systems containing many magnetic filaments. We find that, in general, the features observed on proton images do not directly correspond to the spacing between magnetic filaments (the magnetic wavelength) as has previously been assumed, and that they instead correspond to the filament size. We demonstrate this result by Fourier analysis of synthetic proton images for many randomized configurations of magnetic filaments. Our results help guide the interpretation of experimental proton images of filamentary magnetic structures in plasmas.

3.1 Introduction

Proton imaging is a powerful technique for probing electromagnetic fields in high-energy-density plasma experiments with high-energy (> MeV) protons.[71,66,65,72] Deflections from initial proton trajectories by interaction with electromagnetic fields encode information about the path-integrated field structure onto a detector in the form of spatial variations of the observed proton flux. Proton imaging has been used successfully in experiments studying laser-produced plasma bubbles[71,65,72], magnetic reconnection[72], turbulent dynamo amplification of magnetic fields[34], and the Weibel instability[24,73,18,74,20,21,75], among others. The detailed analysis by Kugland et al. (2012) provides a basis for determining proton image structures from electric and magnetic fields, but inferring quantitative field information from an image is difficult due to its path-integrated nature. Recently, methods have been developed which can infer path-integrated field topology from proton images by solving the inverse problem.[69,70] However, inferring internal structure or spatial scales of magnetic fields which are neither smooth nor homogeneous requires further geometrical assumptions about the system.

An important example of inhomogeneous electromagnetic fields produced in plasmas is the filamentary magnetic field structures associated with the Weibel or current-filamentation instability.[47,76] The Weibel instability is associated with anisotropy of the plasma velocity distribution and is known to lead to the formation of current filaments in counterstreaming, collisionless plasmas, converting kinetic energy into magnetic energy.[47] The Weibel instability, at its most basic, can occur in anisotropic plasma systems when there is a significant difference in velocity across the plasma, or in the interaction of a fast beam with an ambient plasma. A perturbation of the electromagnetic fields transverse to the direction of the velocity anisotropy drives small-scale changes in the current density which, in turn, generate small-scale magnetic fields azimuthal to the perturbed current densities. Defining the beam to be in the z direction, a transverse (r direction) perturbation to the z component of the electric field generates an azimuthal magnetic field. These driven changes in the

current density are in the same direction as the velocity anisotropy, which can be better envisioned by considering the interpenetration of two collisionless electron beams, whose counter-propagating currents drive electromagnetic fields. Under the right conditions, the electromagnetic perturbation is unstable and becomes a purely growing wave, which acts to increase the magnetic fields.

Following the assumptions of Schlickeiser and Shukla (2003), in the interaction of a cold electron beam of number density n_b and initial velocity u with an ambient plasma with a Maxwellian distribution of electron density n_e and ion density n_i, the linear dispersion relation for a plasma experiencing an electromagnetic perturbation is

$$\omega^2 = -\omega_{be}^2 \left(\frac{k^2 u^2}{k^2 c^2 + \omega_{be}^2} - \frac{k^2 v_{th,e}^2 v_{th,i}^2}{\omega_{pe}^2 v_{th,i}^2 + \omega_{pi}^2 v_{th,e}^2} \right), \tag{3.1}$$

where ω is the angular frequency of the time-varying component of the perturbation, ω_{be} is the electron plasma wave frequency for the beam species, k is the wavenumber associated with the transverse perturbation, and the v_{th} terms are the thermal velocities of the electrons and ions in the hot plasma. After some simplification, the conditions for a purely growing mode ($\omega^2 < 0$) are

$$k^2 < \left[\frac{(Z+1)\, u^2}{v_{th,e}^2} - \frac{n_b}{n_e} \right] \left(\frac{\omega_{pe}^2}{c^2} \right), \tag{3.2}$$

$$u^2 > \frac{n_b}{n_e} \frac{v_{th,e}^2}{(Z+1)}, \tag{3.3}$$

where Z is the average ionization of the plasma. In the case when the beam velocity $u \gg v_{th}$, the growth rate of the perturbation is

$$\Gamma = \frac{u \omega_{be} k}{\sqrt{k^2 c^2 + \omega_{be}^2}}, \tag{3.4}$$

as first reported by Weibel (1959). This instability will grow, converting kinetic energy to electromagnetic energy, until the magnetic field reaches a saturated value.[77,48]

This instability is expected to be common in astrophysical plasmas, potentially mediating the amplification of magnetic fields, the formation of collisionless shocks, and the acceleration of particles in energetic and weakly magnetized environments such as gamma ray bursts and young supernova remnant shocks.[77] Furthermore, magnetic fields observed throughout the intergalactic medium may have been seeded by this instability during the early universe.[48,78] In recent years, there has been a significant effort to study the Weibel instability and collisionless shocks mediated by it in laboratory laser-driven plasmas.[18,20,79] Experiments at OMEGA[24,73,74,20,21] and the NIF[75] have explored this instability, successfully observing filamentary magnetic fields.

The Weibel instability is an interesting system of study for proton imaging capabilities because the magnetic fields it generates are highly structured, consisting of many small-scale filaments. The proton images produced when probing these systems perpendicular to the interpenetration axis show filamentary striations in the proton fluence.[74,20,25] However, inferring internal field parameters from these images has proven to be difficult, because the protons experience deflections from many filaments along any path. Previous papers[18,25,20] infer the characteristic spatial mode of the magnetic field as the average distance between successive peaks of proton fluence on a proton image, but it is unclear if this is an accurate or robust method for characterizing the structure of these fields. Levy et al. (2015) explore this issue by creating and analyzing synthetic proton images of randomized distributions of Gaussian magnetic filaments. The synthetic proton images qualitatively recreate filamentary structures seen in experiment, however, no quantitative relation is determined between the spatial modes of synthetic proton images and those of the corresponding magnetic field.

In this analysis we develop a simple analytical model of proton images in the linear deflection regime[54,70] suitable for use on small-scale field structures, and demonstrate that spatial information of Weibel-like magnetic fields may be inferred from Fourier analysis of proton image features. This chapter is organized as follows. Section 3.2 establishes the methodology which we use to produce synthetic proton images in the linear deflection regime.

In Section 3.3 we discuss what we call the forest effect (a term coined by Dmitri Ryutov), which is associated with probing a large number of filamentary structures, and address the limitations associated with inferring the spacing between filaments by counting the number of peaks in the proton images. In Section 3.4 we show that the size of filamentary magnetic fields can be inferred from Fourier analysis of the proton images, illustrate that this method is robust for different field configurations, and address the broader applicability of the method we develop. Section 3.5 concludes the chapter.

3.2 Proton Imaging of Magnetic Filaments

To explore the relationship between filamentary field structures and the associated proton images we develop a simple analytical and numerical model. The system geometry consists of three components, the proton source, the interaction region, and the image plane, as illustrated in Figure 3.1. Following the work of Kugland et al. (2012) and Levy et al. (2015), the filaments are assumed to be Gaussian ellipsoids of vector potential

$$\begin{aligned} A_z\left(x', y', z'\right) &= A_0 \exp\left(-\frac{x'^2}{a^2} - \frac{y'^2}{a^2} - \frac{z'^2}{b^2}\right), \\ A_x &= A_y = 0, \end{aligned} \tag{3.5}$$

where A_0 is the maximum vector potential of the filament, a is the characteristic filament size in the radial plane, and b the characteristic length along the collision axis. The primed coordinates are defined with respect to the center of the filament (x_c, y_c, z_c),

$$x' = x - x_c, \quad y' = y - y_c, \quad z' = z - z_c. \tag{3.6}$$

As in Levy et al. (2015), all filaments are constrained to lie within the cylindrical volume of the interaction region. For further simplification, all filaments are oriented along $\hat{z}$ and considered infinite in length (i.e. $b \to \infty$) to remove variation in z.

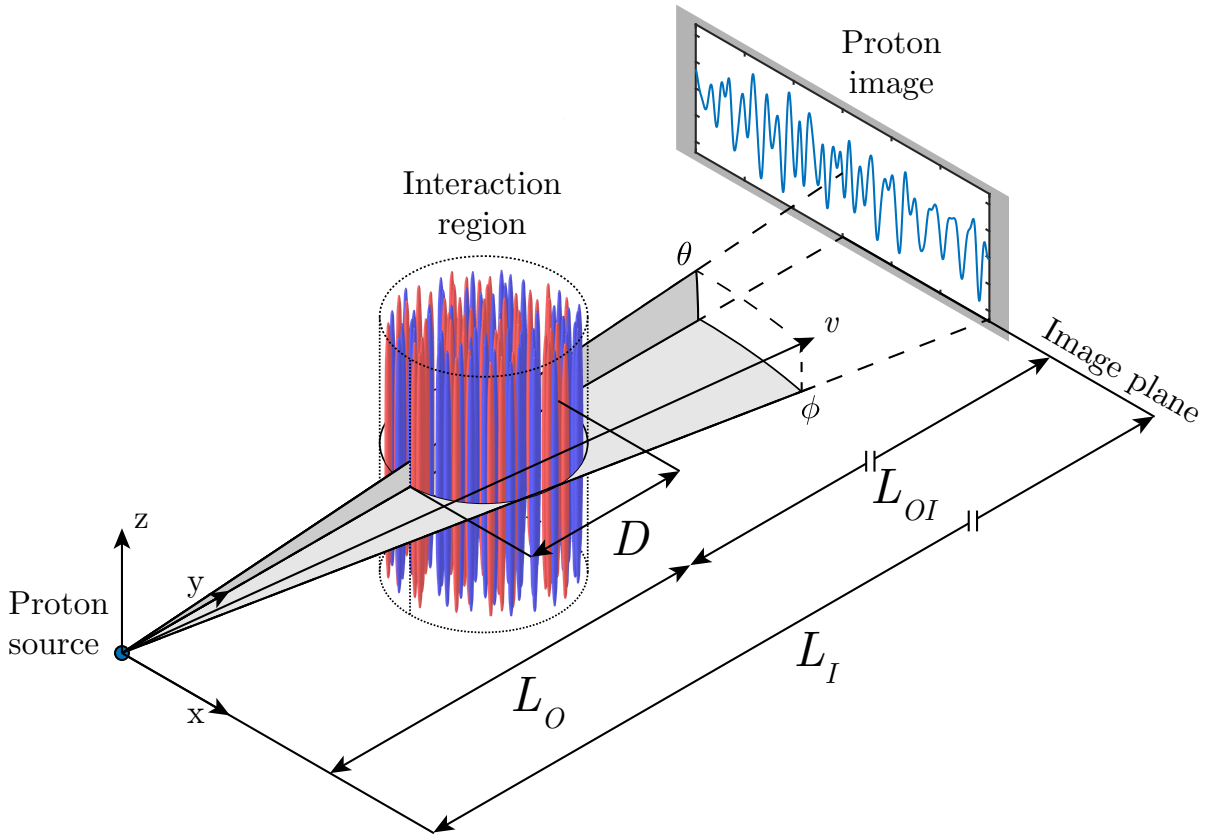

Figure 3.1: Illustration of the system geometry (not to scale). The interaction region is cylindrical with radius in the xy plane and extends infinitely in the z direction. The filaments are contained within the prescribed interaction region, depicted by colored contours of vector potential A_z for a representative system of filaments, where each filament is described as in equation (3.5), and illustrated by Figure 2.5. Protons stream from the origin with initial velocity v through the interaction region to the image plane.

We use the field definition of equation (3.5) to develop a simple analytic model for proton images of filamentary magnetic fields in the linear proton deflection regime. The linear deflection regime, as defined by Kugland et al. (2012), is when proton deflections are small relative to the scale length of electromagnetic fields. The linearity parameter (adapted for our notation) is defined as

$$\mu \equiv L_O \alpha / L_{EM}, \tag{3.7}$$

where L_O is the y-distance from the proton source to the center of the interaction region, α is the proton deflection angle, and L_{EM} is the scale length of the electromagnetic fields. The linear regime is defined as when $\mu \ll 1$. In the case of filamentary magnetic fields, $L_{EM} = a$, and the linear regime applies when $\alpha \ll a/L_O$. In the linear regime, deflections from a proton's initial, unperturbed trajectory are negligible across a single filament, so the total deflection can be calculated from the path-integrated vector potential along the unperturbed trajectory.

We consider a point-like, divergent proton source with initial proton velocities

$$v_x = v \cos\theta \sin\phi, \quad v_y = v \cos\theta \cos\phi, \quad v_z = v \sin\theta, \tag{3.8}$$

where v is the initial speed and the angles θ and ϕ are angles from the y axis in the yz and xy plane as depicted in Figure 1. The angle ϕ provides for magnification effects in the x direction. Because of the uniformity and infinite extent of the filaments along z, we consider only proton deflections in the x direction, producing 1D proton images at a nonzero angle θ as depicted in Figure 3.1. Furthermore, we consider the small deflection regime, where the interaction region diameter D is much smaller than the distance L_O between the proton source and the interaction region, which is typically true in experiment. In this paraxial limit, proton trajectories are considered constant across the interaction region. The angular

deflections in x are calculated as

$$\alpha_x = \frac{e}{c\sqrt{2m_pW}} \sin\theta \frac{\partial}{\partial x} \int_0^{L_I} A_z \mathrm{d}y, \tag{3.9}$$

where e is the electric charge, m_p is the proton mass, c is the speed of light, and W is the energy of the probe protons. We note that in the limiting case of $\theta = 0$, equation (3.9) predicts no deflection in x. In reality, small deflections in x can still arise from higher-order terms as shown in Kugland et al. (2012). However, in typical experiments the proton source is divergent, providing the necessary v_z, and equation (3.9) can thus be used to describe the dominant deflections.

The entire length D across the interaction region is contained within the integration bounds of equation (3.9), and we assume a single filament $a \ll D$, so we can approximate the integral as

$$\int_0^{L_I} A_z \mathrm{d}y \approx \int_{-\infty}^{\infty} A_z \mathrm{d}y = \sqrt{\pi a^2} A_0 \exp\left(-\frac{x^2}{a^2}\right). \tag{3.10}$$

Substituting into equation (3.9), the deflection by a single filament is

$$\alpha_x(x) = \frac{e}{c\sqrt{2m_pW}} A_0 \sin\theta \left(-\frac{2\sqrt{\pi}x}{a}\right) \exp\left(-\frac{x^2}{a^2}\right). \tag{3.11}$$

Assuming the deflection occurs at the center of the interaction region, protons arrive at the image plane with deflected positions

$$x_I(x) = \frac{L_{OI}}{L_O} \left[x + L_O \alpha_x(x)\right], \tag{3.12}$$

where x is the position of a proton along an unperturbed trajectory defined at $y = L_O$. From Kugland et al. (2012), in the linear deflection regime the proton fluence map I at the image can be calculated as

$$I = I_0 \left[1 - L_O \frac{\partial}{\partial x} \alpha_x\right], \tag{3.13}$$

where I_0 is the initial, unperturbed proton fluence profile. The proton image from deflections by a Gaussian filament is thus

$$I(x) = I_0 - L_O \frac{e}{c} \sqrt{\frac{\pi a^2}{2 m_p W}} A_0 \sin\theta \frac{\partial^2}{\partial x^2} \exp\left(-\frac{x^2}{a^2}\right), \tag{3.14}$$

whose profile is primarily proportional to the second derivative of the path-integrated vector potential A_z — the second derivative of a Gaussian in x. By normalizing about the mean image intensity, the influence of any Gaussian filament on the image can be generalized to

$$\delta I(x, x_c) = \left(-\frac{2}{a^2} + \frac{4(x - x_c)^2}{a^4}\right) e^{-(x-x_c)^2/a^2}. \tag{3.15}$$

In the linear deflection regime the image contribution from each filament is effectively independent from one another. Thus, the image of a system of multiple filaments is the summation of contributions from all filaments in the system

$$I(x) = I_0(x) + \sum_n^N \delta I(x, x_{cn}) = I_0(x) + \sum_n^N \delta I_n(x), \tag{3.16}$$

where the subscript cn refers to the center of a filament n.

3.3 The Forest Effect

Previous works have assumed that the spacing between filaments in the interaction region can be directly inferred from the average spacing between successive peaks in fluence on a proton image, adjusted for magnification.[18,20] This may seem like a simple and attractive solution, but because of the complexity of the underlying field structures it is not clear whether this method accurately infers the spacing between filaments in the plasma as intended.

Consider the problem more simply: envision a forest of trees whose centroids are described by a spatial Poisson point process. When viewed from above (Figure 3.2a) the spatial modes of this system may be characterized by the average distance between centroids in the xy

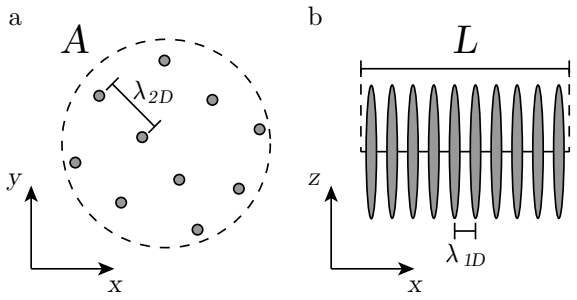

Figure 3.2: Spatial scales for (a) top-down view showing an areal distribution of vector potential filaments, and (b) a side-on view showing a linear distribution of the same number of filaments.

plane, defined as

$$\lambda_{2D} = \sqrt{\frac{A}{N}}, \tag{3.17}$$

where A is the 2D area in which N trees exist. When looking instead at this forest from the ground along the y direction (Figure 3.2b), position information collapses along that axis. Ignoring magnification effects, the position of the trees can now only be discerned in one dimension — along x. The spatial mode in this case corresponds to the average x distance between the trees

$$\lambda_{1D} = L/N, \tag{3.18}$$

where L is the length across the forest. Now extend this line of thought to a distribution (a *forest*) of identical magnetic filaments, or more specifically, the proton image of such a forest of filaments. This simple example illustrates that, naively, one would expect that when the number of filaments (trees) is very large ($N \gg 1$), the wavelength of the filamentary magnetic structures (the spacing between trees) that is inferred from the proton image is significantly smaller, by a factor of $\sqrt{N}$, than the actual filament wavelength.

To explore whether the method of counting peaks on proton images accurately infers the spacing between filaments, we generate randomized distributions of filaments from which we create synthetic 1D proton images. The synthetic system geometry corresponds to the OMEGA experiments[18,20,68]; the interaction region is an infinite cylinder of diameter $D = 3$

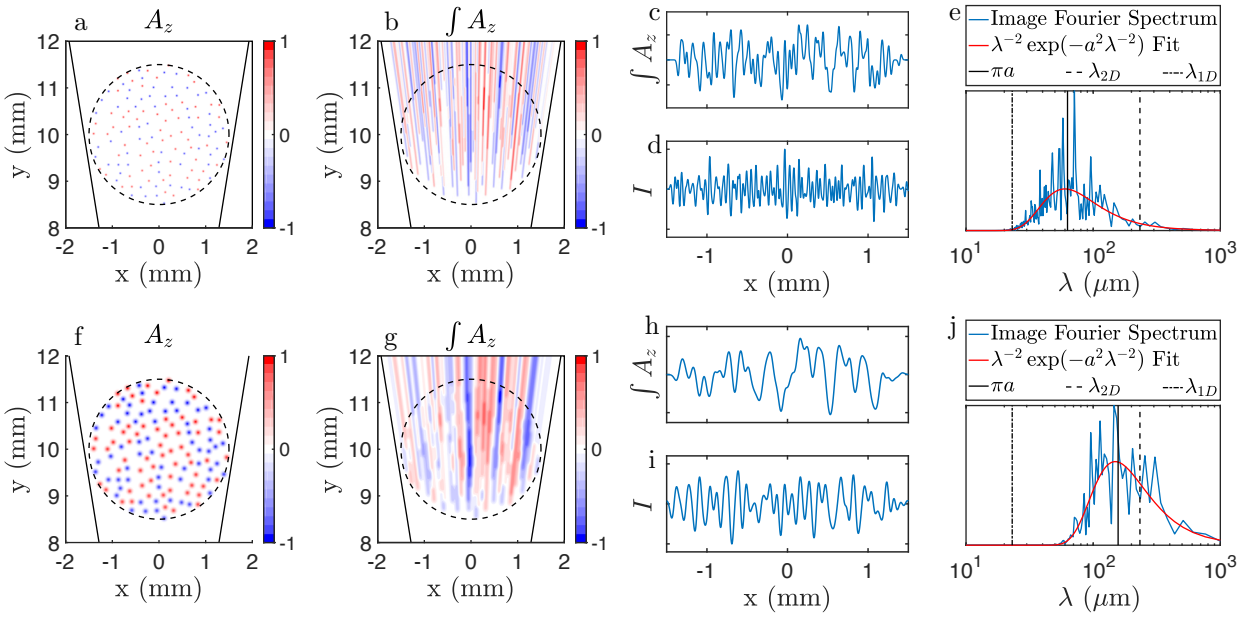

Figure 3.3: Representative results of (a) the normalized vector potential map, (b) the normalized path-integrated vector potential map, (c) the path-integrated vector potential plot at image, (d) the resulting proton fluence at an angle $\theta = 0.1$, and (e) the λ-space Fourier spectrum for a synthetic, randomized distribution of 130 filaments with $a = 20$ μm. Repeated for $a = 50$ μm in (f-j) for the same centroid distribution. The analytic fit of the synthetic Fourier spectra (red) tracks with filament size a following the derived analytic relation.

mm, $L_O = 1$ cm, $L_{OI} = 30$ cm, and the image plane is a 9.6 cm x 9.6 cm square. The synthetic proton images are created for $\theta = 0.1$, and have a resolution of 45 μm at the image plane, corresponding to 1.5 μm with respect to the interaction region. The filament centroids in the interaction region are randomized for each distribution, similar to the setup of Levy et al. (2015), with an enforced minimum distance between each filament to prevent overlap. To conform to expected physical constraints, there are an equal number of positive and negative A_z filaments in every distribution. The filament size a is varied independently of the system size and number of filaments, though these may be related in reality. Figures 3.3a and 3.3f show the vector potential of a typical distribution of 130 filaments for $a = 20$ μm and $a = 50$ μm, respectively. For each distribution of filaments we numerically integrate the vector potential along diverging proton paths to the image plane, as shown in Figures 3.3b and 3.3g, to account for magnification effects. We use the integrated vector potential to calculate α_x, and generate the synthetic 1D proton image (Figures 3.3d and 3.3i) using equation (3.14). By counting peaks in the proton image, we infer an average spacing between consecutive peaks as

$$\lambda_{I,peaks} = D/N_{I,peaks}, \tag{3.19}$$

where $N_{I,peaks}$ is the number of peaks on the image.

The results of this analysis are shown in Figure 3.4 for systems containing 130 filaments. We analyze 100 randomized distributions for each prescribed value of a to average over any distribution dependence. The median inferred λ_I approximately reaches the limit λ_{1D} at $\lambda_{1D} \approx 2a$. Above this limit $\lambda_{I,peaks}$ increases linearly with a and does not appear dependent on λ_{2D} even at large a. We therefore conclude that the forest effect is only present for cases when $a \leq \lambda_{1D}/2$, for which $\lambda_{I,peaks} \approx \lambda_{1D}$. For the case of the Weibel instability, the magnetic wavelength can be approximated as $\lambda_W \sim 4a$[79], and thus $2a/\lambda_{1D} = \sqrt{\pi N}/2$. For most cases of interest $N \gg 1$, which means $2a/\lambda_{1D} > 1$, and thus λ_I will not correspond to λ_{1D}.

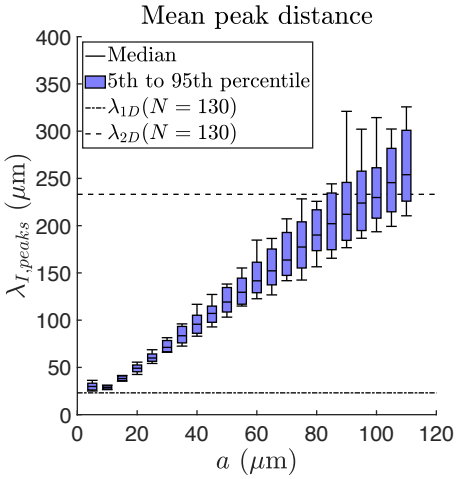

Figure 3.4: Results of the mean peak distance analysis method for 100 randomized distributions of 130 identical filaments at each prescribed filament size a. The vertical bars represent the range of inferred values of $\lambda_{I,peaks}$, and the boxes represent the range in which 90% of the inferred values lie. The lines of λ_{1D} and λ_{2D} are obtained by equations (3.18) and (3.17) for $N = 130$ and $D = 3$ mm.

3.4 Inferring Filament Size via Fourier Analysis

3.4.1 Analytic Solution

In this section we develop a simple method to determine the spatial size of the magnetic filaments from Fourier analysis of the proton images. We return to the simple analytic model of Section 3.2 and derive the expected dominant spatial mode of the proton image of a system containing many filaments. By Fourier transforming the proton image defined in equation (3.16) we find

$$\mathcal{F}\{I\} = \sum_{n}^{N} \sqrt{\frac{a^2}{2}} k^2 \exp\left(-\frac{a^2}{4}k^2 + ix_{cn}k\right). \tag{3.20}$$

The phase terms $ix_{cn}k$ in equation (16) carry information about filament position, and add deviations to the spectrum. However, when summing over the contributions from many randomized filaments these deviations will be small relative to the overall Fourier profile

$$\mathcal{F}\{I\} = Ck^2 \exp\left(-\frac{a^2}{4}k^2\right), \tag{3.21}$$

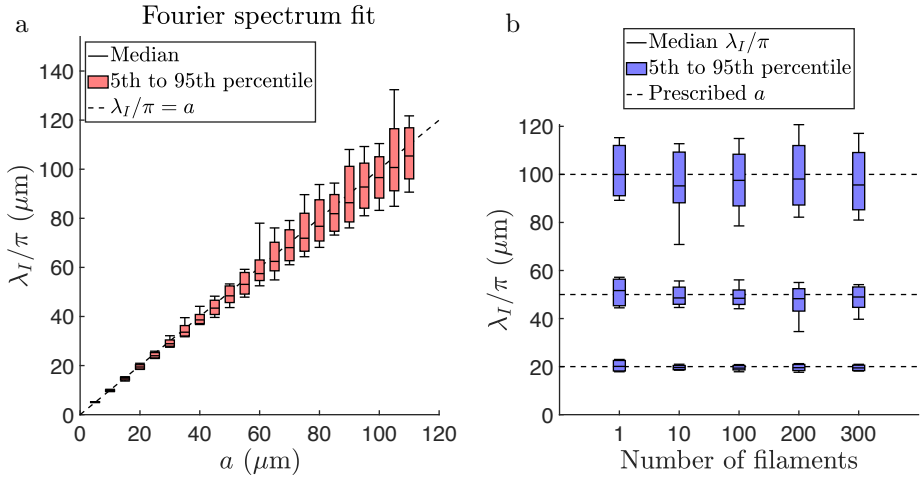

Figure 3.5: (a) Statistics of fitting the image Fourier spectrum to equation (3.24) for 100 randomized distributions of 130 identical filaments for many values of filament size a. (b) Fourier spectrum analysis statistics for 100 randomized distributions for different numbers of filaments and prescribed a of 20, 50, and 100 μm. Fitting the Fourier spectrum to our analytic relation reliably infers the prescribed filament size from synthetic proton images for all a.

which will be present for any distribution. We use this phase-free profile to find the dominant image mode

$$k_I = 2/a, \tag{3.22}$$

from which the dominant observed image wavelength is

$$\lambda_I = 2\pi/k_I = \pi a. \tag{3.23}$$

Thus, λ_I for a system of identical filaments in the linear deflection regime will primarily depend on the size of the constituent filaments and not the separation between them.

3.4.2 Statistical Verification

To test the analytic relation of equation (3.23), we again generate randomized distributions of filaments and analyze corresponding synthetic 1D proton images. Now, however, we

use equation (3.21) to determine λ_I by fitting the function

$$\mathcal{F}\{I\} = C\lambda^{-2}e^{-a^2/\lambda^2}, \tag{3.24}$$

to the Fourier spectrum of the image. The maximum value of this fit occurs at λ_I, from which we infer the filament size as

$$a_I = \lambda_I/\pi. \tag{3.25}$$

The Fourier spectra in Figures 3.3e and 3.3j show large modulations, but the fit of equation (3.24) accurately determines λ_I very close to πa for the same centroid distribution.

We test the accuracy of this method by analyzing many randomized distributions of filaments, as in Section 3.3. Figure 3.5a displays the results of this Fourier analysis method for 100 randomized distributions of 130 identical filaments for a range of independently varying a. The median inferred a_I for these distributions is within $\sim 5\%$ of the prescribed value of a, with 90% of the distributions within 15%. We also test whether the number of filaments in the system affects the accuracy. Figure 3.5b shows the inferred $a_I = \lambda_I/\pi$ for 100 distributions of systems with 1 to 300 identical filaments at a fixed $a = 20$, 50, and 100 μm. From Figures 3.5a and 3.5b, we find that this method accurately infers the prescribed filament size a, regardless of the number of filaments or filament size.

Within the assumptions made throughout this chapter, the results displayed in Figures 3.3 and 3.5 conclusively demonstrate that the effects of the independent filaments are cumulative, and filament position information is effectively lost. Instead, the proton images provide direct information about the individual size of each filament, which can be directly obtained from Fourier analysis of the proton fluence profile. Although the spectra fundamentally depends on the size, rather than the distribution, we note that in the case of the Weibel instability the filament size will be physically correlated to the spacing between filaments, implying that one can infer the scale of the magnetic wavelength by measuring the filament size a.

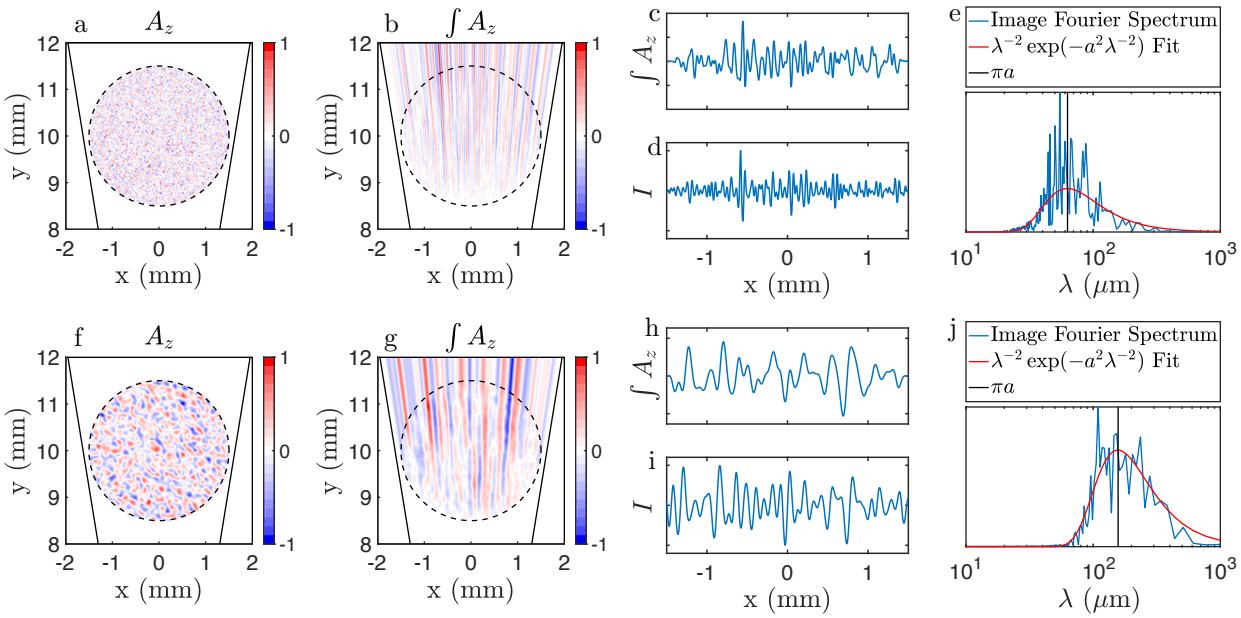

Figure 3.6: Representative results of (a) the normalized vector potential map, (b) the normalized path-integrated vector potential map, (c) the path-integrated vector potential plot at image, (d) the resulting proton fluence at an angle $\theta = 0.1$, and (e) the λ-space Fourier spectrum for a system of Gaussian random fields (rather than individual filaments) generated with spatial correlation $a = 20$ μm. Repeated for $a = 50$ μm in (f-j). The fit of the Fourier spectra again depends only on the prescribed filament size.

3.4.3 Gaussian Random Fields

A more realistic model for the magnetic field profile produced by the Weibel instability is to define the vector potential at the interaction region as a spatial Poisson process, or Gaussian random field. We follow the method described by Kroese and Botev (2015) and Dietrich and Newsam (1997) to create a stationary, zero-mean, two-dimensional Gaussian process of vector potential using the covariance function

$$\rho\left(x,y\right) = \left[1 - \frac{x^2}{l_x^2} - \frac{xy}{l_x l_y} - \frac{y^2}{l_y^2}\right] \exp\left(-\frac{x^2}{l_x^2} - \frac{y^2}{l_y^2}\right), \tag{3.26}$$

where l_x and l_y are the lengths over which the vector potential is correlated in x and y, respectively. To correlate the vector potential by the area of a generalized filament πa^2 we

set $l_x, l_y = \sqrt{\pi}a$ and rewrite equation (3.26) as

$$\rho\left(x,y\right) = \left[1 - \frac{\left(x+y\right)^2}{\pi a^2}\right] \exp\left(-\frac{x^2}{\pi a^2} - \frac{y^2}{\pi a^2}\right), \tag{3.27}$$

which is reminiscent of how we defined our Gaussian filaments in equation (3.5). Figures 3.6a and 3.6f show representative fields produced by this method at $a = 20$ μm and $a = 50$ μm. We again assume that the protons are negligibly deflected within the interaction region and follow the same process for generating proton images as in Figures 3.6d and 3.6i. The fit of equation (3.24) to the Fourier spectra accurately determines the maximum λ to be πa, just as before. Figure 3.7 shows that this method reliably infers the prescribed filament size, or spatial correlation length, from the synthetic proton just as it did for systems of individual filaments.

By modeling the magnetic vector potential of filaments created by the Weibel instability as a two-dimensional Gaussian random field, it becomes clear why we can recover the filament size parameter from proton imaging: the field is zero-mean, and integrating across a probing direction (e.g. y) essentially reduces the field to a one-dimensional Gaussian process with covariance function

$$\rho\left(x\right) = \left(1 - \frac{x^2}{\pi a^2}\right) \exp\left(-\frac{x^2}{\pi a^2}\right), \tag{3.28}$$

which reproduces the Gaussian structures observed. This analysis suggests that when probing the filamentary fields produced by the Weibel instability, and more generally for any magnetic field produced Gaussian random vector potential, in the linear proton deflection regime, that the structure size parameter can be inferred from the proton image.

3.4.4 Applicability

Our analysis is derived for proton images in the linear proton deflection regime, and it is thus important to clarify the limits of its applicability. For proton radiography nearly

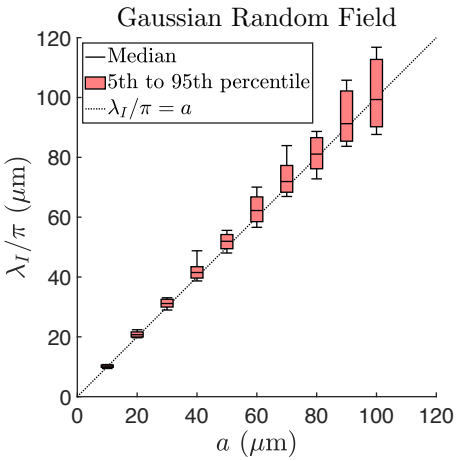

Figure 3.7: Statistics of the Fourier analysis method for 100 initializations of the vector potential as a Gaussian random field at different values of filament size (correlation length) a. Fitting the Fourier spectrum to the analytic relation again reliably infers the prescribed filament size from synthetic proton images for all a.

perpendicular to the magnetic filaments, the linearity condition can be written as

$$B_0(\mathrm{T}) \lesssim 13.4\sqrt{W(\mathrm{MeV})}/L_O(\mathrm{cm}). \tag{3.29}$$

For typical proton radiography parameters, $W = 14.7$ MeV and $L_O = 1$ cm, we expect our analysis to be valid for $B_0 < 50$ T, in agreement with the limit expressed in Kugland et al. (2012). We have confirmed this by simulating proton images of filament systems at varying magnetic field strengths. Above this limit we enter the caustic regime[54], and the Fourier spectrum starts to be significantly modified. The possibility of extending this analysis to the caustic regime is outside the scope of this chapter, and may be explored in future work.

We also note that while we have only used 1.5 micron resolution in the interaction region for our Fourier analysis, an accurate fit will generally be possible as long as the resolution is smaller than $\pi a/2$ to resolve the Fourier peak. In practice the image resolution with respect to the interaction region is limited by the proton source size, which can vary from a few microns for protons generated via Target Normal Sheath Acceleration[64] to ~ 40 μm for protons produced by the implosion of a fusion capsule[65]. This should be carefully considered

in application to future experiments, because at typical experimental conditions $a \approx 50$–100 μm.[20]

3.5 Conclusion

For systems of independent Gaussian magnetic filaments we have shown that, in the limit of linear proton deflections, proton images primarily provide information about the individual size of the filaments, not the spacing between them. We have developed a simple analytical model for the linear deflection of protons and have shown that Fourier analysis of the proton images allow for an accurate measurement of the filament size, independent of the number or density of filaments. Statistical computational analysis of synthetic proton images for many randomized distributions of magnetic filaments shows that this method accurately infers the prescribed filament size. Additionally, we have shown that when modeling the vector potential as a Gaussian random field, in which the effective filament size and number of filaments are correlated, our analysis produces the same behavior in the limit of linear proton deflection. This simple method and underlying analysis provides a robust way to characterize proton images of filamentary magnetic fields and should be broadly applicable to proton imaging of magnetic fields in plasma experiments.

CHAPTER 4

Magnetized Bow Shock Experiments

The magnetic field produced by planets with active dynamos, like the Earth, can exert sufficient pressure to oppose inflowing, supersonic stellar wind plasmas. The effective obstacle to the flow in these systems is the pressure-balance surface between the stellar wind and the magnetic field, known as the magnetopause, and a standing bow shock forms at a standoff distance upstream from the magnetopause to redirect the flow. Satellite measurements and computer models of the Earth's magnetosphere provide robust predictive capabilities for typical conditions of the Earth-Sun system, but may not be directly applicable to more extreme solar wind conditions, or to the study of exoplanetary magnetospheres. Scaled laboratory experiments provide another way to validate and improve models that predict how an external magnetic field responds when interacting with a stellar wind analog. This chapter presents results from a campaign to create astrophysically relevant bow shocks by the interaction of plasma flow with a magnetized obstacle, performed at the OMEGA laser facility. The experimental system consists of a slow, low-density plasma flow, generated by the collision and subsequent expansion of two plasma plumes, which interacts with the external azimuthal magnetic field around a current-carrying wire. The electron number density and temperature of a shock at a significant standoff distance from the wire are inferred from spatially resolved, optical, Thomson scattered spectra. Additionally, the formation of a bow shock around the magnetized wire is inferred from proton images of the magnetic fields

at 60, 70, and 80 ns after the initial laser drive for two different field amplitudes, during which time the flow encounters the magnetic field from the wire, forms a bow shock, and flows around the obstacle at a significant standoff distance.

4.1 Introduction

Astrophysical plasmas are typically magnetohydrodynamic, and because of the large spatial and temporal scales over which these plasmas evolve, the magnetic field produced by stars and some planets can significantly alter or dominate the dynamics of the surrounding interplanetary and interstellar media. The magnetic field pressure produced by these bodies separates them from the surrounding plasma, forming a magnetosphere. Stellar and interstellar winds are typically supersonic and superalfvénic, so a bow shock forms upstream to redirect the flow around the obstacle.[82] However, the effective obstacle of the magnetized body is not its physical surface, but the surface at which the magnetic field and the surrounding plasma reach pressure balance, known as the magnetopause. The standing, detached bow shock therefore occurs upstream of the magnetopause. The region of shocked flow between the bow shock and magnetopause is known as the magnetosheath. In the Earth-Sun system, the Earth's magnetic field exerts sufficient pressure to oppose the solar wind at an average distance of $\sim$10 Earth radii, with a bow shock 3 Earth radii farther upstream.[49]

Semi-analytical and empirical models of the Earth's magnetosphere based on satellite observations can determine the location of the magnetopause and bow shock for a range of observed solar wind parameters.[82,49,83,84] However, with thousands of exoplanets already discovered, there is growing interest in learning how stellar winds interact with both weakly- and strongly-magnetized planets under a range of conditions beyond those normally present in our solar system. For example, exoplanets with no or weak intrinsic magnetic fields, similar to Venus or Mars[85], that are located close to their stars are more likely to have their atmospheres stripped by stellar flare events during the earlier stages of their star's life, which has implications for atmospheric compositions, densities, and the potential evolution of

life.[86,87] A laboratory analog capable of testing the interaction of variable plasma flows with magnetized obstacles would complement numerical models, which are difficult to validate owing to the large number of free parameters and the need for both fine-scale resolution of the shear interfaces as well as large-scale tracing of field geometries in systems that evolve rapidly in time.[88] Such experiments could provide new insights into, for example, the early stages of bow shock formation, how the magnetosphere responds to more extreme plasma conditions[89], and the role of turbulence and instabilities.[50]

When scaling this system down to the laboratory, the key consideration for the viability of the experimental platform used in this chapter is the balance between ram pressure of the incoming plasma flow

$$P_{\mathrm{ram}} = \rho u^2/2 \tag{4.1}$$

and the magnetic pressure of an externally applied field

$$P_B = B_\perp^2/2\mu_0, \tag{4.2}$$

where ρ and u are the density and velocity of the incoming plasma, $B_\perp$ is the magnetic field amplitude aligned perpendicular to the plasma flow, and μ_0 is the vacuum permeability. For simplicity, we define the ratio of ram to magnetic pressure as the dimensionless parameter

$$\beta_{\mathrm{ram}} = P_{\mathrm{ram}}/P_B = \rho u^2 \mu_0/B_\perp^2, \tag{4.3}$$

with the requirement for shock formation given as $\beta_{\mathrm{ram}} \leq 1$. Achieving the necessary conditions for the formation of magnetic-pressure-dominated bow shocks requires producing a sufficiently strong magnetic field and a corresponding plasma inflow that is relatively slow and diffuse. Although the Earth's magnetopause and bow shock are the result of collisionless plasma interactions, we do not require that our experiment be collisionless, because typical ways of producing such plasmas by laser irradiation are too energetic to form a shock for the

achievable magnetic fields. The primary goal of this experiment was to create and measure a shock at a significant standoff by pressure balance between the plasma and the magnetic field.

In this chapter we report experimental observations of detached bow shock formation in the interaction of a supersonic, initially unmagnetized plasma with a strongly magnetized obstacle at the OMEGA laser facility, and the first direct measurements of the magnetic field in the shock. In these experiments our magnetized obstacle is a current-carrying wire. The stellar wind analog is created by using high-intensity lasers to generate two counter-propagating carbon plasma plumes which collide on-axis, after which the resulting radial expansion of these flows achieves favorable conditions for shock formation. Although the field topology is not dipolar, the field around the wire acts as a suitable analog to a planetary magnetic field for the purposes of generating a shock.[90] We infer plasma parameters around the location of expected shock formation from spatially resolved, optical Thomson scattering spectra measured with the Imaging Thomson Scattering (ITS) diagnostic.[55,56,60] We also use proton imaging to probe the magnetic fields within the system[65,72], which allows us to observe the formation and evolution of the bow shock in a large field of view based on features created by the compressed magnetic field. Recent z-pinch experiments[36,37] have observed shock formation around initially unmagnetized, conducting obstacles due to the pileup of magnetic field intrinsic to a plasma flow, and around a driven, magnetized obstacle. The OMEGA facility provides a diagnostic advantage for these experiments, however, as we are able to directly probe the magnetic field with proton imaging.

Section 4.2 further describes the experimental setup, detailing the colliding plasma flow source and the relative orientation of the diagnostics. Section 4.3 presents the inferred electron number density and electron temperature from ITS measurements of a likely shock transition at a significant standoff distance from the wire. Section 4.4 presents the proton images of the experiment for multiple field strengths, from which we infer the formation and evolution of a bow shock in time and measure its standoff distance upstream of the

magnetized wire obstacle. Section 4.5 concludes the chapter and presents considerations for future experiments using this platform.

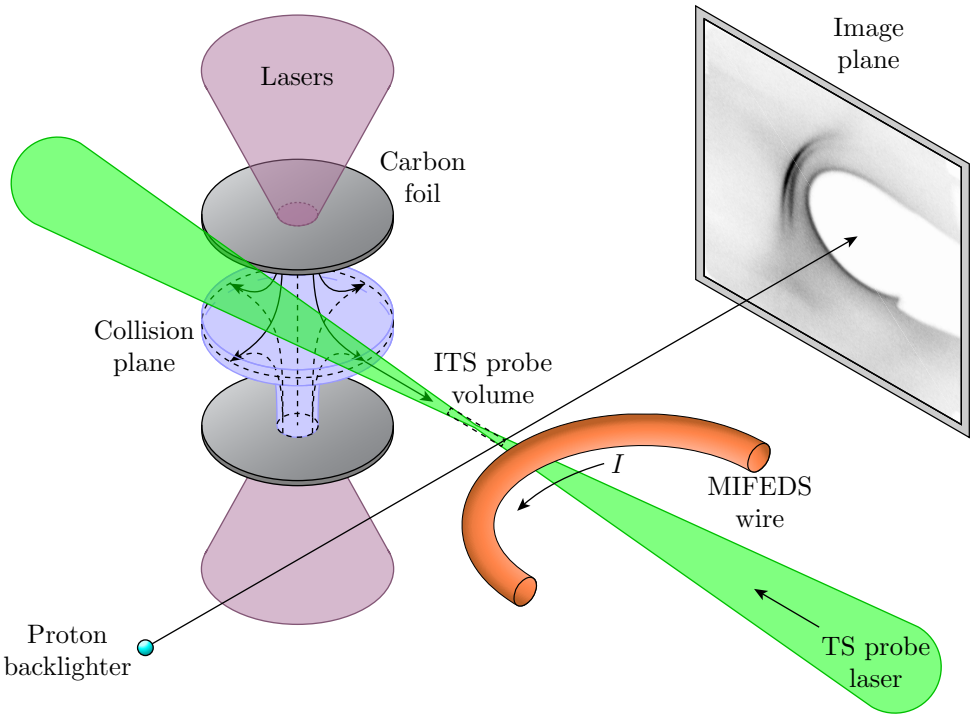

Figure 4.1: Illustration of the experiment. Two thin carbon discs are simultaneously irradiated with six 450 J, 351 nm lasers over a 1 ns square pulse within a 800 μm spot size, to generate counter-propagating plasma flows. The flows collide and expand outward toward the magnetized obstacle, which is a thin current-carrying wire driven via the MIFEDS. The ITS diagnostic measures the spectrum of Thomson scattered light from a 2ω probe beam incident at 43.7° to the primary flow axis 1.45 mm upstream of the wire in a 1.8 mm field of view along the laser axis. Protons produced by the implosion of a D^3He capsule probe the magnetic fields in the area of interest, and are captured by a CR-39 detector 16 cm away (proton image not to scale).

4.2 Experimental Setup

The experiment is illustrated in Figure 4.1, for which the primary components are the magnetized obstacle and the laser-irradiated source of plasma inflow. The magnetized obstacle is created by using the OMEGA Magneto-Inertial Fusion Electrical Discharge System (MIFEDS)[16] to drive up to 25.5 kA of current in a 760 μm diameter, kapton-insulated copper

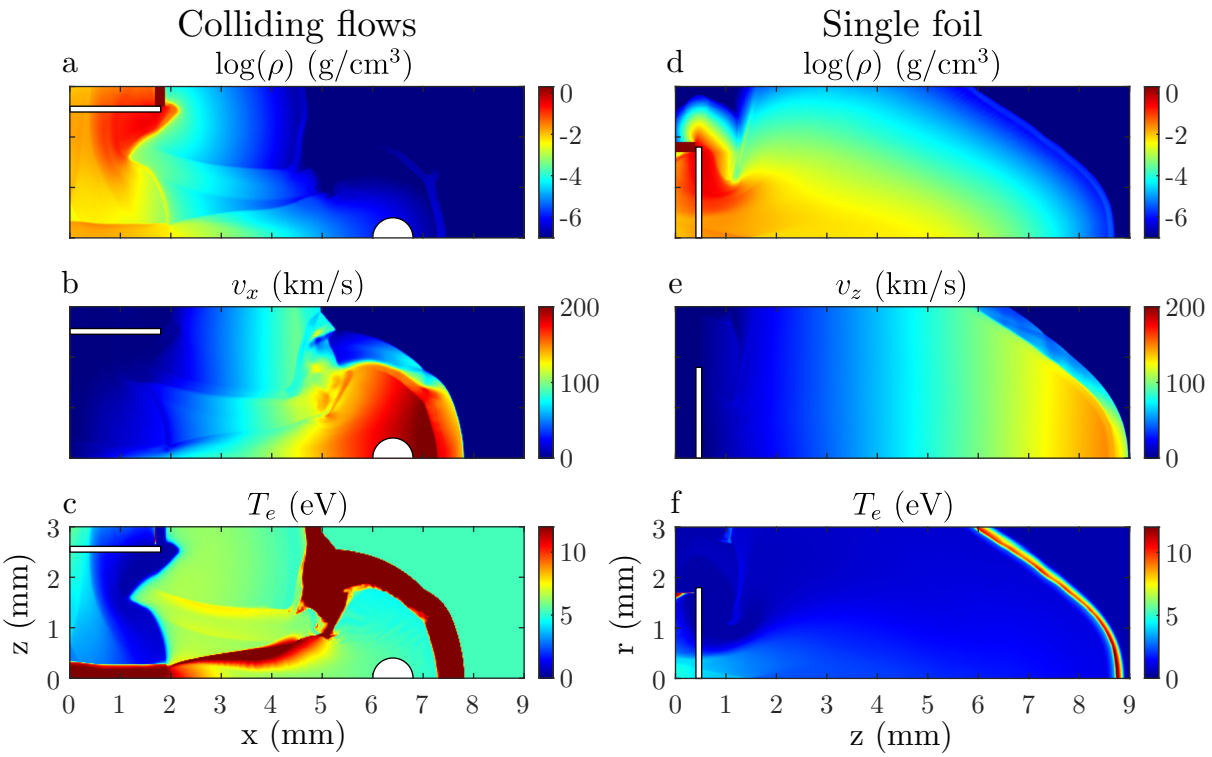

Figure 4.2: Results from FLASH hydrodynamic simulations of the colliding flow source and a single plasma plume for comparison, as labeled, 60 ns after laser drive. (a), (b), and (c) show the density, velocity in the x direction, and electron temperature for the colliding flow source. (d), (e), and (f) show the density, velocity in the z direction, and electron temperature for the single plasma plume. Each simulation is cylindrically symmetric about their z axis, along which the laser is incident, and the plane $z = 0$ is a reflecting boundary for the colliding flows. The white boxes in each image show the original extent of the solid carbon discs.

wire. The nominal 4 mm radius of curvature of the wire with respect to the experimental plane of Figure 4.1 is large compared to the system scale, determined by the wire radius, so the field can be approximated as the field around an infinite wire, which drops off as R/r where R is the radius of the wire and r is radial distance. To compare the effect of different magnetic field strengths, two nominal driven currents in the wire were used — 25.5 kA and 17 kA, which generated maximum magnetic fields at the surface of the wire of 13.5 T and 9 T, respectively. We refer to the two nominal currents as the high-field and low-field configurations. Despite the relatively large maximum magnetic fields achieved by MIFEDS at the surface of the wire, reaching the desired parameter space at a measurable standoff distance

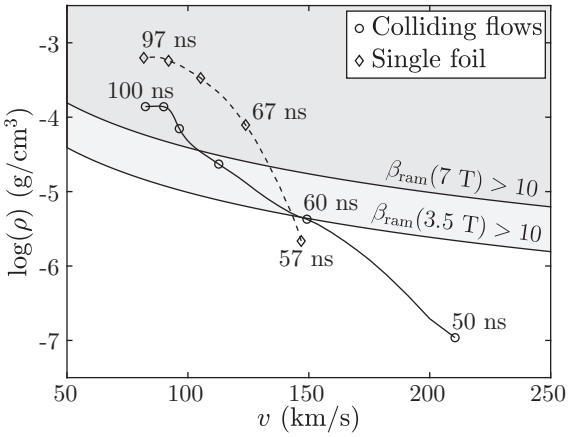

Figure 4.3: A region plot comparing the plasma parameters of the two sources in ρ-v space. The plot lines start when the plasma first reaches the point of interest, with markers at 10 ns intervals. The plasma is measured 7.5 mm from the target surface in each case, where the path length in the colliding flow case is first along the axial direction and then the radial direction after colliding. The diamond and circle symbols mark these measurement locations in Figure 4.2. The shaded regions indicate the regimes where $\beta_{\rm ram} < 10$, and the magnetic field is not strong enough to influence the flow.

requires tailoring the plasma flow source to suitable densities and velocities. Considering a maximum field of 13.5 T at the surface of the wire, at a radius of 1.45 mm, the 3.5 T field can oppose a plasma with density 10^{-6} g/cm^3 traveling at 100 km/s.

Laser-generated plasma sources are typically highly energetic, so a novel approach was used to achieve the desired parameters. The plasma inflow is created by colliding two counter-propagating plasma plumes from two laser-irradiated carbon discs. The discs are nominally 3.8 mm in diameter and 100 μm thick, oriented normal to one another and spaced 5 mm apart along the normal axis. The carbon discs are simultaneously irradiated by six 450 J, 351 nm lasers over a 1 ns square pulse within a 800 μm spot size (total irradiance $\approx 1.34 \times 10^{14}$ W/cm^2), driving a shock through each disc. The plasma flows expanding from the surfaces opposite the lasers collide on-axis at the midplane between the discs and expand outward toward the wire, which is 6.45 mm away from the collision axis along the collision plane. The expansion reduces the density of the flow that interacts with the wire, and the longer

effective path length to the wire reduces the density and velocity gradients when compared to a direct plasma plume. The reduced density makes shock formation possible, and the flattened gradients extends the duration over which favorable conditions exist.

Figure 4.2 shows density, temperature, and velocity results from 2D hydrodynamic (no magnetic field) simulations of the laser-driven plasma collision performed using the FLASH code. FLASH is a modular, open-source, Eulerian magnetohydrodynamics code which includes laser energy deposition, multigroup radiation diffusion, and tabulated equations of state (EOS) and opacities.[91,92] These simulations have 20 μm resolution, and are cylindrically symmetric about the z axis. The colliding flow is approximated by colliding a plasma plume against a reflecting boundary condition at $z = 0$. The laser parameters used in simulation mirror that of the experiment, as described above. It is immediately apparent that the two plasma flows exhibit very different properties, particularly in the gradients of the flow, where the collision source changes much more gradually than the direct plasma plume. Figure 4.3 is a region plot of the acceptable plasma parameters for 3.5 T and 7 T fields, and plots the general time evolution of plasma parameters in $\rho - v$ space for the two simulated flows, measured 1.5 mm upstream from the wire. The colliding plasma flow source is expected to have $\sim 10^{-6}$ g/cm^3 density and ≈ 200 km/s velocity 50 ns after laser drive. The colliding flow source remains in the desired β_{ram} regime (the unshaded region) for approximately 20 ns, although the first 10 ns has a lower β_{ram} and a more gradual rise in density than the last 10 ns. In contrast, the density of a the plume from a single disc, irradiated with the same laser intensity, is at least an order of magnitude greater than in the expanding flows by the time it reaches the same effective distance, and would quickly outstrip the magnetic pressure less than 10 ns after first reaching the wire. Note that these estimates do not consider any compression of the magnetic field by the flow, which could potentially reduce the plasma velocity, ease the constraints on the plasma flow and increase the standoff distance at which $\beta_{\text{ram}} = 1$, by increasing the effective field strength.

Another consideration in the formation of the bow shock is whether the plasma moves

Parameter	Solar Wind	Experiment
ρ (g/cm^3)	$\sim 10^{-23}$	$10^{-6} - 10^{-5}$
v (km/s)	400	150
T (eV)	12	6
c_s (km/s)	45	15.5
B (T)	$\sim 10^{-9}$	≤ 13.5
v_A (km/s)	~ 10	80
β_{ram}	1	$1 - 10$
M_{fms}	~ 9	~ 2
R_m	$\gg 1$	~ 4

Table 4.1: Comparison of average solar wind parameters and experimental parameters, where ρ is the plasma density, v is the velocity, T is the temperature, c_s is the sound speed, B is the external magnetic field, v_A is the Alfvén speed, β_{ram} is the ratio of plasma ram pressure to external magnetic pressure, M_{fms} is the fast magnetosonic Mach number, and R_m is the magnetic Reynolds number.

quickly enough across the obstacle while it has a $\beta_{\text{ram}} \lesssim 1$. If we consider that the obstacle is on the order of 1 mm, then at the average predicted velocity of ≈ 150 km/s between 50 and 70 ns, the flow completes approximately 3 wire crossings during the period when it has favorable conditions for shock formation. The plasma gyroradius should also be smaller than the obstacle, and for a 7 T magnetic field, the ion gyroradius is approximately 40 μm, which is sufficiently small in comparison with the 1 mm obstacle for the ions to be redirected by the magnetic field.

We must also consider the magnetic Reynolds number of this system, it must be large enough that the evolution of the magnetic field is not dominated by diffusion over dynamical time scales. Using the ~ 6 eV temperature and a velocity of 150 km/s predicted by the FLASH simulations over a 1 ns duration, we estimate a magnetic Reynolds number $R_m \approx 4$. The diffusion and advection time scales are equal on length scales ~ 300 μm. These parameters indicate that advection of the field is dominant over larger length scales, but that diffusion will still contribute over shorter distances, potentially reducing any compression of the field.

Table 4.1 compares the average solar wind parameters[51,93] with our experimental system, from which we can see that the orders of magnitude difference between the ram pressure are

balanced by the corresponding change in magnitude of the field strength. The experiment is slower than the solar wind by a factor of 3 and colder by a factor of two, and because of the strong magnetic field is in a slightly different regime than the solar wind, in that the experimental plasma has a greater Alfvén speed than sound speed. The experiment is also substantially more diffusive over the concerned length and time scales, which may affect shock evolution.

We probe the system using two primary diagnostics: spatially resolved, optical Thomson scattering spectrometry, and proton imaging. The spatially resolved Imaging Thomson Scattering diagnostic (ITS)[59,60] measures the Thomson-scattered electron plasma wave (EPW) and ion acoustic wave (IAW) spectra from the 2ω (526.5 nm wavelength) probe laser from a 100 μm $\times$ 1.8 mm cylindrical probe volume. The TS probe beam is focused where the bow shock was expected to form 60 ns after irradiating the carbon targets — 1.45 mm upstream from the wire. The probe beam has a 43.7° angle of incidence with respect to the collision flow axis. Proton imaging uses the laser-driven implosion of a 400 μm D^3He capsule as the proton source, which produces quasi-monoenergetic protons at 3 MeV and 14.7 MeV with a $\sim$100 μm source size.[65,72] The capsule is positioned 1 mm upstream from the wire along the plasma flow axis and 1 cm from the experimental plane. The protons are captured by a roughly 10 cm square CR-39 detector[65] placed 16 cm from the experimental plane on the opposite side of the wire from the source. With this geometry the proton images have a magnification of 16 between the plane at the center of the wire and the image plane.

4.3 Thomson Scattering

Thomson scattering of laser light from a plasma is a well-known method of measuring plasma parameters, where, by fitting synthetic Thomson scattered spectra to the measured spectra, we can infer the electron number density and temperature of the plasma.[56,55,57,58] At 50 ns after the initial laser drive, using the high-field setup with a 100 ps, 20 J, 526 nm wavelength probe beam, there is a sharp shift of the peak wavelength of the Thomson scat-

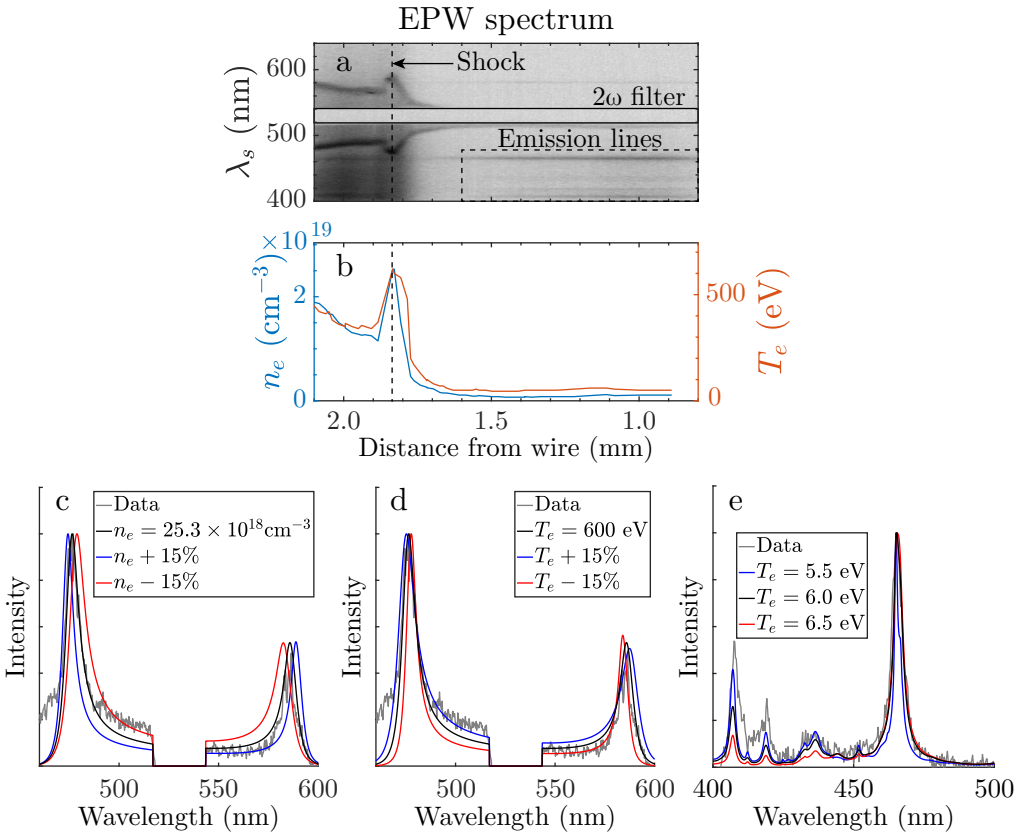

Figure 4.4: (a) The Thomson-scattered electron plasma wave spectrum, measured in wavelength λ_s, 50 ns after initial laser drive. (b) Inferred fits to electron number density and electron temperature from the spectra of (a). The position axis is calibrated relative to wire along the plasma expansion axis. The inferred shock location is overlaid as a dashed line in (a) and (b). (c,d) Best fits to the spectrum at the shock location, demonstrating that plasma parameter fits are typically accurate to within ± 15 %, in n_e (c), and T_e (d). (e) Best fit to the self-emission spectrum using PrismSPECT and assuming a carbon plasma.

tered electron plasma wave spectrum and a corresponding increase in background brightness 1.85 mm upstream from the wire, as shown in Figure 4.4a. The off-axis incidence of the probe beam complicates the orientation of the spatial axis, so we orient our results based on distance from the wire with respect to the primary axis of the incoming plasma flow. The best fits to n_e and T_e are plotted in Figure 4.4b, with errors of $\leq$15% in the fits, as shown in Figure 4.4c and 4.4d for the spectra taken at the location of maximum shift in the scattered wavelength. We infer an approximate doubling of the electron number density

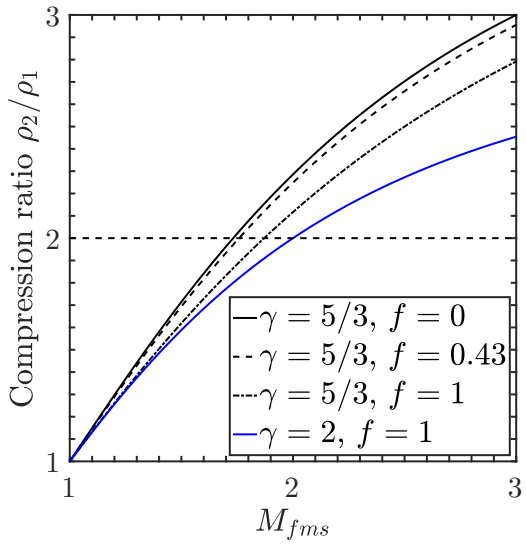

Figure 4.5: Plots of the shock compression ratio as a function of fast magnetosonic Mach number for a perpendicular MHD shock. Multiple values of f, the ratio of Alfvén speeds to fast magnetosonic speed, are shown at $\gamma = 5/3$. A plot for a fully MHD shock at $\gamma = 2$ is also shown. The dashed line at a compression of 2 corresponds to the observed compression inferred from the Thomson scattered spectra at 50 ns.

from 12×10^{18} cm^{-3} in the incoming flow to $\sim 25 \times 10^{18}$ cm^{-3} over a roughly 100 μm region between 1.9 and 1.8 mm from the wire along the detector line of sight. The number density then decreases sharply moving downstream from the spike and toward the wire, to less than $\sim 3 \times 10^{18}$ cm^{-3} at positions closer than 1.6 mm from the wire. This rapid increase in number density from the incoming flow is indicative of a shock, and the doubling factor is an important indicator of the system parameters. The large > 100 eV inferred temperature is likely a result of heating by the intense probe laser, which occurs over 10 ps. We use the PrismSPECT software[94] to calculate synthetic self-emission lines of a hot carbon plasma, and comparing to the the self-emission lines that we observe alongside the Thomson scattered spectrum (labeled in Figure 4.4a) we infer a best fit temperature of ~ 6 eV, shown in Figure 4.4e. This inferred temperature corresponds to the temperature of the plasma prior to probe heating, and agrees with simulation results of the colliding flows shown in Figure 4.2e.

γ	f	M_{fms}	T (eV)	c_s (km/s)	B (T)	v_A (km/s)	v (km/s)
5/3	0	1.73	350	167	0	–	289
5/3	0	1.73	6	15.5	0	–	31
5/3	0.43	1.76	350	167	2.85	80	326
5/3	≈1	1.87	6	15.5	2.85	80	152
2	≈1	2	6	17	2.85	80	164

Table 4.2: Sets of parameters for a perpendicular fast magnetosonic shock which result in the observed compression of 2 at a distance of 1.8 mm from the wire. The 350 eV temperature corresponds to the probe-heated plasma temperature, while the 6 eV temperature is the temperature predicted by simulation and inferred from self-emission spectra. The 2.85 T magnetic field is the amplitude of the unperturbed field at a radius of 1.8 mm.

We next consider what parameters would be necessary to produce the compression ratio of ~ 2 observed ~ 1.8 mm from the wire at 50 ns. Jump conditions for magnetized plasmas are significantly more complex than for their non-magnetic counterparts, and depend on the angle θ between the magnetic field and the direction normal to the plane of the shock.[95,43] However, the equations simplify when $\theta = 90$ degrees, and the magnetic field is perpendicular to the shock normal — as is the case in this experiment. In this limit, the relevant signal speed is the fast magnetosonic speed

$$v_{fms} = \sqrt{c_s^2 + v_A^2}, \tag{4.4}$$

where c_s is the pre-shock sound speed and v_A is the pre-shock Alfven speed.

Following Hartigan (2003), we plot in Figure 4.5 the density jump conditions for a perpendicular MHD shock as a function of the fast magnetosonic Mach number $M_{fms} = v/v_{fms}$ of the incident flow for multiple values of f, the ratio of Alfvén speeds to fast magnetosonic speed, with $\gamma = 5/3$, and the curve for a fully MHD shock with $\gamma = 2$. Although the plot shows that the necessary M_{fms} for a compression of 2 does not vary significantly for changing f or γ — between 1.7 and 2 — it is important to consider what this ratio means for the underlying system parameters. Table 4.2 shows possible sets of system parameters which produce a compression of 2 across a perpendicular shock. Importantly, the velocities v cal-

culated for each set of parameters at the necessary M_{fms} in Table 4.2 allow us to determine which system is most like the experiment.

First we consider what would happen if the system were completely unmagnetized, so the shock would be purely hydrodynamic, meaning $f = 0$, and the Mach number for a doubling of the density is $M = 1.73$. If we the shock is due to plasma conditions after probe heating by the Thomson scattering laser, the corresponding flow velocity must be 289 km/s, which is much faster than the system should be. If we instead use the inferred pre-probe temperature of 6 eV, the sound speed is 15.5 km/s, so the required flow velocity would be only 31 km/s. The parameters necessary for a hydrodynamic shock to provide the observed jump are well outside of what we expect for the system at 50 ns, either from simulations (Figure 4.2) or intuition (distance traveled by the plasma divided by time).

Now we consider magnetized systems and assume a pre-shock field amplitude of 2.85 T perpendicular to the flow, corresponding to a radius of 1.8 mm from the wire in the high-field case. The Alfvén velocity of 80 km/s is now significant. Using the probe-heated plasma temperature, $f = 0.43$ and the velocity must be 326 km/s, which is more than 100 km/s faster than we predict for this system. At 6 eV, however, $f = 0.98 \approx 1$, so the system can be considered completely magnetized, and the velocities of $\sim$ 152 km/s and 164 km/s for $\gamma = 5/3$ and $\gamma = 2$, respectively, are well within the range predicted by FLASH between 50 and 60 ns Thus, for the expected inflow conditions, a strongly magnetized plasma is necessary to achieve the shock compression ratio that we infer from the Thomson scattered spectra. Under these conditions the shock must be a fast magnetosonic shock, the same kind exhibited by the Earth's bow shock, and that we have observed the formation of an MHD shock at a significant standoff distance from the solid obstacle of the wire via Thomson scattering.

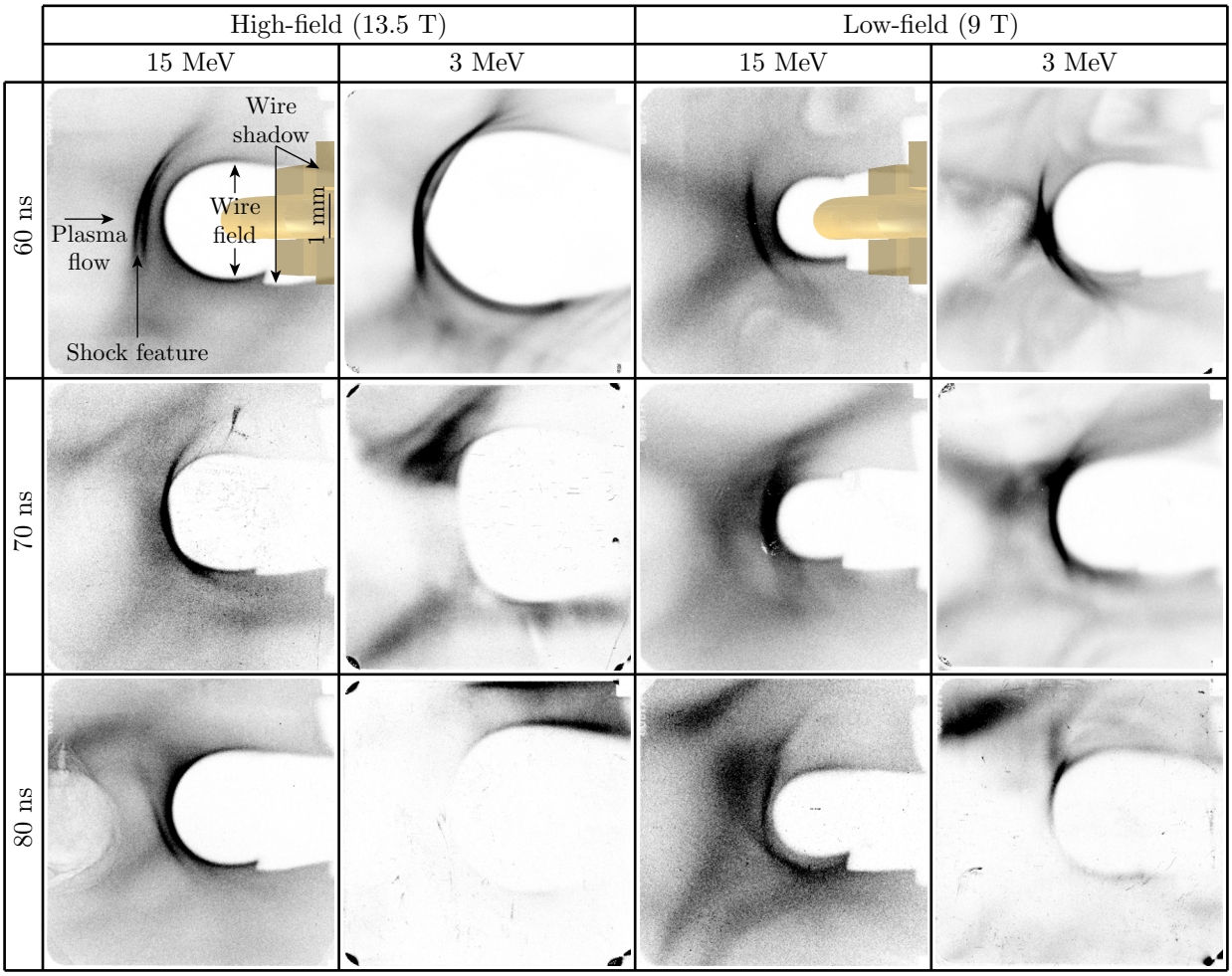

Figure 4.6: Series of proton images from the experiment. Darker regions indicate increased proton fluence. The lowest and highest 1% of values have been saturated to increase contrast of the large-scale features. There are four primary features on these images: the wire shadow, the caustic wire field feature caused by the nominal field generated by the wire, the shock feature caused by magnetic field compression, and the plasma flow feature corresponding to the inflow. A 3D representation of the wire target has been overlaid to demonstrate the wire shadow. The image scale corresponds to object plane distances.

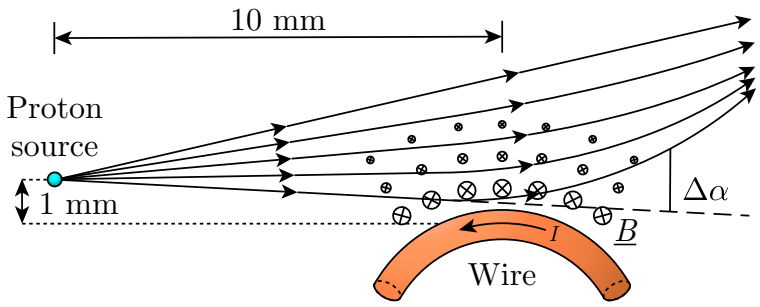

Figure 4.7: Illustration of proton deflection by the field around a current-carrying wire. The protons travel primarily antiparallel to the direction of current and are deflected radially outward from the wire. Protons that travel closer to the wire experience a stronger magnetic field and undergo larger deflections. A caustic forms at the image plane where proton trajectories cross, creating the wire field feature.

4.4 Proton Imaging

Proton imaging measures path-integrated electromagnetic fields, based on the deflected positions of probe protons at the image plane.[54] In the case of purely magnetic fields, the probe protons are deflected, based on the Lorentz force ($\underline{v} \times \underline{B}$), by fields transverse to a proton's trajectory. Images are formed based on the incident fluence of the 3 MeV and 15 MeV protons captured on a 10 cm square CR-39 detector. Because the deflections are primarily dependent on the magnetic field topology, a thorough analysis must be made to understand and predict image features.

Figure 4.6 shows the 15 MeV and 3 MeV proton images obtained in this campaign of both field configurations at 60, 70, and 80 ns. There are many features in these images, so we will first describe the known components. First, the labeled "Wire shadow" feature is the shadow caused by the wire and the structure holding it; a 3D representation of this structure has been overlaid to demonstrate its extent. The shadow is present to varying degrees in all images, and is characterized by a sharp cutoff in proton fluence without a corresponding increase outside of the shadow.

Next, the "Wire field" feature is the (mostly) annular increase in proton fluence away from the wire. To understand this feature's origin, consider the geometry of the magnetic

Field configuration	Proton energy (MeV)	Wire feature radius (cm) 60 ns	70 ns	80 ns	Analytic
High-field (13.5 T)	15	2.02 ±0.06	2.00 ±0.03	1.95 ±0.03	1.89
High-field (13.5 T)	3	3.02 ±0.10	2.98 ±0.03	2.86 ±0.10	2.82
Low-field (9 T)	15	1.42 ±0.03	1.42 ±0.03	1.50 ±0.03	1.54
Low-field (9 T)	3	1.98 ±0.06	2.06 ±0.16	2.18 ±0.06	2.29

Table 4.3: The measured radii of the wire feature from the experimental proton images and the analytic expectation using equations (4.5) and (4.6) for nominal magnetic field and proton energy parameters. The uncertainty in feature radius is determined by the width of the proton intensity maxima for each image.

field with respect to the primary probe axis. The protons probe antiparallel to the direction of the current in the wire, causing the protons to be deflected radially outward from the wire, as illustrated in Figure 4.7. Were the direction of the current relative to the probe direction reversed, the protons would instead be radially focused to a point. The outward deflection of protons simplifies analysis by spreading field information out over a larger area on the image, where in the reverse configuration information is more easily lost by overlapping proton trajectories.

The magnetic field is inversely proportional to distance from the wire, so protons that pass closer to the wire undergo larger deflections. By assuming a diverging, point source of protons, the proton trajectories will approach the ballistic trajectory from the diverging source profile as the field decreases farther from the wire. A region of increased proton fluence — a caustic — occurs on the image at the point where the deflected and ballistic trajectories of the protons cross, resulting in the wire field feature. The region closer in from this crossing point is devoid of protons, having been deflected farther out than the intensity maximum. For even modest field amplitudes, this combination of probe orientation and field topology will produce a caustic. Because the images are inherently caustic, techniques to reconstruct a path-integrated field amplitude[69,70,96] will not necessarily work. Fortunately, the system geometry is known and consistent, which allows us to infer information from the position of the image features.

To better understand the extent of the wire field feature, we analytically determine the

location of the caustic for our system by making a few geometric assumptions. The curvature of the wire is large relative to the extent of the incoming plasma profile, so we approximate the field around the wire in the experimental plane as that of an infinite, current carrying wire. Assuming a straight, 380 μm radius, 4 mm long wire centered 1 cm from the proton source and 16 cm from the image plane, the approximate radial distance of the proton fluence maximum is calculated as

$$d_{14.7\text{ MeV}} \approx 1.63\sqrt{B_0/10\text{ T}}\text{ cm}, \tag{4.5}$$

$$d_{3\text{ MeV}} \approx 2.42\sqrt{B_0/10\text{ T}}\text{ cm}, \tag{4.6}$$

for 14.7 MeV and 3 MeV probe protons, respectively, where B_0 is the maximum field amplitude at the wire surface. To apply these equations to the distance relative to the object plane (1 cm from the proton source), divide equations (4.5) and (4.6) by the 16 times magnification. Table 4.3 lists the radii of the wire field features inferred from the experimental proton images, which are consistent with the predictions of equations 4.5 and 4.6 — the radii are roughly 50% larger for 3 MeV images than the 15 MeV images, and approximately 25% larger for 13.5 T maximum fields than for 9 T. In general, the analytic approximation underpredicts the high-field radii and overpredicts the low-field radii by $< 15\%$, with greater error for the low-energy proton images. This error likely comes from a combination of geometric assumptions about the wire and from assuming a constant velocity across the length of the wire, where discrete time effects would be more important for the lower-energy protons.

From the left side of these images, upstream from the wire is a region of decreased fluence corresponding to the expanding plasma from the two colliding flows. The reduced proton fluence at the center of this feature is caused by increased scattering.The increased fluence at the edge of this feature implies the presence of intrinsic electromagnetic fields in the plasma. This feature expands laterally in time, and at late times the 3 MeV images become partially obscured by the increased density and lateral extent of plasma flowing around the wire.

Near the leading edge of the inflow feature and upstream from the wire field maximum

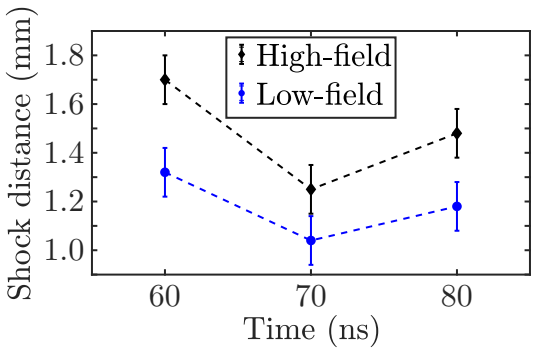

Figure 4.8: Plot of the inferred shock feature positions from the 15 MeV proton images, scaled to the object plane. The uncertainty of the inferred position is ± 100 μm, based on how accurately the center of the wire can be determined on each image.

are sharper features of increased proton fluence caused by compression of the magnetic field by the inflow, which we refer to as the shock feature. These features are observed in all 15 MeV proton images. From 60 to 80 ns the shock features move further toward the wire (to the right on the image) and drape around the wire, forming a bow, the timing of which generally agrees with the expected crossing times from FLASH simulations of the source. The two-tiered appearance of the shock feature in some images is not currently understood, but may be due to the 3D extent and curvature of the wire. The shocks may also extend farther around the wire than indicated by the leading shock feature, as evidenced in the high-field 3 MeV image at 60 ns by continuous lines that appear to be waves in the bottom right corner. The angle of these waves changes by $\sim 20^\circ$ across a surface separating a region of lower proton flux toward the wire. This rotation could indicate magnetic compression across an oblique MHD shock.

We infer the standoff distance of the leading shock features directly from the 15 MeV proton images by assuming that the deflections of the high-energy protons at the location of the shock features are relatively small, and that the highest intensity features outside of the wire field feature are produced by the shock. First, the center of the wire is inferred to be at the center of curvature of the wire field feature in each image. The uncertainty in the wire's position is ± 100 μm, because the wire field features are not perfectly circular. Figure 4.8 plots the position of the shock features inferred from the high-energy proton images in

Figure 4.6. For both field strengths, the shock feature exists farthest upstream at 60 ns, rapidly pushes toward the wire until 70 ns, and at 80 ns appears to rebound slightly for high field while remaining stationary for low field. Based on the unperturbed field profile, the real position of the shock may be up to ≈ 200 μm closer to the wire, but is difficult to determine without knowledge of how much the field is compressed.

Additionally, although we have chosen to take the location of the proton maximum as the shock position, there are more diffuse features which also resemble a shock further upstream in some images, particularly visible for the low-field case at 70 ns. It is possible that these diffuse features correspond to the true shock location, particularly since these features seem to wrap around the wire in time as we would expect of a bow shock. If that is the case, then what we currently assume to be the shock features may instead correspond to the effective magnetopause. Further experiments would be necessary to determine this.

4.5 Conclusion

From these experiments we have obtained evidence which indicates the presence of an MHD shock at a significant standoff distance from a highly magnetized wire, measured with both Thomson scattering spectrometry and proton imaging diagnostics. Features in the proton images clearly show regions where the magnetic field around the wire is compressed, which extend significant distances around and past the wire, and indicate the formation of a bow shock. The clarity of the large scale features on the proton images is notable, proving this diagnostic to be an excellent way to image shocks by way of probing changes in magnetic field topology. Additionally, because of the quasi-two dimensional aspect of the wire, we were able to analytically estimate the size of the proton image feature caused by the nominal magnetic field around the wire and compare to the data. In future experiments, careful consideration should be made of the magnetic field topology, and steps should be taken to ensure uniformity and further reduce 3D effects.

It may be difficult to generate sustained magnetized shocks at the OMEGA laser facility,

but by using the collision and subsequent expansion of two plasma plumes, we achieved the desired β_{ram} conditions for shock formation. As shown by FLASH simulations, and supported by proton images, these conditions last for approximately 10-20 ns after the flow first encounters the obstacle, allowing at most a few wire-crossing times to form a distinct bow, before the density increases enough to overwhelm the magnetic pressure. Although the shocks appear to be short lived due to the rapidly increasing density of the solar wind analog, these results are promising, with many interesting proton image features that would benefit from further investigation. With further tuning of the experimental setup, primarily to reduce the rise in density of the plasma flow, the Omega facility could provide a suitable platform for studying physics relevant to the formation and evolution of planetary bow shocks.

CHAPTER 5

FLASH Simulations of Bow Shock Experiments

Following the magnetobaric bow shock experiments at the OMEGA laser facility (described in Chapter 4), I simulated the experiment using the FLASH code developed at the University of Chicago[91,92]. FLASH is a modular, open-source, Eulerian, magnetohydrodynamics code utilizing a staggered unsplit mesh MHD solver[91], and includes extended MHD effects (i.e. Hall, Nernst, and Biermann effects, though these were not included in the following simulations), laser energy deposition, multigroup radiation diffusion, and tabulated equations of state (EOS) and opacities. These simulations were performed for two primary purposes: to characterize and verify our assumptions of the colliding plasma source, and to potentially verify analysis of the experimental data. The results of these simulations are discussed in the following sections.

5.1 Plasma Source Characterization

In this section I discuss the simulations performed using FLASH to characterize the colliding plasma source for the bow shock experiments. Specifically, these simulations test our assumptions about the colliding flow source and whether it should perform (or did perform) as expected. As described in Chapter 4, the purpose of the collision source was to tailor the plasma parameters of the inflow to achieve the necessary $\beta_{\mathrm{ram}} = 1$ condition for the formation of magnetobaric shocks. The collision was designed to reduce the density of

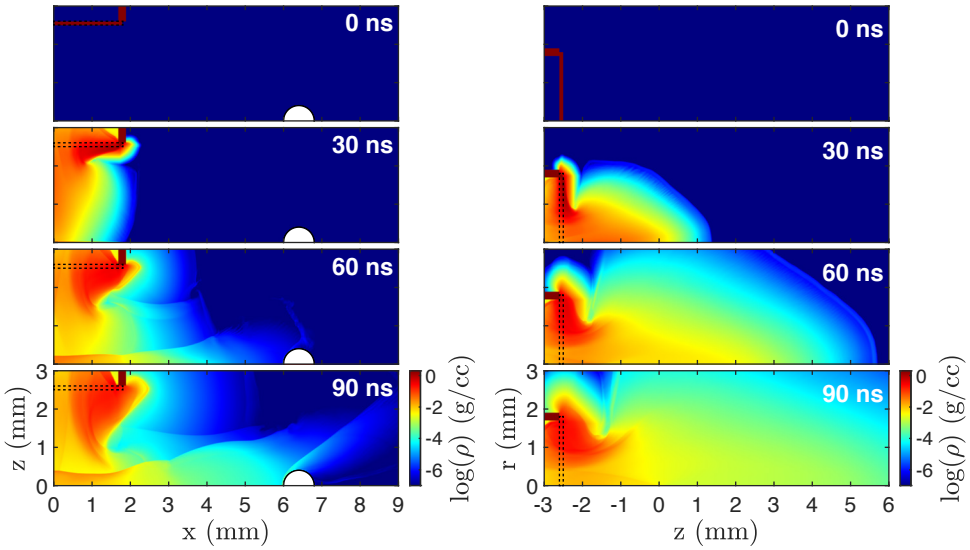

Figure 5.1: Left: time series of colliding flow source results from FLASH. Right: time series of single foil source. A boundary (unchanging in density) is present at the far edge of the foil to prevent an initial shock from traveling outward from the rear (irradiated) surface of the target. Note that the axes are flipped between images of the two simulations to follow the relevant flow axis, though both use a 2D cylindrical geometry.

the flow when compared to the blowoff of a single foil by forcing it to expand radially, so the farther away from the collision plane, the lower the density would be at any given time. Additionally, the longer effective path length over which the plasma must travel from the target to the wire would flatten the velocity and density gradients. All these effects help to decrease the ram pressure of the flow, and increase the duration for which suitable conditions for shock formation exist.

To test the assumptions about this source I compare the results from two plasma source configurations: the direct, axial plasma plume from a single, laser-irradiated carbon foil, and the plasma outflow from the collision of two counter-propagating carbon plasma plumes, as described in Chapter 4. These simulations are purely hydrodynamic, in the sense that no magnetic field was applied. The simulations used tabulated equations of state and opacities generated by the PROPACEOS software by PRISM.[97] The targets are carbon, initialized at effectively solid graphite density of 1.8 g/cm^3 with 100 μm thickness and radial extent of 1.8

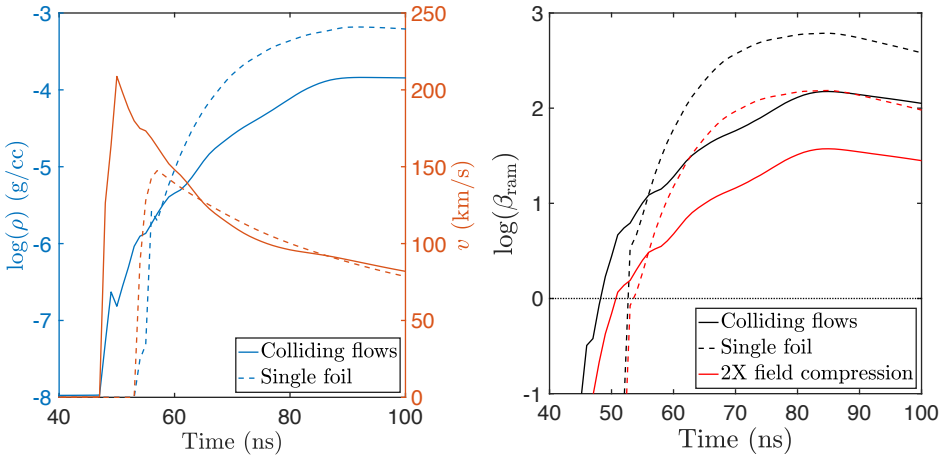

Figure 5.2: Left: comparison of density and velocity results from simulations of the single flow and colliding flow plasma sources, measured 7.5 mm from the target surface in the case of the single flow, and 5 mm radially away from the collision axis in the case of the colliding flows (equivalent 7.5 mm total path length from targets). Right: comparison of β_{ram} for the two flow sources, the black lines assuming a field strength of 3.5 T, corresponding to the field 1.45 mm away from the wire assuming a maximum field strength of 13.5 T, and the red lines assuming a 2X compression fo the field. The desired $\beta_{\text{ram}} = 1$ ($\log(\beta_{\text{ram}}) = 0$) is denoted by the dotted line.

mm. The background is an ambient helium plasma, with initial density of 2×10^{-7} g/cm^3 and a minimum density of 1×10^{-7} g/cm^3. The simulation is initialized with a temperature of 5290 K, which is likely much higher than the initial temperature in the experiment, in order to avoid issues with the PROPACEOS EOS tables which can occur at lower ($\leq$ 1000 K) temperatures. The targets are driven by a laser energy deposition corresponding to the laser properties of the experiment, the equivalent of six OMEGA beams with 400 J (89% of the nominal 450 J requested in experiment, because laser energy deposition is typically over-predicted in fluid simulations) over a 1 ns square pulse, resulting in total intensity of approximately 5×10^{14} W/cm^2.

Figure 5.1 shows a time series of density evolution from these FLASH simulations. The single-foil simulations were run in the 2D cylindrical geometry, the target and axis of laser incidence are centered on the z axis. Following laser drive, the plasma expands outward along the z axis. The two-foil simulations are similarly initialized, except the foils are positioned

5 mm from each other along the z axis, equidistant from the collision plane $z = 0$. The two targets are simultaneously irradiated, heating and driving a shock through the material. The shocks break out into the surrounding ambient medium and resulting plasma flows expand outward, primarily along the z axis, but with some radial expansion as well. The two plumes collide at $z = 0$, creating a shocked layer which heats and redirects the plasma radially outward.

Figure 5.2 shows lineouts in time of the simulated density, velocity, and estimated β_{ram} of the two flow sources. Plasma properties of the collision source are measured in the collision plane ($z = 0$) at a radial distance of 1.45 mm from the center of the wire. The flow properties of the single plasma plume were measured 6.5 mm from the target surface, the equivalent distance from each target surface as expected shock location for the colliding source. The density of the collision source is lower than the single flow by approximately an order of magnitude after 60 ns. The two cases result in approximately the same velocity in the flow. Between the two cases it is clear that, in simulation, the colliding flow achieved the desired effect, providing a lower-density inflow condition, of approximately 1×10^6 g/cm^3 and 150 km/s at the region of interest 1.45 mm from the wire. These results demonstrate that, as expected, the plasma from a single laser-irradiated target is very dense in the region of interest and contains sharp gradients, whereas the colliding source is much more diffuse throughout, and has a much more gradual density gradient. Assuming no compression of the magnetic field, the colliding flow source is estimated to achieve $\beta_{\text{ram}} = 1$ at approximately 50 ns, $\beta_{\text{ram}} = 10$ around 60 ns, and remain below $\beta_{\text{ram}} = 100$ until 80 ns. Assuming the field in front of the flow is compressed by a factor of 2 (similar to the compression of the Earth's magnetic field at the magnetopause) the collision source maintains a $\beta_{\text{ram}} < 10$ until 70 ns, which would prolong the duration of shock formation.

A notable observation from these magnetic-field-free simulations with the colliding flow is that there is no forward shock in front of the flow, and the hydrodynamic bow shock around the wire remains within 100 μm of the wire surface. This implies that the magnetic field is

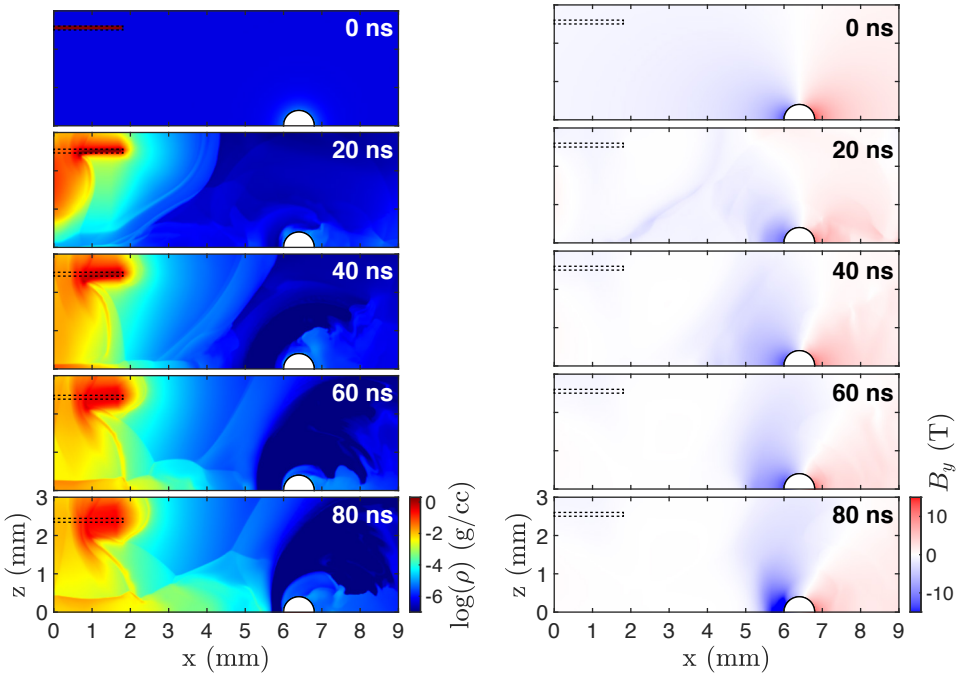

Figure 5.3: Time series of an MHD simulation of the system with a maximum field of 13.5 T, allowing for rear surface blowoff. Left: density, where the plasma propagates axially, collides with the $z = 0$ boundary, and is redirected as expected. The magnetic field sustains a shock in the expanding flow starting between 40 and 60 ns, which is observed to push toward the wire in time. Right: magnetic field in the z direction, showing significant compression of the magnetic field upstream of the wire and redirecting the field as the flow moves downstream around it.

necessary to form a shock as was inferred from the Thomson scattered spectra in Chapter 4.

5.2 2D MHD Simulations

I also performed 2D simulations of the system including various levels of magnetic field, though I only show the results from the high-field simulations here. These simulations show some good qualitative agreement with the observed structures in the proton images and Thomson scattered spectra, but are not sufficiently similar to allow more quantitative comparisons or inferences.

The system is defined in 2D cylindrical geometry with the z axis defined at the center of the carbon targets. This is not an exact match with the actual experimental geometry,

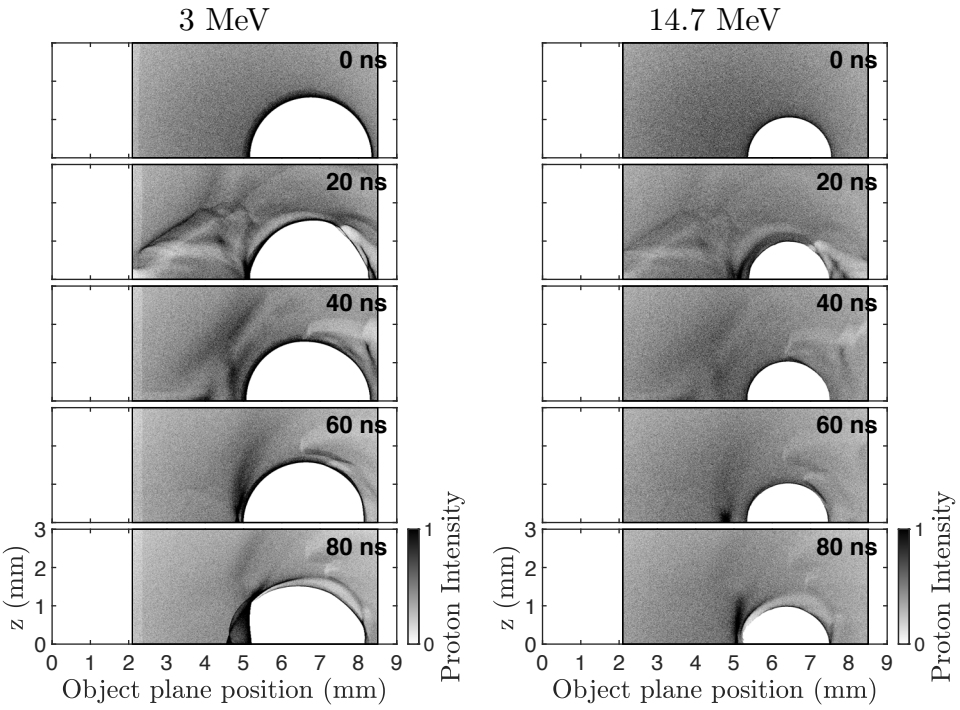

Figure 5.4: Time series of synthetic 3 and 14.7 MeV proton images using the magnetic field from the simulation shown in Figure 5.3. A synthetic volume of magnetic field is created by layering the initial field with the compressed field structure from FLASH, whose extent depends on the transverse expansion of the flow.

as the wire only has a limited extent, and is even curved away from the carbon targets, rather than around them as this geometry implies. Regardless of the imposed cylindrical symmetry, the magnetic field around the wire is initialized corresponding to the 2D Cartesian field around an infinite current-carrying wire. This mismatch of field symmetries may cause minor issues, but this is the best 2D approximation of the system because it correctly reduces the density of the flow as it expands radially, whereas a 2D Cartesian setup exhibits a much higher density at the same relative position. Unfortunately, 3D simulations would be too resource-intensive because of the large system volume. Another caveat of translating the experiment to simulations in FLASH, is that FLASH does not include any means of driving or calculating the current flowing through the wire, so to make up for diffusion of the field out of the wire, the field inside the wire is replenished to the initial state at each time step, and this inhibits field pileup on or in the wire as the flow compresses the field.

Figure 5.3 shows the results of FLASH simulations which used a maximum field of 13.5 T at the surface of the wire, the nominal conditions for the high-field case of experiments described in Chapter 4. After the initial 1 ns laser drive, the target plasma expands along the axis of laser incidence, as expected, as well as laterally, generating a shock in the ambient medium which quickly propagates outward. At just after 20 ns, the main plasma plume reaches the collision plane, creating a shock and redirecting the flow radially in the same way as in Figure 5.1. This outflow sweeps up the magnetic field and acts against an increasing magnetic pressure as it travels, forming a shock and a region closer to the wire in which magnetic pressure dominates and redirects the incoming flow. The plasma is effectively evacuated from this region due to the 2D cylindrical geometry, which likely would be rectified by moving to 3D. Unfortunately, despite forming at approximately the expected location, the density of the flow in these simulations does not match the density inferred from the experimental Thomson scattering data, it is typically too low by a factor of 4. At 80 ns and later, the incoming flow is too dense and is able to overcome the magnetic pressure, despite increasing field compression. The timing of this evolution is mostly in line with the predicted duration of favorable β_{ram} from Figure 5.2.

In the simulations, it is common to see a shock originating from the laser spot expand outward and wrap around to the front of the target very quickly, which can be seen at 20 ns in Figure 5.3. This first shock also reaches the wire, causing a reflected shock to travel back toward the axis of flow, as indicated by the increase in magnetic field ahead of the flow at 40 and 60 ns. This shock is likely the result of the high ambient density in the simulation, and may not be physical. However, the presence of this initial seed shock seems to be what allows the magnetobaric bow shock to correctly form. When a boundary is imposed on the back side of the target to block this shock in the ambient medium as was done for the hydrodynamic simulations in Figure 5.1, the colliding flows remain much more collimated, and do not seem to set up a shock as the flow approaches the wire, instead plowing through the increased field despite reaching approximately the same conditions as when there is no

boundary. In reality, at early times the shock may be initially set up by the faster, more diffuse, collisionless plasma streaming ahead of the primary flow, which cannot be captured by a hydrodynamic code. A hybrid fluid-kinetic code may be needed to more accurately model this system throughout its evolution.

Figure 5.4 shows synthetic proton images of the simulation for the same conditions shown in Figure 5.3. The synthetic proton images were created by propagating 10 million protons through a synthetic volume of magnetic field using the results from the simulation (unfortunately, FLASH does not provide any corresponding electric field). The protons are initialized with randomized diverging velocity to simulate a point source. Because the simulations are 2D cylindrical, it is necessary to construct an artificial volume of field, which is done by assuming a 4 mm length of field interaction and assuming the compressed field is limited in extent proportional to its transverse expansion. The field of the first and last 1 mm along the probe axis are defined as the initial, unperturbed wire field, and the middle 2 mm have the compressed field of the simulation result at that time. The imaging geometry is the same as described in Chapter 4, where the distance from the proton source to the center of the wire is 1 cm, and the distance from the center of the wire to the image plane is 16 cm, for a magnification of 16.

The proton images of the initial, unperturbed field at 0 ns display the same features discussed in Chapter 2 for the wire field when using a diverging proton source. At 20 ns, there is much structure visible due to the initial compression and sharp gradients of the shock expanding from the foil. At 40 ns some of this structure has evolved into a feature wrapping around the wire, most visible in the 3 MeV proton image, and corresponds to the slowing expansion of the direct blowoff. This feature further expands in time, following the evolution of the flow seen in Figure 5.3. The high-energy proton images show less of this feature, but at later times more prominently show a limited region of increased proton fluence similar to the forward shock features of the experimental data discussed in Chapter 4. Additionally, this same field structure results in an overlap feature in the 3 MeV images,

which is again similar to the data. This qualitative analysis of the images, assuming a tiered field structure, is approaching the limit of what can be done with these simulations. The conflicting 2D geometry and the construction of a synthetic field volume make it difficult to make truly quantitative inferences with respect to the experimental images.

5.3 Discussion

The question that might be asked at this point is: Why use a fluid code? A fluid code does not capture any kinetic effects, which are likely important for this system at early times, but global MHD models have been shown to reproduce the location of the bow shock and magnetopause due to the pressure balance, as well as the plasma density, temperature and magnetic field strength outside of the magnetopause.[89,98] These codes are not typically well-equipped to determine properties of the inner magnetosphere, however, because kinetic effects (and high resolution) are required to couple the outer and inner parameters. Of course, the codes used to perform magnetospheric simulations are designed specifically for use in the magnetosphere or astrophysical plasmas, whereas FLASH is a more multi-purpose code whose strength lies in its modularity and especially in its application to laboratory HED systems. As such, it is no surprise that issues arise in these simulations when a shock exists that is sustained on one side by magnetic pressure. I have typically observed that once the shock becomes dominated by magnetic pressure on one side of the shock, it allows the plasma pressure to drop to (essentially) zero on that side. Because of this, what results is an evacuation of the plasma in the sub-magnetopause (or perhaps sub-shock) region closer to the wire analog. This most likely affects the dynamics and evolution of the plasma after this point, but with the knowledge that even space weather codes need specific coupling models to get the inner magnetosphere correct, it is not unexpected.

What *is* somewhat unexpected is that these simulations do not seem to quantitatively reproduce the overall features observed in proton images and even Thomson scattering data. This mismatch suggests that there are, perhaps, more serious underlying issues with at least

the setup and execution of these simulations. These could perhaps arise from a lack of resolution, the (pseudo-) 2D geometry rather than 3D, high ambient plasma density and temperature, and a smoothing-over of thermal conduction terms. However, addressing any of these potential issues requires a significant (and perhaps insurmountable, given resource constraints) increase in time and computational resources. It is disappointing that the MHD simulations were not more directly applicable to the data, but much was learned, qualitatively, like the general location of the shock and perhaps the influence of the more direct flows. Particularly important is that, because FLASH models the HED hydrodynamics of the system well when there are no magnetic fields, and since no shock is observed in those simulations, we can conclude that the magnetic field does significantly affect the flow.

CHAPTER 6

Conclusion and Future Work

This thesis has covered experiments and analysis that I have performed in regards to magnetized, astrophysically relevant plasmas. Magnetized HED experiments will likely remain a topic of interest for some time, especially as the available magnetic fields increase, and as application broadens to more ICF-relevant systems. When thinking about the overall impact of some of these more astrophysically motivated experiments, it is the diagnostic access and control of experimental parameters which make them worthwhile. The common thread between the experiments presented in this thesis is the method of probing the magnetic field: proton imaging.

Chapter 2 presented an overview of proton imaging methods, focusing on analysis techniques when dealing with deflections by magnetic fields. I worked through the common assumptions that have been used for approximating proton intensity maps since at least Kugland et al. (2012): that of paraxiality and that the proton source is collimated. I then expanded upon this derivation to show that there are important effects to consider in more realistic, diverging proton sources — perspective, and off-axis velocity components. Using a Gaussian ellipsoidal magnetic field topology, which was assumed for the Weibel filament work presented in Chapter 3, I demonstrate that perspective has a significant effect on the resulting image. When probing parallel to the axis of the single-component vector potential, adding perspective changes the path-integrated field topology, so the resulting proton image

features are not symmetric, as would be seen with a collimated source. When probing perpendicular to the vector potential axis, it turns out that the primary driver of the image is the interaction of the off-axis velocity components (in the direction of the vector potential) with the fields, and when these are not considered (like with collimated probing) there would essentially be no deflections. I also derived the location of caustic formation when probing parallel to the field around a current-carrying wire, which is used in the analysis of Chapter 4. If I could pick one aspect of this work that readers take away, it is that proton imaging analysis requires a careful consideration all geometric aspects of the system.

Chapter 3 then delved into the specific proton imaging situation of imaging perpendicular to a system containing many small-scale magnetic filaments. This system arises in experiment via the collisionless interpenetration of two plasmas, driving the Weibel instability. The driving question behind the analysis of these images was how the two-dimensional proton images corresponded to the underlying three-dimensional magnetic field topology. Prior to the publication of this analysis in Levesque et al. (2019), the common assumption was that the spacing of the regular patterns observed on the proton images corresponded to some internal spacing of the filaments. By breaking down the imaging problem by assuming small-deflections, I was able to define the image features using linear operators on the image corresponding to each filament, and the final image was just the summation of all the operators over all filaments. This approach was verified when comparing these operator images to more sophisticated calculations of the entire system. Importantly, this operator-based approach revealed that underlying field information could in fact be recovered from a proton image in this situation by analyzing the Fourier spectrum. The Fourier spectrum of a lineout of the proton image would contain the Fourier summation of the underlying filaments, from which we can determine the size of the constituent filaments. This result has important implications for the understanding of proton images in this specific system and in general: the features observed on proton images should generally correspond to the *extent* of the field structures, and not on any spacing. More work exploring further generalizing proton

imaging structures could potentially uncover some more fundamental analysis methods, but as I tried to convey in Chapter 2 and throughout, geometry is such an important driver of these images that trying to generalize may not be worthwhile.

Chapters 4 and 5 covered the magnetized bow shock experiments. In these experiments, we were able to achieve conditions favorable for the formation of a bow shock around a magnetized obstacle, where the magnetic pressure was sufficient to oppose the incoming plasma flow at a significant standoff distance away from the obstacle's surface. Just achieving the necessary parameters was a significant challenge, and required a new configuration of colliding two laser-generated plasma plumes to drive the experiment by the plasma that expanded from the collision plane. Measurements of the number density and temperature in the plasma made with Thomson scattering indicate the presence of a shock by a rapid doubling of these parameters with respect to the incoming flow parameters. Proton imaging proved to be a reliable and insightful diagnostic, as we could observe the evolution of a shock around the wire based on the changing magnetic field topology. Unfortunately, calibrating measurements between the two diagnostics proved to be implausible, primarily because the small ITS probe volume is very sensitive to slight changes in the location of the wire, as opposed to the proton images, which can image the entire system. Additionally, the hydrodynamic and resistive MHD simulations performed using FLASH enabled us to predict properties of the colliding plasma source, and to determine that the magnetic field has a significant effect on the flow, although the two-dimensional geometry of the simulations proved to be a significant obstacle. I was also able to qualitatively piece together some features we observed on proton images by creating synthetic proton images from the simulation output and better understand how the feature distance on the images correlated to the real position of the shock.

Fundamentally, the bow shock experiments were a success, both as a platform and in terms of considerations for proton imaging, and they will provide a basis for further exploration. This platform could likely be improved by a few changes: constraining the system to

be more two-dimensional, using TNSA proton imaging for higher resolution, simultaneous Faraday rotation imaging perpendicular to the proton image axis, and a new plasma source. Some preliminary reading suggests that a Hall thruster may be a good plasma source — it would be very low density, and have a consistent flow. With a plasma thruster, the physics would be a bit different, the low density would constrain it to the kinetic regime which could provide better similarity to astrophysical bow shocks, and instead of observing the formation of the shock, the shock would likely be fully formed before the proton probe time because the thruster would likely need to be turned on well before any lasers. There are, of course, other options that could be explored for a new plasma source, perhaps altering the geometry of some colliding flows, but simplicity and consistency would be advantageous.

In terms of physics that could be explored, there are signs of propagating Alfvén or magnetosonic waves in the high-field 3 MeV proton image at 60 ns, which change direction, indicating that the shock has a larger extent than we have inferred. The low-field proton images at 60 ns also show interesting extraneous focusing features downstream of the shock, along its side. These features may very well correspond to the formation of a vortex sheet as the plasma flows around the leading edge of the bow shock, which perhaps cannot be sustained as the magnetic field becomes more parallel to the flow. This could suggest that in the early stages of bow shock formation, before the magnetosphere is fully formed, the stellar wind has more turbulent components which may allow it to reach farther in toward a protoplanet. Additionally, this could be of use for understanding our own space weather, as it indicates that sudden increases in intensity of the solar wind may induce such rollups in the Earth's magnetosphere, relevant to the findings of Moore et al. (2016). In closing, the initial results of these experiments are promising, and deserve further refinement and investigation.

APPENDIX

APPENDIX A

Additional Experimental Data

A.1 Proton Images (August 2016)

The first shot day of this campaign using proton imaging had a slightly different setup: we used two offset wires in the proton field of view, one of which was driven and the other was unconnected, presumably allowing us to see the effect of magnetic field on the flow simultaneously with a null wire. This setup ended up not being as useful as desired, as the necessary offset of the wires from the expanding plasma axis changes the incidence of the incoming flow on the plasma, and we discovered during these shots that the flow is structure. Additionally, we had not defocused the lasers incident on the implosion capsule until the final shot with the antiparallel current, so the parallel-current shots had reduced proton yield, reducing the image quality. We were able to drive a maximum current of 15 T for these shots, but we also had only one shot in which the current was antiparallel to the probe protons, the others were parallel, causing the protons to be axially focused on the image, as described in Chapter 4 Section 4.4. In the focusing configuration of Figures A.1 and A.2, the resulting caustic is much more difficult to analyze in terms of determining field strength, and magnetic compression in Figure A.2 is only recognized in the deflection of the wire feature and regions of decreased proton intensity, rather than sharp increases. Fortunately, we did

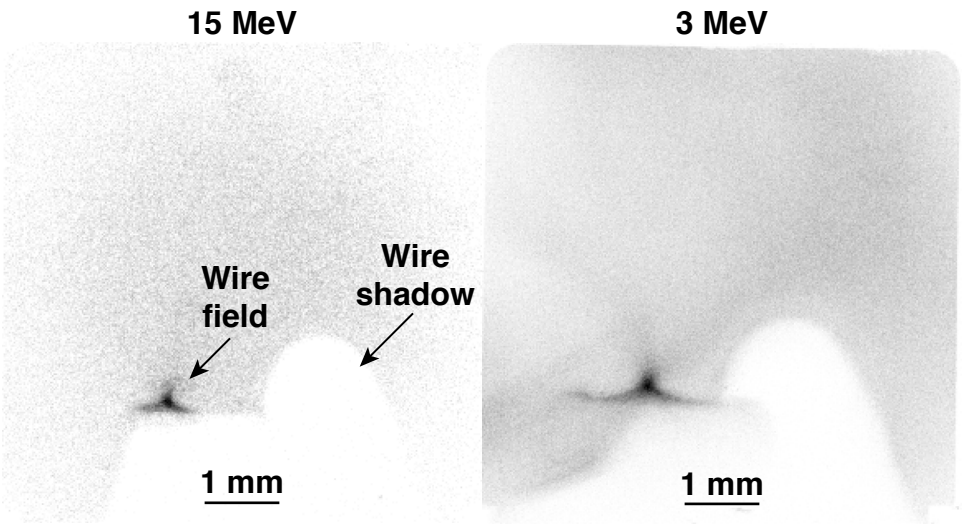

Figure A.1: Proton images from shot 82490 in the parallel-current configuration, for a maximum field of 15 T at the surface of the wire with no incoming plasma flow . The wire field feature deflects protons to a point (and beyond), making it difficult to determine field strength from this caustic.

capture a significant shock for our one good shot with antiparallel current, as shown in Figure A.3, and these features closely resemble what we see in the high-field proton images from the second shot day (a double-banded increase in proton intensity upstream of the wire), as presented in Chapter 4. The 3 MeV image in Figure A.3 clearly shows the large extent of the shock from the high magnetic field. Unfortunately, the null wire does not seem to have much effect on the flow, except maybe a diffuse indication of a shock at the very right of the 3 MeV image.

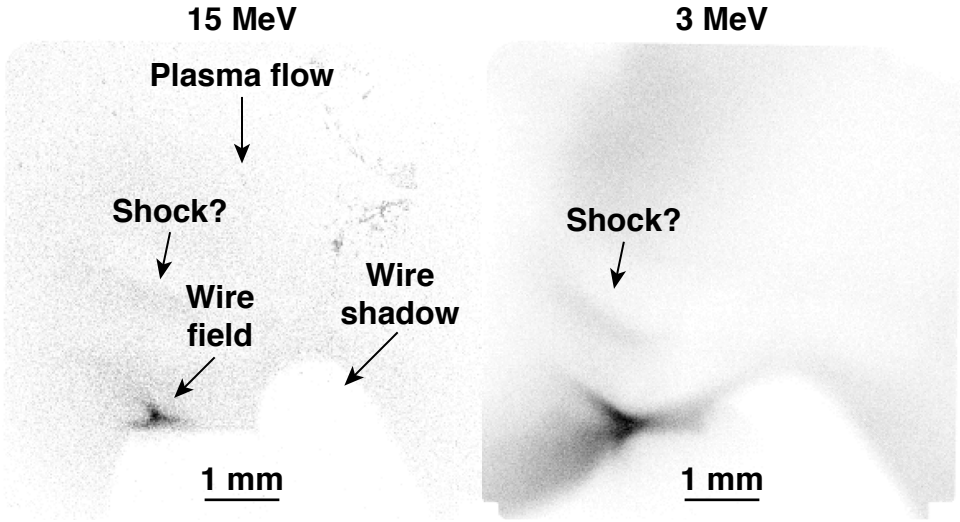

Figure A.2: Proton images from shot 82487 in the parallel-current configuration, probing 60 ns after drive for a maximum field of 15 T at the surface of the wire. The wire field feature is deflected from the null flow case, and there are indications of magnetic field compression by decreases of proton intensity upstream of the wire. Inferring shock position or field strength from this image would pose a significant challenge.

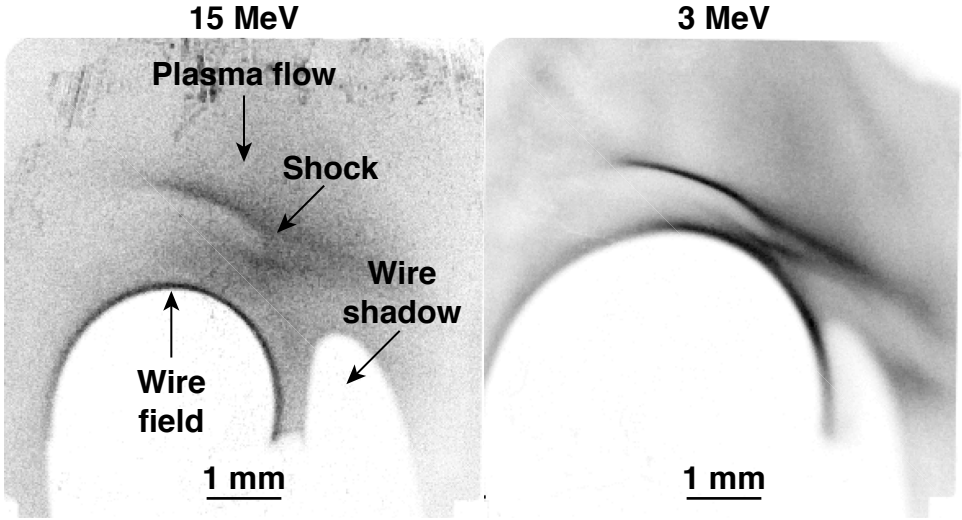

Figure A.3: Proton images from shot 82491 in the desired antiparallel-current configuration, probing 60 ns after drive for a maximum field of 15 T at the surface of the wire. The image features closely resemble the later images as described in Chapter 4. The 15 MeV image shows some imperfections or damage on the edge closest to the plasma inflow.

A.2 Additional Thomson Scattering Measurements (December 2016)

Although the data presented in Chapter 4 concerns only the EPW spectra from a single shot, there was more extensive use of Thomson scattering throughout the second shot day. We used ITS as the sole diagnostic for two shots using the high-field configuration at 50 ns, during which the probe beam was at roughly 20 J over a 100 ps square pulse, which resulted in the best data (shown in Figure 4.4). Figure A.4 shows the EPW (with best fit) and IAW spectra measured for the two high-field shots at 50 ns. As before, a shock is visible in the inferred density jump from the EPW spectrum of shot 83878, and there is a corresponding translational shift of the scattered peaks in the IAW spectrum which correspond to a change of the bulk velocity (along the axis from the plasma to the detector), another indication of a shock. The IAW measurement for this shot was not used in the analysis of Chapter 4 because the additional degrees of freedom (ionization state, flow velocity, ion temperature) when compared to the EPW spectrum (electron number density, electron temperature) make IAW spectra more difficult to fit. The second of these shots (shot 83879) does not show this same jump on either the EPW or IAW spectrum, though the rest of the profile looks similar. There are many possible reasons why this could have occurred, the most likely is that the combination of random structure in the incoming plasma, which could easily shift the timing, alongside the relatively large potential for error in positioning inherent from the small ITS probe volume coupled with imperfections in and misalignment of the wire resulted in the ITS not measuring the same place or time as the previous shot. From these ITS data alone, one could imaging that the shock is transient or random, but the proton images show definitively otherwise.

We also used ITS alongside proton imaging, probing 5 ns after the proton implosion to prevent creating perturbations in the flow and field structure from the probe laser that would affect the proton images, and to ensure that the CCD would not be saturated or damaged by emissions from the proton backlighter. However, for these shots it was necessary to use a 1 ns square pulse for the probe beam, since it was on the same driver as the lasers driving

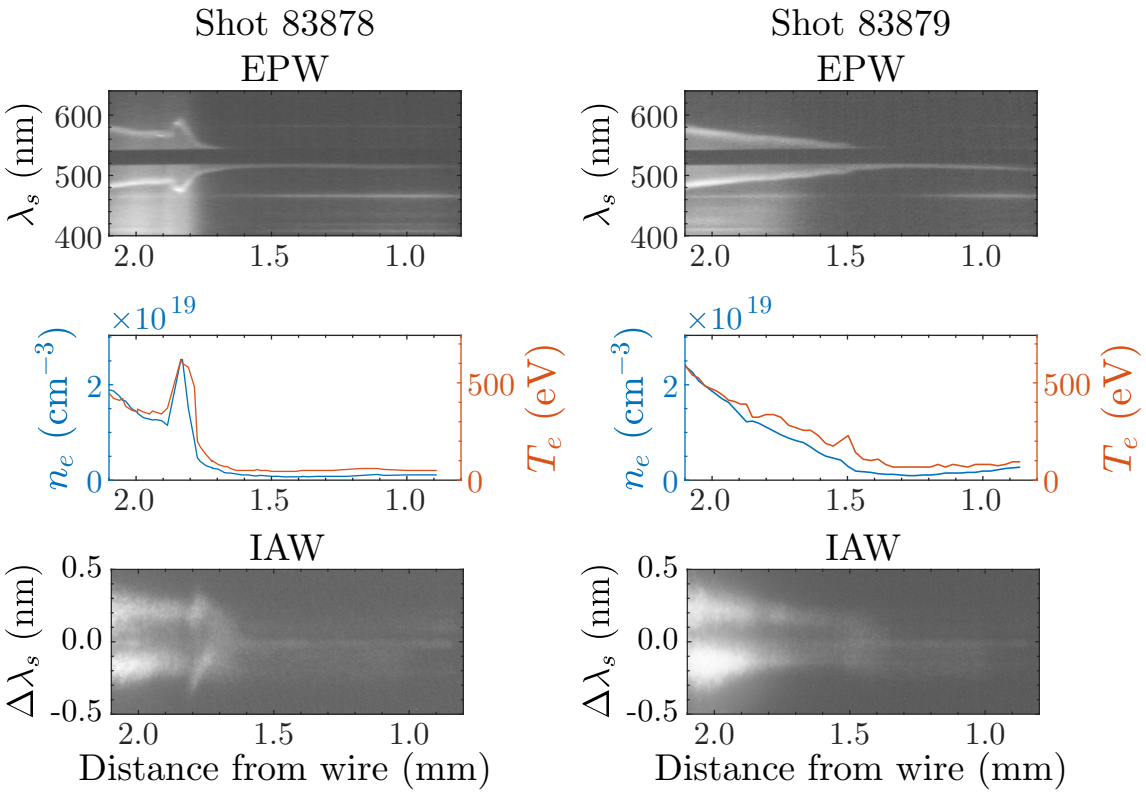

Figure A.4: ITS data and inferred plasma parameters from the two shots at 50 ns in the high-field configuration, using the 100 ps, 20 J probe beam. The shock jump is only seen in one shot, although the background profile is similar for both. Deviations in wire positioning and random structure in the incoming plasma flow causing an effective shift in timing may be the cause of the irreproducibility in the ITS.

the proton backlighter implosion. The extra energy (∼300 J) and extended pulse duration increased the effect of the probe on the plasma, and contributed to much confusion for the IAW measurements, in particular. The shocks measured using ITS never seem to match the inferred position from the proton images, likely owing to the 5 ns difference in timing and the angle of the probe beam.

Figure A.5 shows the high-field EPW spectra and the inferred parameters taken using the longer-pulse configuration at 75 and 85 ns (the shot at 65 ns had too much filtering). No significant structure is observed at 75 ns. The jump at 85 ns indicates a shock, and is fairly close to the shock position inferred from proton images reported in Figure 4.8, although different in profile from what we observe at 50 ns. Figure A.6 shows the high-field IAW

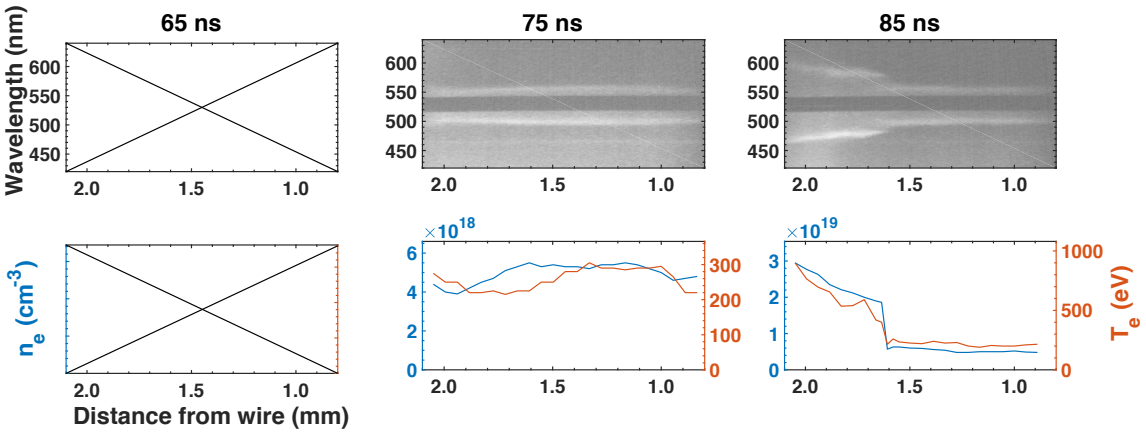

Figure A.5: High-field EPW spectra and the inferred parameters taken using the longer-pulse configuration at 75 and 85 ns (the shot at 65 ns had too much filtering).

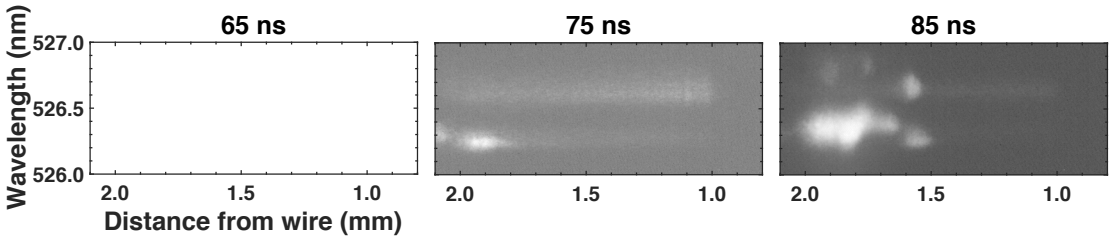

Figure A.6: High-field IAW spectra using the longer-pulse configuration at 75 and 85 ns (the shot at 65 ns had too much filtering).

spectra using the longer-pulse configuration at 75 and 85 ns (the shot at 65 ns had too much filtering). The segmented structure (three sets of blob-like peaks) is difficult to interpret, but likely corresponds to regions across the shock, since they occur at roughly the same region we see a shock in the EPW spectra.

Figure A.7 shows the low-field EPW spectra and the inferred parameters taken using the longer-pulse configuration at 65, 75, and 85 ns. At 65 ns there is a significant spike in plasma parameters, and likely corresponds to the shock. Looking at the corresponding proton images for this shot, the shock does have an azimuthal asymmetry, so the relatively far distance from the wire may be a result of the ITS probe beam angle. As in the high-field case, no significant structure is observed at 75 ns, which is strange, so there may have been some systematic error we did not catch for those two shots, which were performed back-to-

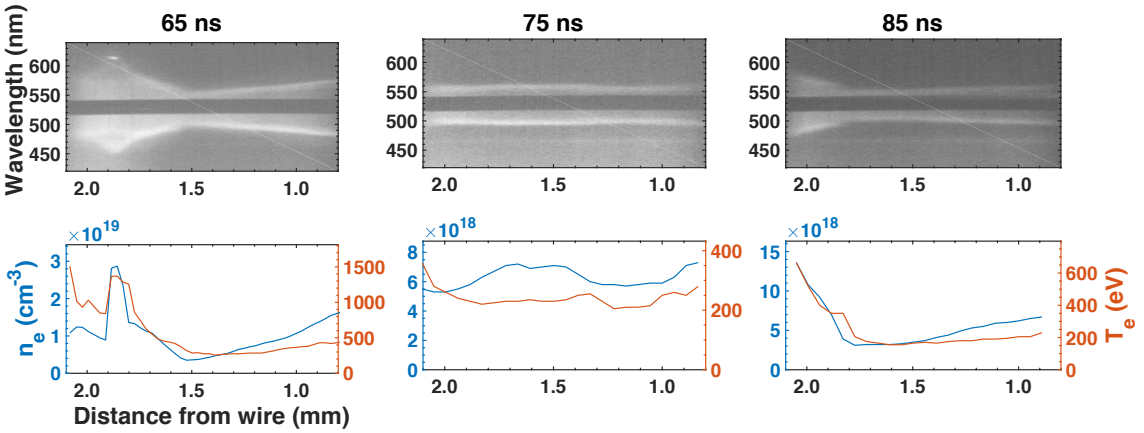

Figure A.7: Low-field EPW spectra and the inferred parameters taken using the longer-pulse configuration at 65, 75, and 85 ns.

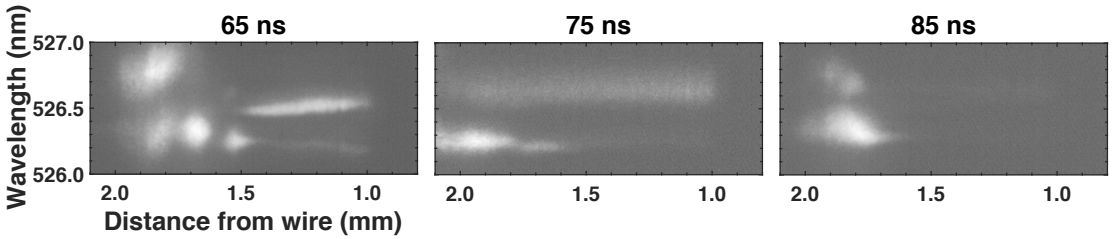

Figure A.8: Low-field IAW spectra using the longer-pulse configuration at 65, 75, and 85 ns

back. At 85 ns there is a ramp-up in density starting 1.8 mm from the wire, which may be a shock, which could correspond to the diffuse increase in proton intensity farther out than the inferred shock position for that shot. Figure A.8 shows thezlow-field IAW spectra using the longer-pulse configuration at 65, 75, and 85 ns. The segmented structure occurs again in the 65 ns and 85 ns measurements, following the shock structure. However, aside from agreeing in location, the asymmetries and width of these features make it hard to quantitatively infer more plasma parameters.

BIBLIOGRAPHY

BIBLIOGRAPHY

[1] Drake, R Paul. *High-Energy-Density Physics*. Springer International, 2 edition, 2018.

[2] John Nuckolls, Lowell Wood, Albert Thiessen, and George Zimmerman. Laser compression of matter to super-high densities: Thermonuclear (ctr) applications. *Nature*, 239 (5368):139–142, 1972. doi:10.1038/239139a0.

[3] S. Le Pape, L. F. Berzak Hopkins, L. Divol, A. Pak, E. L. Dewald, S. Bhandarkar, L. R. Bennedetti, T. Bunn, J. Biener, J. Crippen, D. Casey, D. Edgell, D. N. Fittinghoff, M. Gatu-Johnson, C. Goyon, S. Haan, R. Hatarik, M. Havre, D. D-M. Ho, N. Izumi, J. Jaquez, S. F. Khan, G. A. Kyrala, T. Ma, A. J. Mackinnon, A. G. MacPhee, B. J. MacGowan, N. B. Meezan, J. Milovich, M. Millot, P. Michel, S. R. Nagel, A. Nikroo, P. Patel, J. Ralph, J. S. Ross, N. G. Rice, D. Strozzi, M. Stadermann, P. Volegov, C. Yeamans, C. Weber, C. Wild, D. Callahan, and O. A. Hurricane. Fusion energy output greater than the kinetic energy of an imploding shell at the national ignition facility. *Phys. Rev. Lett.*, 120:245003, Jun 2018. doi:10.1103/PhysRevLett.120.245003.

[4] O. A. Hurricane, P. T. Springer, P. K. Patel, D. A. Callahan, K. Baker, D. T. Casey, L. Divol, T. Döppner, D. E. Hinkel, M. Hohenberger, L. F. Berzak Hopkins, C. Jarrott, A. Kritcher, S. Le Pape, S. Maclaren, L. Masse, A. Pak, J. Ralph, C. Thomas, P. Volegov, and A. Zylstra. Approaching a burning plasma on the nif. *Physics of Plasmas*, 26 (5):052704, 2019. doi:10.1063/1.5087256.

[5] T. R. Boehly, R. S. Craxton, T. H. Hinterman, J. H. Kelly, T. J. Kessler, S. A. Kumpan, S. A. Letzring, R. L. McCrory, S. F. B. Morse, W. Seka, S. Skupsky, J. M. Soures, and C. P. Verdon. The upgrade to the omega laser system. *Review of Scientific Instruments*, 66(1):508–510, 1995. doi:10.1063/1.1146333.

[6] J. M. Soures, R. L. McCrory, C. P. Verdon, A. Babushkin, R. E. Bahr, T. R. Boehly, R. Boni, D. K. Bradley, D. L. Brown, R. S. Craxton, J. A. Delettrez, W. R. Donaldson, R. Epstein, P. A. Jaanimagi, S. D. Jacobs, K. Kearney, R. L. Keck, J. H. Kelly, T. J. Kessler, R. L. Kremens, J. P. Knauer, S. A. Kumpan, S. A. Letzring, D. J. Lonobile, S. J. Loucks, L. D. Lund, F. J. Marshall, P. W. McKenty, D. D. Meyerhofer, S. F. B. Morse, A. Okishev, S. Papernov, G. Pien, W. Seka, R. Short, M. J. Shoup, M. Skeldon, S. Skupsky, A. W. Schmid, D. J. Smith, S. Swales, M. Wittman, and B. Yaakobi. Direct-drive laser-fusion experiments with the omega, 60-beam, ¿40 kj, ultraviolet laser system. *Physics of Plasmas*, 3(5):2108–2112, 1996. doi:10.1063/1.871662.

[7] D. Ryutov, R. P. Drake, J. Kane, E. Liang, B. A. Remington, and W. M. Wood-Vasey. Similarity criteria for the laboratory simulation of supernova hydrodynamics. *The Astrophysical Journal*, 518(2):821–832, jun 1999. doi:10.1086/307293.

[8] D. D. Ryutov, R. P. Drake, and B. A. Remington. Criteria for scaled laboratory simulations of astrophysical MHD phenomena. *The Astrophysical Journal Supplement Series*, 127(2):465–468, apr 2000. doi:10.1086/313320.

[9] D. D. Ryutov, B. A. Remington, H. F. Robey, and R. P. Drake. Magnetohydrodynamic scaling: From astrophysics to the laboratory. *Physics of Plasmas*, 8(5):1804–1816, 2001. doi:10.1063/1.1344562.

[10] D. D. Ryutov and B. A. Remington. Scaling astrophysical phenomena to high-energy-density laboratory experiments. *Plasma Physics and Controlled Fusion*, 44(12B):B407–B423, nov 2002. doi:10.1088/0741-3335/44/12b/328.

[11] R. P. Drake. Laboratory experiments to simulate the hydrodynamics of supernova remnants and supernovae. *J. Geophys. Res.*, 104(A7):14505–14516, July 1999. doi:10.1029/98JA02829.

[12] B. A. Remington, D. Arnett, R. Paul Drake, and H. Takabe. Modeling Astrophysical Phenomena in the Laboratory with Intense Lasers. *Science*, 284:1488, May 1999. doi:10.1126/science.284.5419.1488.

[13] Bruce A. Remington, R. Paul Drake, Hideaki Takabe, and David Arnett. A review of astrophysics experiments on intense lasers. *Physics of Plasmas*, 7(5):1641–1652, May 2000. doi:10.1063/1.874046.

[14] Bruce A. Remington, R. Paul Drake, and Dmitri D. Ryutov. Experimental astrophysics with high power lasers and Z pinches. *Reviews of Modern Physics*, 78(3):755–807, July 2006. doi:10.1103/RevModPhys.78.755.

[15] O. V. Gotchev, J. P. Knauer, P. Y. Chang, N. W. Jang, M. J. Shoup, D. D. Meyerhofer, and R. Betti. Seeding magnetic fields for laser-driven flux compression in high-energy-density plasmas. *Review of Scientific Instruments*, 80(4):043504, 2009. doi:10.1063/1.3115983.

[16] G. Fiksel, A. Agliata, D. Barnak, G. Brent, P. Y. Chang, L. Folnsbee, G. Gates, D. Hasset, D. Lonobile, J. Magoon, D. Mastrosimone, M. J. Shoup, and R. Betti. Note: Experimental platform for magnetized high-energy-density plasma studies at the omega laser facility. *Review of Scientific Instruments*, 86(1):016105, 2018/03/15 2015. doi:10.1063/1.4905625.

[17] R. P. Drake and G. Gregori. Design considerations for unmagnetized collisionless-shock measurements in homologous flows. *The Astrophysical Journal*, 749(2):171, 2012. doi:10.1088/0004-637X/749/2/171.

[18] W. Fox, G. Fiksel, A. Bhattacharjee, P.-Y. Chang, K. Germaschewski, S. X. Hu, and P. M. Nilson. Filamentation instability of counterstreaming laser-driven plasmas. *Phys. Rev. Lett.*, 111:225002, Nov 2013. doi:10.1103/PhysRevLett.111.225002.

[19] G. Gregori, A. Ravasio, C. D. Murphy, K. Schaar, A. Baird, A. R. Bell, A. Benuzzi-Mounaix, R. Bingham, C. Constantin, R. P. Drake, M. Edwards, E. T. Everson, C. D. Gregory, Y. Kuramitsu, W. Lau, J. Mithen, C. Niemann, H. S. Park, B. A. Remington, B. Reville, A. P. L. Robinson, D. D. Ryutov, Y. Sakawa, S. Yang, N. C. Woolsey, M. Koenig, and F. Miniati. Generation of scaled protogalactic seed magnetic fields in laser-produced shock waves. *Nature*, 481:480 EP –, 01 2012.

[20] C. M. Huntington, F. Fiuza, J. S. Ross, A. B. Zylstra, R. P. Drake, D. H. Froula, G. Gregori, N. L. Kugland, C. C. Kuranz, M. C. Levy, C. K. Li, J. Meinecke, T. Morita, R. Petrasso, C. Plechaty, B. A. Remington, D. D. Ryutov, Y. Sakawa, A. Spitkovsky, H. Takabe, and H. S. Park. Observation of magnetic field generation via the weibel instability in interpenetrating plasma flows. *Nature Physics*, 11:173 – 176, 01 2015.

[21] C. M. Huntington, M. J.-E. Manuel, J. S. Ross, S. C. Wilks, F. Fiuza, H. G. Rinderknecht, H.-S. Park, G. Gregori, D. P. Higginson, J. Park, B. B. Pollock, B. A. Remington, D. D. Ryutov, C. Ruyer, Y. Sakawa, H. Sio, A. Spitkovsky, G. F. Swadling, H. Takabe, and A. B. Zylstra. Magnetic field production via the weibel instability in interpenetrating plasma flows. *Physics of Plasmas*, 24(4):041410, 2017. doi:10.1063/1.4982044.

[22] N. L. Kugland, D. D. Ryutov, P-Y. Chang, R. P. Drake, G. Fiksel, D. H. Froula, S. H. Glenzer, G. Gregori, M. Grosskopf, M. Koenig, Y. Kuramitsu, C. Kuranz, M. C. Levy, E. Liang, J. Meinecke, F. Miniati, T. Morita, A. Pelka, C. Plechaty, R. Presura, A. Ravasio, B. A. Remington, B. Reville, J. S. Ross, Y. Sakawa, A. Spitkovsky, H. Takabe, and H-S. Park. Self-organized electromagnetic field structures in laser-produced counter-streaming plasmas. *Nature Physics*, 8:809 EP –, 09 2012.

[23] S S Moiseev and R Z Sagdeev. Collisionless shock waves in a plasma in a weak magnetic field. *Journal of Nuclear Energy. Part C, Plasma Physics, Accelerators, Thermonuclear Research*, 5(1):43, 1963.

[24] Hye-Sook Park, D. D. Ryutov, J. S. Ross, N. L. Kugland, S. H. Glenzer, C. Plechaty, S. M. Pollaine, B. A. Remington, A. Spitkovsky, L. Gargate, G. Gregori, A. Bell, C. Murphy, Y. Sakawa, Y. Kuramitsu, T. Morita, H. Takabe, D. H. Froula, G. Fiksel, F. Miniati, M. Koenig, A. Ravasio, A. Pelka, E. Liang, N. Woolsey, C. C. Kuranz, R. P. Drake, and M. J. Grosskopf. Studying astrophysical collisionless shocks with counterstreaming plasmas from high power lasers. *High Energy Density Physics*, 8(1):38–45, 2012. doi:https://doi.org/10.1016/j.hedp.2011.11.001.

[25] H.-S. Park, C. M. Huntington, F. Fiuza, R. P. Drake, D. H. Froula, G. Gregori, M. Koenig, N. L. Kugland, C. C. Kuranz, D. Q. Lamb, M. C. Levy, C. K. Li, J. Meinecke, T. Morita, R. D. Petrasso, B. B. Pollock, B. A. Remington, H. G. Rinderknecht, M. Rosenberg, J. S. Ross, D. D. Ryutov, Y. Sakawa, A. Spitkovsky, H. Takabe, D. P.

Turnbull, P. Tzeferacos, S. V. Weber, and A. B. Zylstra. Collisionless shock experiments with lasers and observation of weibel instabilities. *Physics of Plasmas*, 22(5):056311, 2015. doi:10.1063/1.4920959.

[26] J. S. Ross, J. D. Moody, F. Fiuza, D. Ryutov, L. Divol, C. M. Huntington, and H. S. Park. Thomson scattering measurements from asymmetric interpenetrating plasma flows. *Review of Scientific Instruments*, 85(11):11E613, 2018/03/16 2014. doi:10.1063/1.4891974.

[27] D D Ryutov, N L Kugland, H S Park, C Plechaty, B A Remington, and J S Ross. Basic scalings for collisionless-shock experiments in a plasma without pre-imposed magnetic field. *Plasma Physics and Controlled Fusion*, 54(10):105021, 2012.

[28] D. B. Schaeffer, W. Fox, D. Haberberger, G. Fiksel, A. Bhattacharjee, D. H. Barnak, S. X. Hu, K. Germaschewski, and R. K. Follett. High-mach number, laser-driven magnetized collisionless shocks. *Physics of Plasmas*, 24(12):122702, 2017. doi:10.1063/1.4989562.

[29] D. B. Schaeffer, W. Fox, R. K. Follett, G. Fiksel, C. K. Li, J. Matteucci, A. Bhattacharjee, and K. Germaschewski. Direct observations of particle dynamics in magnetized collisionless shock precursors in laser-produced plasmas. *Phys. Rev. Lett.*, 122:245001, Jun 2019. doi:10.1103/PhysRevLett.122.245001.

[30] A. Stockem, F. Fiuza, A. Bret, R. A. Fonseca, and L. O. Silva. Exploring the nature of collisionless shocks under laboratory conditions. *Scientific Reports*, 4:3934 EP –, 02 2014.

[31] Anatoly Spitkovsky. On the structure of relativistic collisionless shocks in electron-ion plasmas. *The Astrophysical Journal Letters*, 673(1):L39, 2008.

[32] L. Willingale, P. M. Nilson, M. C. Kaluza, A. E. Dangor, R. G. Evans, P. Fernandes, M. G. Haines, C. Kamperidis, R. J. Kingham, C. P. Ridgers, M. Sherlock, A. G. R. Thomas, M. S. Wei, Z. Najmudin, K. Krushelnick, S. Band yopadhyay, M. Notley, S. Minardi, M. Tatarakis, and W. Rozmus. Proton deflectometry of a magnetic reconnection geometry. *Physics of Plasmas*, 17(4):043104, April 2010. doi:10.1063/1.3377787.

[33] M. J. Rosenberg, C. K. Li, W. Fox, I. Igumenshchev, F. H. Séguin, R. P. J. Town, J. A. Frenje, C. Stoeckl, V. Glebov, and R. D. Petrasso. A laboratory study of asymmetric magnetic reconnection in strongly driven plasmas. *Nature Communications*, 6:6190, February 2015. doi:10.1038/ncomms7190.

[34] P. Tzeferacos, A. Rigby, A. F. A. Bott, A. R. Bell, R. Bingham, A. Casner, F. Cattaneo, E. M. Churazov, J. Emig, F. Fiuza, C. B. Forest, J. Foster, C. Graziani, J. Katz, M. Koenig, C. K. Li, J. Meinecke, R. Petrasso, H. S. Park, B. A. Remington, J. S. Ross, D. Ryu, D. Ryutov, T. G. White, B. Reville, F. Miniati, A. A. Schekochihin, D. Q. Lamb, D. H. Froula, and G. Gregori. Laboratory evidence of dynamo amplification of magnetic fields in a turbulent plasma. *Nature Communications*, 9(1):591, 2018. doi:10.1038/s41467-018-02953-2.

[35] Andy Sha Liao, Shengtai Li, Hui Li, Kirk Flippo, Daniel Barnak, Kwyntero Van Kelso, Codie Fiedler Kawaguchi, Alexander Rasmus, Sallee Klein, Joseph Levesque, Carolyn Kuranz, and Chikang Li. Design of a new turbulent dynamo experiment on the OMEGA-EP. *Physics of Plasmas*, 26(3):032306, March 2019. doi:10.1063/1.5081062.

[36] G. C. Burdiak, S. V. Lebedev, S. N. Bland, T. Clayson, J. Hare, L. Suttle, F. Suzuki-Vidal, D. C. Garcia, J. P. Chittenden, S. Bott-Suzuki, A. Ciardi, A. Frank, and T. S. Lane. The structure of bow shocks formed by the interaction of pulsed-power driven magnetised plasma flows with conducting obstacles. *Physics of Plasmas*, 24(7):072713, 2017. doi:10.1063/1.4993187.

[37] L. G. Suttle, G. C. Burdiak, C. L. Cheung, T. Clayson, J. W. D. Halliday, J. D. Hare, S. Rusli, D. R. Russell, E. R. Tubman, A. Ciardi, N. F. Loureiro, J. Li, A. Frank, and S. V. Lebedev. Interactions of magnetized plasma flows in pulsed-power driven experiments. *Plasma Physics and Controlled Fusion*, 62(1):014020, Jan 2020. doi:10.1088/1361-6587/ab5296.

[38] Russell M. Kulsrud. *Plasma Physics for Astrophysics*. Princeton University Press, 2005.

[39] Paul M. Bellan. *Fundamentals of Plasma Physics*. Cambridge University Press, 2006.

[40] Francis F. Chen. *Introduction to Plasma Physics and Controlled Fusion*, volume 1. Plenum Press, 2 edition, 1983.

[41] Margaret G. Kivelson and Christopher T. Russell, editors. *Introduction to Space Physics*. Cambridge University Press, 1995.

[42] A. Kantrowitz and H. E. Petshek. Mhd characteristics and shock waves. In Wulf B. Kunkel, editor, *Plasma Physics in Theory and Application*, chapter 6, pages 147–206. McGraw-Hill, 1966.

[43] Bruce T. Draine and Christopher F. McKee. Theory of interstellar shocks. *Annual Review of Astronomy and Astrophysics*, 31(1):373–432, 1993. doi:10.1146/annurev.aa.31.090193.002105.

[44] Patrick Hartigan. Shock waves in outflows from young stars. *Astrophysics and Space Science*, 287(1):111–122, 2003. doi:10.1023/B:ASTR.0000006209.56314.c8.

[45] R. P. Drake. The design of laboratory experiments to produce collisionless shocks of cosmic relevance. *Physics of Plasmas*, 7(11):4690–4698, 2000. doi:10.1063/1.1314625.

[46] F. Fiuza, R. A. Fonseca, J. Tonge, W. B. Mori, and L. O. Silva. Weibel-instability-mediated collisionless shocks in the laboratory with ultraintense lasers. *Phys. Rev. Lett.*, 108:235004, Jun 2012. doi:10.1103/PhysRevLett.108.235004.

[47] Erich S. Weibel. Spontaneously growing transverse waves in a plasma due to an anisotropic velocity distribution. *Phys. Rev. Lett.*, 2:83–84, 02 1959. doi:10.1103/PhysRevLett.2.83.

[48] R. Schlickeiser and P. K. Shukla. Cosmological magnetic field generation by the weibel instability. *The Astrophysical Journal*, 599(2):L57–L60, dec 2003. doi:10.1086/381246.

[49] Donald H. Fairfield. Average and unusual locations of the earth's magnetopause and bow shock. *Journal of Geophysical Research (1896-1977)*, 76(28):6700–6716, 1971. doi:10.1029/JA076i028p06700.

[50] T. W. Moore, K. Nykyri, and A. P. Dimmock. Cross-scale energy transport in space plasmas. *Nat Phys*, 12(12):1164–1169, 12 2016. doi:10.1038/nphys3869.

[51] A. J. Hundhausen. The solar wind. In M. G. Kivelson and C. T. Russell, editor, *Introduction to Space Physics*, chapter 4, pages 91–128. Cambridge University Press, 1995.

[52] E.W. Cliver. The 1859 space weather event: Then and now. *Advances in Space Research*, 38(2):119 – 129, 2006. doi:https://doi.org/10.1016/j.asr.2005.07.077.

[53] James L. Green, Scott Boardsen, Sten Odenwald, John Humble, and Katherine A. Pazamickas. Eyewitness reports of the great auroral storm of 1859. *Advances in Space Research*, 38(2):145 – 154, 2006. doi:https://doi.org/10.1016/j.asr.2005.12.021.

[54] N. L. Kugland, D. D. Ryutov, C. Plechaty, J. S. Ross, and H.-S. Park. Invited article: Relation between electric and magnetic field structures and their proton-beam images. *Review of Scientific Instruments*, 83(10), 2012. doi:10.1063/1.4750234.

[55] Dustin H. Froula, Siegfried H. Glenzer, Neville C. Luhmann, and John Sheffield, editors. *Plasma Scattering of Electromagnetic Radiation*. Academic Press, Boston, second edition edition, 2011.

[56] D. H. Froula, J. S. Ross, L. Divol, and S. H. Glenzer. Thomson-scattering techniques to diagnose local electron and ion temperatures, density, and plasma wave amplitudes in laser produced plasmas (invited). *Review of Scientific Instruments*, 77(10):10E522, 2006. doi:10.1063/1.2336451.

[57] J. S. Ross, S. H. Glenzer, J. P. Palastro, B. B. Pollock, D. Price, G. R. Tynan, and D. H. Froula. Thomson-scattering measurements in the collective and noncollective regimes in laser produced plasmas (invited). *Review of Scientific Instruments*, 81(10):10D523, 2010. doi:10.1063/1.3478975.

[58] R. K. Follett, J. A. Delettrez, D. H. Edgell, R. J. Henchen, J. Katz, J. F. Myatt, and D. H. Froula. Plasma characterization using ultraviolet thomson scattering from ion-acoustic and electron plasma waves (invited). *Review of Scientific Instruments*, 87(11): 11E401, 2018/03/15 2016. doi:10.1063/1.4959160.

[59] J. S. Ross, D. H. Froula, A. J. Mackinnon, C. Sorce, N. Meezan, S. H. Glenzer, W. Armstrong, R. Bahr, R. Huff, and K. Thorp. Implementation of imaging thomson scattering on the omega laser. *Review of Scientific Instruments*, 77(10):10E520, 2018/04/18 2006. doi:10.1063/1.2220077.

[60] J. Katz, J. S. Ross, C. Sorce, and D. H. Froula. A reflective image-rotating periscope for spatially resolved thomson-scattering experiments on omega. *Journal of Instrumentation*, 8(12):C12009, 2013. doi:10.1088/1748-0221/8/12/C12009.

[61] Joseph Levesque, Carolyn Kuranz, Timothy Handy, Mario Manuel, and Frederico Fiuza. Characterizing filamentary magnetic structures in counter-streaming plasmas by fourier analysis of proton images. *Physics of Plasmas*, 26(10):102303, 2019. doi:10.1063/1.5100728.

[62] G. F. Swadling, S. V. Lebedev, G. N. Hall, S. Patankar, N. H. Stewart, R. A. Smith, A. J. Harvey-Thompson, G. C. Burdiak, P. de Grouchy, J. Skidmore, L. Suttle, F. Suzuki-Vidal, S. N. Bland, K. H. Kwek, L. Pickworth, M. Bennett, J. D. Hare, W. Rozmus, and J. Yuan. Diagnosing collisions of magnetized, high energy density plasma flows using a combination of collective thomson scattering, faraday rotation, and interferometry (invited). *Review of Scientific Instruments*, 85(11):11E502, 2018/03/16 2014. doi:10.1063/1.4890564.

[63] R. A. Snavely, M. H. Key, S. P. Hatchett, T. E. Cowan, M. Roth, T. W. Phillips, M. A. Stoyer, E. A. Henry, T. C. Sangster, M. S. Singh, S. C. Wilks, A. MacKinnon, A. Offenberger, D. M. Pennington, K. Yasuike, A. B. Langdon, B. F. Lasinski, J. Johnson, M. D. Perry, and E. M. Campbell. Intense high-energy proton beams from petawatt-laser irradiation of solids. *Phys. Rev. Lett.*, 85:2945–2948, Oct 2000. doi:10.1103/PhysRevLett.85.2945.

[64] Stephen P. Hatchett, Curtis G. Brown, Thomas E. Cowan, Eugene A. Henry, Joy S. Johnson, Michael H. Key, Jeffrey A. Koch, A. Bruce Langdon, Barbara F. Lasinski, Richard W. Lee, Andrew J. Mackinnon, Deanna M. Pennington, Michael D. Perry, Thomas W. Phillips, Markus Roth, T. Craig Sangster, Mike S. Singh, Richard A. Snavely, Mark A. Stoyer, Scott C. Wilks, and Kazuhito Yasuike. Electron, photon, and ion beams from the relativistic interaction of petawatt laser pulses with solid targets. *Physics of Plasmas*, 7(5):2076–2082, 2000. doi:10.1063/1.874030.

[65] C. K. Li, F. H. Séguin, J. A. Frenje, J. R. Rygg, R. D. Petrasso, R. P. J. Town, P. A. Amendt, S. P. Hatchett, O. L. Landen, A. J. Mackinnon, P. K. Patel, V. A. Smalyuk, J. P. Knauer, T. C. Sangster, and C. Stoeckl. Monoenergetic proton backlighter for measuring e and b fields and for radiographing implosions and high-energy density plasmas (invited). *Review of Scientific Instruments*, 77(10):10E725, 2006. doi:10.1063/1.2228252.

[66] A. J. Mackinnon, P. K. Patel, R. P. Town, M. J. Edwards, T. Phillips, S. C. Lerner, D. W. Price, D. Hicks, M. H. Key, S. Hatchett, S. C. Wilks, M. Borghesi, L. Romagnani, S. Kar, T. Toncian, G. Pretzler, O. Willi, M. Koenig, E. Martinolli, S. Lepape, A. Benuzzi-Mounaix, P. Audebert, J. C. Gauthier, J. King, R. Snavely, R. R. Freeman, and T. Boehlly. Proton radiography as an electromagnetic field and density perturbation diagnostic (invited). *Review of Scientific Instruments*, 75(10):3531–3536, 2004. doi:10.1063/1.1788893.

[67] J. F. Nye. *Natural focusing and fine structure of light : caustics and wave dislocations*. Institute of Physics Pub., Bristol ; Philadelphia :, 2020-05-13 1999.

[68] M. C. Levy, D. D. Ryutov, S. C. Wilks, J. S. Ross, C. M. Huntington, F. Fiuza, D. A. Martinez, N. L. Kugland, M. G. Baring, and H.-S. Park. Development of an interpretive simulation tool for the proton radiography technique. *Review of Scientific Instruments*, 86(3):033302, 2015. doi:10.1063/1.4909536.

[69] Carlo Graziani, Petros Tzeferacos, Donald Q. Lamb, and Chikang Li. Inferring morphology and strength of magnetic fields from proton radiographs. *Review of Scientific Instruments*, 88(12):123507, 2017. doi:10.1063/1.5013029.

[70] A. F. A. Bott, C. Graziani, P. Tzeferacos, T. G. White, D. Q. Lamb, G. Gregori, and A. A. Schekochihin. Proton imaging of stochastic magnetic fields. *Journal of Plasma Physics*, 83(6):905830614, 2017. doi:10.1017/S0022377817000939.

[71] M. Borghesi, D. H. Campbell, A. Schiavi, M. G. Haines, O. Willi, A. J. MacKinnon, P. Patel, L. A. Gizzi, M. Galimberti, R. J. Clarke, F. Pegoraro, H. Ruhl, and S. Bulanov. Electric field detection in laser-plasma interaction experiments via the proton imaging technique. *Physics of Plasmas*, 9(5):2214–2220, 2002. doi:10.1063/1.1459457.

[72] C. K. Li, F. H. Séguin, J. A. Frenje, M. Manuel, D. Casey, N. Sinenian, R. D. Petrasso, P. A. Amendt, O. L. Landen, J. R. Rygg, R. P. J. Town, R. Betti, J. Delettrez, J. P. Knauer, F. Marshall, D. D. Meyerhofer, T. C. Sangster, D. Shvarts, V. A. Smalyuk, J. M. Soures, C. A. Back, J. D. Kilkenny, and A. Nikroo. Proton radiography of dynamic electric and magnetic fields in laser-produced high-energy-density plasmas. *Physics of Plasmas*, 16(5):056304, 2009. doi:10.1063/1.3096781.

[73] J. S. Ross, S. H. Glenzer, P. Amendt, R. Berger, L. Divol, N. L. Kugland, O. L. Landen, C. Plechaty, B. Remington, D. Ryutov, W. Rozmus, D. H. Froula, G. Fiksel, C. Sorce, Y. Kuramitsu, T. Morita, Y. Sakawa, H. Takabe, R. P. Drake, M. Grosskopf, C. Kuranz, G. Gregori, J. Meinecke, C. D. Murphy, M. Koenig, A. Pelka, A. Ravasio, T. Vinci, E. Liang, R. Presura, A. Spitkovsky, F. Miniati, and H.-S. Park. Characterizing counter-streaming interpenetrating plasmas relevant to astrophysical collisionless shocks. *Physics of Plasmas*, 19(5):056501, 2012. doi:10.1063/1.3694124.

[74] N. L. Kugland, J. S. Ross, P.-Y. Chang, R. P. Drake, G. Fiksel, D. H. Froula, S. H. Glenzer, G. Gregori, M. Grosskopf, C. Huntington, M. Koenig, Y. Kuramitsu, C. Kuranz, M. C. Levy, E. Liang, D. Martinez, J. Meinecke, F. Miniati, T. Morita, A. Pelka, C. Plechaty, R. Presura, A. Ravasio, B. A. Remington, B. Reville, D. D. Ryutov, Y. Sakawa, A. Spitkovsky, H. Takabe, and H.-S. Park. Visualizing electromagnetic fields in laser-produced counter-streaming plasma experiments for collisionless shock laboratory astrophysics. *Physics of Plasmas*, 20(5):056313, 2013. doi:10.1063/1.4804548.

[75] J. S. Ross, D. P. Higginson, D. Ryutov, F. Fiuza, R. Hatarik, C. M. Huntington, D. H. Kalantar, A. Link, B. B. Pollock, B. A. Remington, H. G. Rinderknecht, G. F. Swadling, D. P. Turnbull, S. Weber, S. Wilks, D. H. Froula, M. J. Rosenberg, T. Morita, Y. Sakawa, H. Takabe, R. P. Drake, C. Kuranz, G. Gregori, J. Meinecke, M. C. Levy, M. Koenig, A. Spitkovsky, R. D. Petrasso, C. K. Li, H. Sio, B. Lahmann, A. B. Zylstra, and H. S. Park. Transition from Collisional to Collisionless Regimes in Interpenetrating Plasma

Flows on the National Ignition Facility. *Physical Review Letters*, 118:185003, May 2017. doi:10.1103/PhysRevLett.118.185003.

[76] Burton D. Fried. Mechanism for instability of transverse plasma waves. *The Physics of Fluids*, 2(3):337–337, 1959. doi:10.1063/1.1705933.

[77] Mikhail V. Medvedev and Abraham Loeb. Generation of magnetic fields in the relativistic shock of gamma-ray burst sources. *The Astrophysical Journal*, 526(2):697, 1999.

[78] Mikhail V. Medvedev, Luis O. Silva, and Marc Kamionkowski. Cluster magnetic fields from large-scale structure and galaxy cluster shocks. *The Astrophysical Journal*, 642 (1):L1–L4, apr 2006. doi:10.1086/504470.

[79] C. Ruyer and F. Fiuza. Disruption of current filaments and isotropization of the magnetic field in counterstreaming plasmas. *Phys. Rev. Lett.*, 120:245002, Jun 2018. doi:10.1103/PhysRevLett.120.245002.

[80] D. P. Kroese and Z. I. Botev. Spatial process simulation. In Schmidt V., editor, *Stochastic Geometry, Spatial Statistics and Random Fields*, volume 2120. Springer, Cham, 2015.

[81] CR Dietrich and GN Newsam. Fast and exact simulation of stationary gaussian processes through circulant embedding of the covariance matrix. *SIAM Journal on Scientific Computing*, 18(4):1088–1107, JUL 1997. doi:10.1137/S1064827592240555.

[82] John R. Spreiter, Audrey L. Summers, and Alberta Y. Alksne. Hydromagnetic flow around the magnetosphere. *Planetary and Space Science*, 14(3):223 – 253, 1966. doi:10.1016/0032-0633(66)90124-3.

[83] H. C. Zhuang and C. T. Russell. An analytic treatment of the structure of the bow shock and magnetosheath. *Journal of Geophysical Research: Space Physics*, 86(A4): 2191–2205, 1981. doi:10.1029/JA086iA04p02191.

[84] Iver H. Cairns and Crockett L. Grabbe. Towards an mhd theory for the standoff distance of earth's bow shock. *Geophysical Research Letters*, 21(25):2781–2784, 1994. doi:10.1029/94GL02551.

[85] J. G. Luhmann. Plasma interactions with unmagnetized bodies. In M. G. Kivelson and C. T. Russell, editor, *Introduction to Space Physics*, chapter 8, pages 203–226. Cambridge University Press, 1995.

[86] Maxim L. Khodachenko, Ignasi Ribas, Helmut Lammer, Jean-Mathias Grießmeier, Martin Leitner, Franck Selsis, Carlos Eiroa, Arnold Hanslmeier, Helfried K. Biernat, Charles J. Farrugia, and Helmut O. Rucker. Coronal mass ejection (cme) activity of low mass m stars as an important factor for the habitability of terrestrial exoplanets. i. cme impact on expected magnetospheres of earth-like exoplanets in close-in habitable zones. *Astrobiology*, 7(1):167–184, 2007. doi:10.1089/ast.2006.0127.

[87] A. A. Vidotto, R. Fares, M. Jardine, C. Moutou, and J. F. Donati. On the environment surrounding close-in exoplanets. *MNRAS*, 449(4):4117–4130, June 2015. doi:10.1093/mnras/stv618.

[88] Gábor Tóth, Igor V. Sokolov, Tamas I. Gombosi, David R. Chesney, C. Robert Clauer, Darren L. De Zeeuw, Kenneth C. Hansen, Kevin J. Kane, Ward B. Manchester, Robert C. Oehmke, Kenneth G. Powell, Aaron J. Ridley, Ilia I. Roussev, Quentin F. Stout, Ovsei Volberg, Richard A. Wolf, Stanislav Sazykin, Anthony Chan, Bin Yu, and József Kóta. Space weather modeling framework: A new tool for the space science community. *Journal of Geophysical Research: Space Physics*, 110(A12), 2005. doi:10.1029/2005JA011126.

[89] B. Lavraud and J. E. Borovsky. Altered solar wind-magnetosphere interaction at low mach numbers: Coronal mass ejections. *Journal of Geophysical Research: Space Physics*, 113(A9):n/a–n/a, 2008. doi:10.1029/2008JA013192.

[90] Andy Sha Liao, Shule Li, Patrick Hartigan, Peter Graham, Gennady Fiksel, Adam Frank, John Foster, and Carolyn Kuranz. Numerical simulation of an experimental analogue of a planetary magnetosphere. *High Energy Density Physics*, 17, Part A:38 – 41, 2015. doi:10.1016/j.hedp.2014.09.005.

[91] Dongwook Lee and Anil E. Deane. An unsplit staggered mesh scheme for multidimensional magnetohydrodynamics. *Journal of Computational Physics*, 228(4):952 – 975, 2009. doi:https://doi.org/10.1016/j.jcp.2008.08.026.

[92] P. Tzeferacos, M. Fatenejad, N. Flocke, G. Gregori, D.Q. Lamb, D. Lee, J. Meinecke, A. Scopatz, and K. Weide. Flash magnetohydrodynamic simulations of shock-generated magnetic field experiments. *High Energy Density Physics*, 8(4):322 – 328, 2012. doi:https://doi.org/10.1016/j.hedp.2012.08.001.

[93] D. J. Mullan and C. W. Smith. Solar wind statistics at 1 au: Alfven speed and plasma beta. *Solar Physics*, 234(2):325–338, 2006. doi:10.1007/s11207-006-2077-y.

[94] *PrismSPECT version 6.5.0*. Prism Computational Sciences, Inc., www.prism-cs.com, .

[95] Eric R. Priest. *Solar Magnetohydrodynamics*. Springer, Dordrecht, 1982.

[96] Mohamed M. Sulman, J.F. Williams, and Robert D. Russell. An efficient approach for the numerical solution of the monge–ampère equation. *Applied Numerical Mathematics*, 61(3):298 – 307, 2011. doi:https://doi.org/10.1016/j.apnum.2010.10.006.

[97] *PROPACEOS software*. Prism Computational Sciences, Inc., www.prism-cs.com, .

[98] J. P. Eastwood, H. Hietala, G. Toth, T. D. Phan, and M. Fujimoto. What controls the structure and dynamics of earth's magnetosphere? *Space Science Reviews*, 188(1): 251–286, 2015. doi:10.1007/s11214-014-0050-x.